

AD-A149 333

ANALYSIS OF SHOCK TO DETONATION TRANSITION (SDT) OF
POROUS HIGH ENERGY PR. (U) ILLINOIS UNIV AT URBANA DEPT
OF MECHANICAL AND INDUSTRIAL ENG. H KRIER ET AL

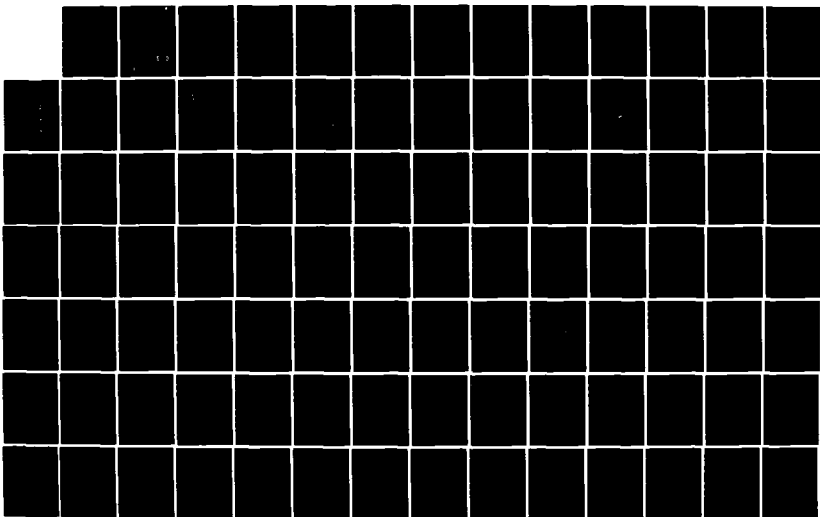
1/2

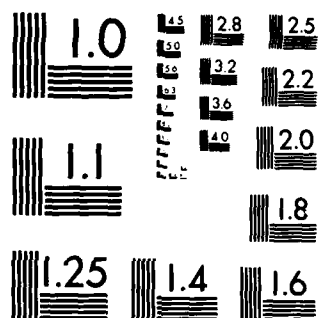
UNCLASSIFIED

SEP 84 UIIU-ENG-84-4007 AFOSR-TR-84-1105

F/G 21/9.2

NL



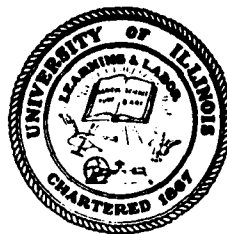


MICROCOPY RESOLUTION TEST CHART
NATIONAL BUREAU OF STANDARDS-1963-A

AFOSR-TR. 84-1105

50

DEPARTMENT OF MECHANICAL
AND INDUSTRIAL ENGINEERING
UNIVERSITY OF ILLINOIS AT URBANA-CHAMPAIGN
URBANA, IL 61801



Technical Report UILU ENG-84-4007

ANALYSIS OF SHOCK TO DETONATION TRANSITION (SDT)
OF POROUS HIGH ENERGY PROPELLANT FROM
RAMP-WAVE COMPRESSION LOADING

Annual Technical Report

AFOSR Grant No. 81-0145

September 15, 1984

DTIC
ELECTE
DEC 28 1984
S D E

release
distribution unlimited.

84 12 17 093

AD-A149 333

016 full copy

ANNUAL TECHNICAL REPORT

No. UILU-ENG-84-4007

For Research Supported by

AFOSR Grant No. 81-0145

-entitled-

ANALYSIS OF SHOCK TO DETONATION TRANSITION (SDT)
OF POROUS HIGH ENERGY PROPELLANT FROM
RAMP-WAVE COMPRESSION LOADING

prepared by

Herman Krier⁽¹⁾ and Christopher A. Cudak⁽²⁾

Department of Mechanical and Industrial Engineering
University of Illinois at Urbana-Champaign
144 MEB, 1206 W. Green St., Urbana, IL 61801

work supported by

Air Force Office of Scientific Research

(1) Principal Investigator; Professor of Mechanical Engineering

(2) Research Assistant

AIR FORCE OFFICE OF SCIENTIFIC RESEARCH
NOTICE OF RESEARCH RESULTS
This report is the property of the Air Force Office of Scientific Research and is loaned to you for your information. It is not to be distributed outside your organization without the written permission of the Air Force Office of Scientific Research.
MATTHEW J. [illegible]
Chief, Technical Information Division

UNCLASSIFIED

i

SECURITY CLASSIFICATION OF THIS PAGE

REPORT DOCUMENTATION PAGE

1a. REPORT SECURITY CLASSIFICATION UNCLASSIFIED		1b. RESTRICTIVE MARKINGS None													
2a. SECURITY CLASSIFICATION AUTHORITY		3. DISTRIBUTION/AVAILABILITY OF REPORT Approved for Public Release; Distribution Unlimited													
2b. DECLASSIFICATION/DOWNGRADING SCHEDULE															
4. PERFORMING ORGANIZATION REPORT NUMBER(S) UILU-ENG-84-4007		5. MONITORING ORGANIZATION REPORT NUMBER(S) AFOSR-TR- 84 - 1105													
6a. NAME OF PERFORMING ORGANIZATION University of Illinois	6b. OFFICE SYMBOL (If applicable) UIUC	7a. NAME OF MONITORING ORGANIZATION Air Force Office of Scientific Research													
6c. ADDRESS (City, State and ZIP Code) Dept. of Mechanical and Industrial Engr. 144 MEB; University of Illinois Urbana, IL 61801		7b. ADDRESS (City, State and ZIP Code) ATTN: Dr. R. J. Barker/NP Bolling AFB, DC 20332													
8a. NAME OF FUNDING/SPONSORING ORGANIZATION Air Force Office of Scientific Research	8b. OFFICE SYMBOL (If applicable) AFOSR	9. PROCUREMENT INSTRUMENT IDENTIFICATION NUMBER Grant No. AFOSR-81-0145													
8c. ADDRESS (City, State and ZIP Code) AFOSR/NP Dr. Robert J. Barker Bolling AFB, DC 20332		10. SOURCE OF FUNDING NOS. <table border="1"><tr><td>PROGRAM ELEMENT NO.</td><td>PROJECT NO.</td><td>TASK NO.</td><td>WORK UNIT NO.</td></tr><tr><td>61102F</td><td>2301</td><td>AG</td><td></td></tr></table>		PROGRAM ELEMENT NO.	PROJECT NO.	TASK NO.	WORK UNIT NO.	61102F	2301	AG					
PROGRAM ELEMENT NO.	PROJECT NO.	TASK NO.	WORK UNIT NO.												
61102F	2301	AG													
11. TITLE (Include Security Classification) <i>see front cover</i>															
12. PERSONAL AUTHOR(S) HERMAN KRIER and CHRISTOPHER A. CUDAK															
13a. TYPE OF REPORT INTERIM Rept.	13b. TIME COVERED FROM 1/10/83 TO 9/10/84	14. DATE OF REPORT (Yr., Mo., Day) September 1984	15. PAGE COUNT 112												
16. SUPPLEMENTARY NOTATION															
17. COSATI CODES <table border="1"><tr><th>FIELD</th><th>GROUP</th><th>SUB. GR.</th></tr><tr><td></td><td></td><td></td></tr><tr><td></td><td></td><td></td></tr><tr><td></td><td></td><td></td></tr></table>		FIELD	GROUP	SUB. GR.										18. SUBJECT TERMS (Continue on reverse if necessary and identify by block number) Shock initiation of explosives; Transition to detonation; Dynamic compression of porous solids	
FIELD	GROUP	SUB. GR.													
19. ABSTRACT (Continue on reverse if necessary and identify by block number) → Increasing the nitramine content of solid rocket propellants increases the overall performance of the system as well as the sensitivity to detonation by shock initiation. In some instances a confined zone of granulated propellant adjacent to a zone of cast propellant can provide a rapid enough pressure-rise rate to shock initiate the cast material. If the cast propellant is porous, the detonation will initiate at some location ahead of the granulated bed/cast material interface. The work presented here is an effort to numerically model this Deflagration to Shock to Detonation Transition (DSDT) event. Results are presented showing the detonation build up for propellants/explosives with various initial void content and ramp wave compression loads.															
20. DISTRIBUTION/AVAILABILITY OF ABSTRACT UNCLASSIFIED/UNLIMITED <input checked="" type="checkbox"/> SAME AS RPT. <input checked="" type="checkbox"/> DTIC USERS <input type="checkbox"/>		21. ABSTRACT SECURITY CLASSIFICATION UNCLASSIFIED													
22a. NAME OF RESPONSIBLE INDIVIDUAL Dr. Robert J. Barker	22b. TELEPHONE NUMBER (Include Area Code) 202-767-5011	22c. OFFICE SYMBOL AFOSR/NP													

DD FORM 1473, 83 APR

EDITION OF 1 JAN 73 IS OBSOLETE.

UNCLASSIFIED

SECURITY CLASSIFICATION OF THIS PAGE

TABLE OF CONTENTS

	Page
NOMENCLATURE	iv
CHAPTER 1 REVIEW AND OVERVIEW.....	1
1.1 <u>Related Published Works</u>	2
1.2 <u>Hot Spot Theory</u>	11
1.3 <u>Scope of Our Study</u>	12
CHAPTER 2 MATHEMATICAL AND NUMERICAL ANALYSIS.....	20
2.1 <u>Free Boundary</u>	20
2.2 <u>Governing Equations</u>	22
2.3 <u>Constitutive Relations</u>	24
2.4 <u>The Localized Hot Spot Temperature</u>	32
2.5 <u>The Combustion Model</u>	35
2.6 <u>Review of the Key Assumptions</u>	37
2.7 <u>Numerical Solution Technique</u>	41
CHAPTER 3 NUMERICAL RESULTS.....	48
3.1 <u>Shock Initiation of Detonation</u>	49
3.2 <u>Validation of the Model</u>	53
3.3 <u>Typical Cases</u>	56
3.4 <u>Numerical Accuracy Test</u>	72
3.5 <u>Comparison of the Combustion Models</u>	80
3.6 <u>Parametric Studies</u>	89

CHAPTER 4	CONCLUDING REMARKS.....	94
4.1	<u>Necessary Improvements</u>	94
4.2	<u>Importance of the Work</u>	96
APPENDIX A:	<u>HMX PROPERTIES</u>	98
APPENDIX B:	<u>RECIPROCITY RELATIONS</u>	100
REFERENCES	102

Accession For	
NTIS GRA&I	<input checked="" type="checkbox"/>
DTIC TAB	<input type="checkbox"/>
Unannounced	<input type="checkbox"/>
Justification	
By	
Distribution/	
Availability Codes	
Dist	Avail and/or Special
A-1	



NOMENCLATURE

Symbols	Definition	Units
c	sound speed	cm/s
C_v	specific heat at constant volume	erg/g/K
D	detonation velocity	mm/ μ sec
e	specific internal energy	erg/g
E	total internal energy	erg
E^*	activation energy	erg/mole
h	Lagrangian spatial coordinate	cm
H_{DET}	heat of detonation	erg/g
G	shear modulus	dynes/cm ²
M	mass	g
P	pressure	dynes/cm ²
P^*	maximum input pressure	dynes/cm ²
q	artificial viscosity	dynes/cm ²
Q	chemical energy release rate	erg/g/s
R	detonation velocity	mm/ μ sec
\bar{R}	universal gas constant	erg/mole/K
\hat{R}	product gas constant	erg/g/K
t	time	s
t^*	characteristic rise time	μ sec
T	temperature	K
T_H	hot spot temperature	K
T^*	characteristic burn temperature	K

\hat{T}	activation temperature	K
u	particle velocity	cm/s
v	specific volume	cm ³ /g
V	volume	cm ³
W	unreacted mass fraction	
W_B	$W_B = 1 - W_H$	
W_H	hot spot mass fraction	
x	Eulerian spatial coordinate	cm
Y	yield strength	dynes/cm ²
z	frequency factor	1/s
z	run-up distance to detonation	cm

Greek

α	$V_T/V_S = 1/(1 - \phi)$	
β	covolume correction term	cm ³ /g
ϕ	porosity, V_g/V_T	
Γ	Gruneisen coefficient	
κ_0	isothermal compressibility of the material at standard conditions	cm ² /dynes
κ_p	coefficient of thermal expansion	1/K
ρ	density	g/cm ³
τ	hot spot decomposition time	μ sec
ψ	Helmholtz free energy	erg/g

Subscripts

bc	boundary condition
CJ	Chapman-Jouguet state
g	gas
I	isentropes
o	initial state
s	solid
T	total or mechanical mixture

ABSTRACT

Increasing the nitramine content of solid rocket propellants increases the overall performance of the system as well as the sensitivity to detonation by shock initiation. In some instances a confined zone of granulated propellant adjacent to a zone of cast propellant can provide a rapid enough pressure-rise rate to shock initiate the cast material. If the cast propellant is porous, the detonation will initiate at some location ahead of the granulated bed/cast material interface. The work presented here is an effort to numerically model this Deflagration to Shock to Detonation Transition (DSDT) event. Results are presented showing the detonation build up for propellants/explosives with various initial void content and ramp wave compression loads.

CHAPTER 1

REVIEW AND OVERVIEW

Improving the specific impulse of a solid rocket motor continues to be an engineering endeavor. The specific impulse of a system is defined to be the ratio of thrust to fuel mass flow rate and is a technical description of the overall performance of a system. Recently, one of the most advantageous ways of increasing the specific impulse has been to use secondary high explosives as constituents in the propellant mixture. However, when high-energy nitramines such as HMX (octogen) are utilized in the propellant formulation the hazard of a Deflagration to Shock to Detonation (DSDT) becomes a relevant new concern.

A DSDT event is defined as a controlled subsonic deflagration wave making a transition to a high order steady detonation wave. Most researchers agree that in order for DSDT to occur the rocket motor grain must first be damaged. Granulation of the propellant bed can be a result of a handling accident or case and/or nozzle failure during operation. Moreover, once a region of granulated material has been ignited in a confined configuration the high surface to volume ratio particles provide an increased gas generation and a rapid pressurization rate which can shock initiate the detonative reaction. Therefore the occurrence of a DSDT event can result in total destruction of the solid propellant rocket motor assembly in the order of only milliseconds after the onset of granulation.

Since the employment of high secondary explosives in the propellant formulation is now taking place (to increase the specific impulse), there is a need to understand the criteria for a DSDT event to occur so the hazard can be

eliminated or at least avoided. In recent years there has been an increasing amount of research in this particular area of hazards. At the University of Illinois, under the direction of Professor Herman Krier, an effort has been made for over a decade to investigate the occurrence of a Deflagration to Shock to Detonation Transition in cyclotetramethylene tetranitramine (HMX, octogen). Examples of previous studies are given in references [1-4]. The research in this study is an attempt to delineate a DSDT event from the onset of compression waves propagating into the propellant bed to an eventual steady detonation.

1.1 Related Published Work

As mentioned, here at the University of Illinois, Krier and co-workers have extensively examined the possibility of DSDT occurring as a result of convective flame propagation through granular propellants [1-4]. The propagation sequence of events can be summarized as follows. First, pressure gradients develop in the granular bed from the localized burning of propellant fragments. To conserve momentum, the hot product gases are driven through the cracks between the propellant fragments. Convective heat transfer from the product gases to the surface of particles ignites more fragments, which in turn increase the pressure gradients. As more and more fragments are ignited the pressure gradients increase in magnitude eventually leading to shock initiation of the detonation of the unreacted propellant. This process of events is referred to by some as the accelerated convective burn model, developed by Butler, Lembeck and Krier [4]. In brief, the rapid pressure rise, fueled by particle ignition from convective heat transfer, appears to be the primary action that leads to detonation.

On the other hand, Campbell's investigation [5] suggested that convective flame spreading was essential only in the early stages of DSDT. He suggested that the stress waves produced by the burning fragments propagate ahead of the flame front and subsequently cause detonation. As the pressure gradients increase, stronger compression waves propagate and coalesce with earlier waves to form and continually strengthen the shock prior to detonation. Campbell went on to hypothesize that once a critical pressure was reached the pores would collapse between the fragments and cause a solid plug to form. The plug would continue to grow until the shock wave was strong enough to initiate detonation and in some instances detonation.

To validate his theory experimentally, Campbell packed a thick walled steel pipe with granulated HMX and inserted one or more neoprene diaphragms at various locations throughout the interior of the column. The neoprene disks completely covered the cross-sectional area of the pipe, preventing penetration of the hot product gases beyond the location of the disk. For various degrees of fineness of granulated HMX, the experiments showed detonation does occur ahead of the disk and in advance of the convective flame front. Figure 1.1 delineates the procession of the stress wave as time increases, brought forth by the burning propellant fragments, in times t_1 through t_5 . At time t_5 , the stress wave has advanced ahead of the first disk. Subsequently, the figure portrays at times t_6 and t_7 , the detonation wave traveling through the granulated bed. Furthermore, for the same effective diameters, experimental runs were made, absent of the neoprene disks, with coinciding run-up to detonation distances. In summary, Figure 1.2 depicts the measured run-up length to detonation for HMX granulated beds, with and without interval barriers.

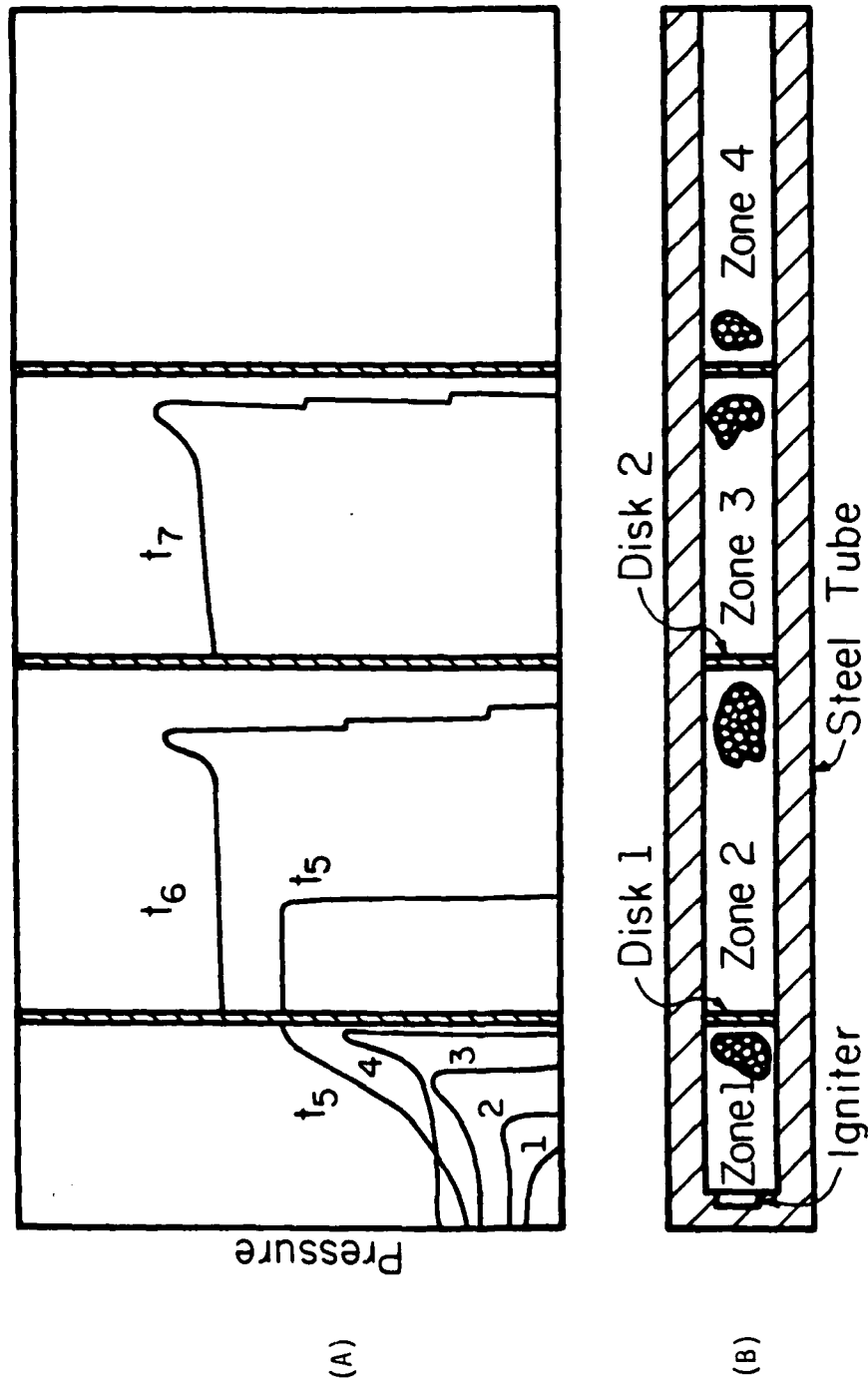


Figure 1.1 Part A: Schematic of Campbell's experiment [5] and illustration of assumed pressure - x-location profiles.
 Part B: The burning granular propellant in Zone 1 shock initiates the propellant in Zone 2.

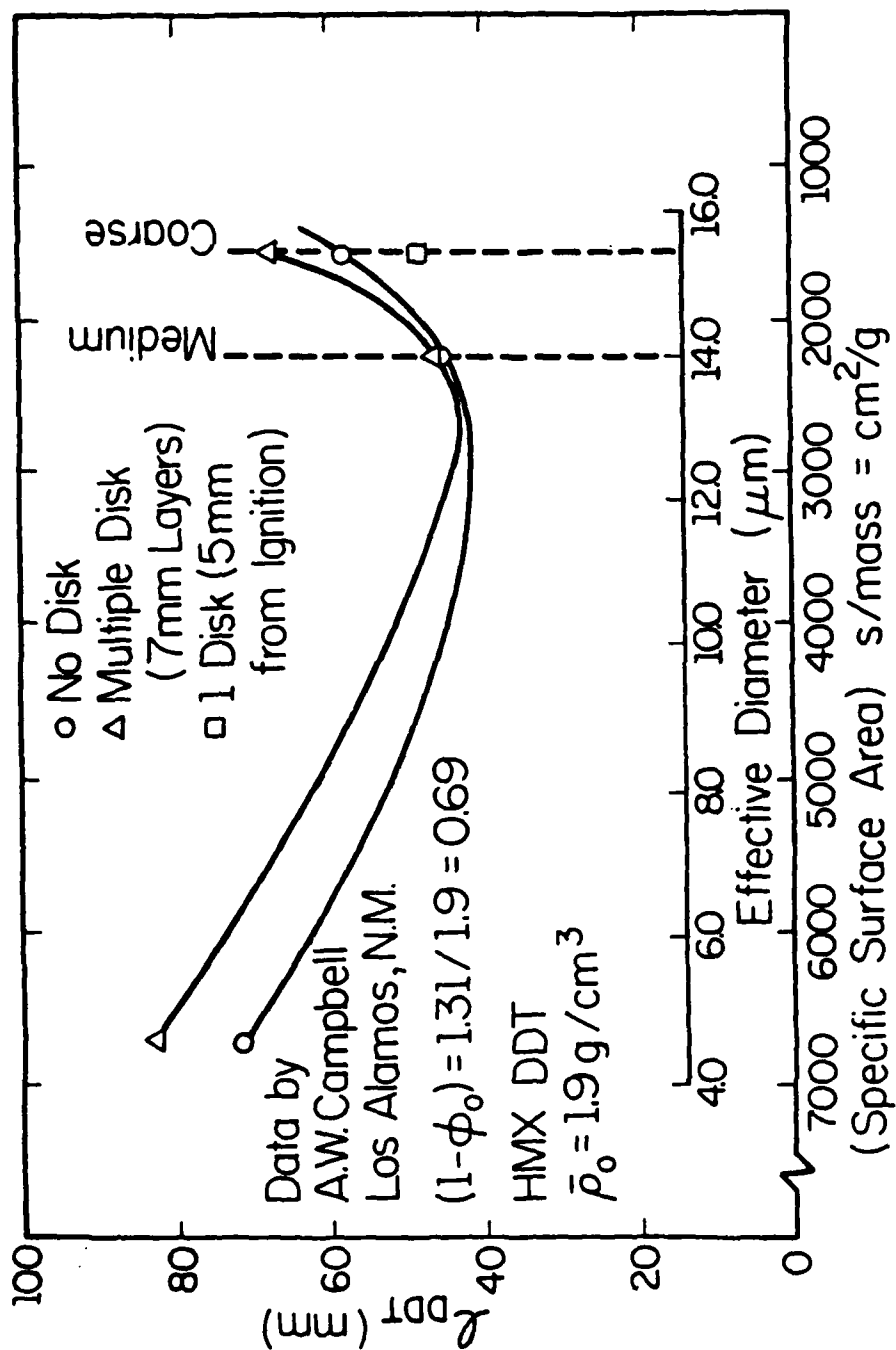


Figure 1.2 Summary of Campbell's data [5] showing detonation

Unlike Campbell [5], Macek [6] and Tarver [7] et al. studied DSDT in homogeneous solid explosives. Macek ran a series of experiments in which heavily confined cast cylinders of dithytnitramine dinitrate (DINA) and 50/50 pentolite were thermally ignited by an electrical source. The pressure rises observed in the experiments by Macek were approximated by an exponential, $P = 0.08 \exp(0.1 t)$, where pressure, P , and time, t , had units of gigapascals and microseconds, respectively. Moreover, Macek used a simplified model to serve as a prototype of explosive burning under confinement. The model employed a linear burn rate at the plane of deflagration, which is normal to the direction of the propagation of the flame, that separates the product gases from the unreacted explosive. Accordingly, the method of characteristics was utilized to obtain theoretical verification for the experimentally observed run-up distance to detonation. The point of coalescence of the right-running characteristics, as shown in Figure 1.3 was conjectured to be the point of formation of the shock which consequently initiates detonation.

However, Jacobs [8] found that Macek [6] had neglected to include the compressibility of the material, and with this correction in the model, his recent calculations infer that conductive burning could not have produced a shock wave. Both Jacobs [8] and Tarver [7] concluded that a mechanical means of increasing the burning surface must exist to obtain exponential burning rates that exceed the expected normal rates by several orders of magnitude. Hence, Anderson and Kooker [9] postulated that deconsolidation of a slightly porous material could occur through confined burning by shear-induced stresses, thus creating a greater surface to volume ratio.

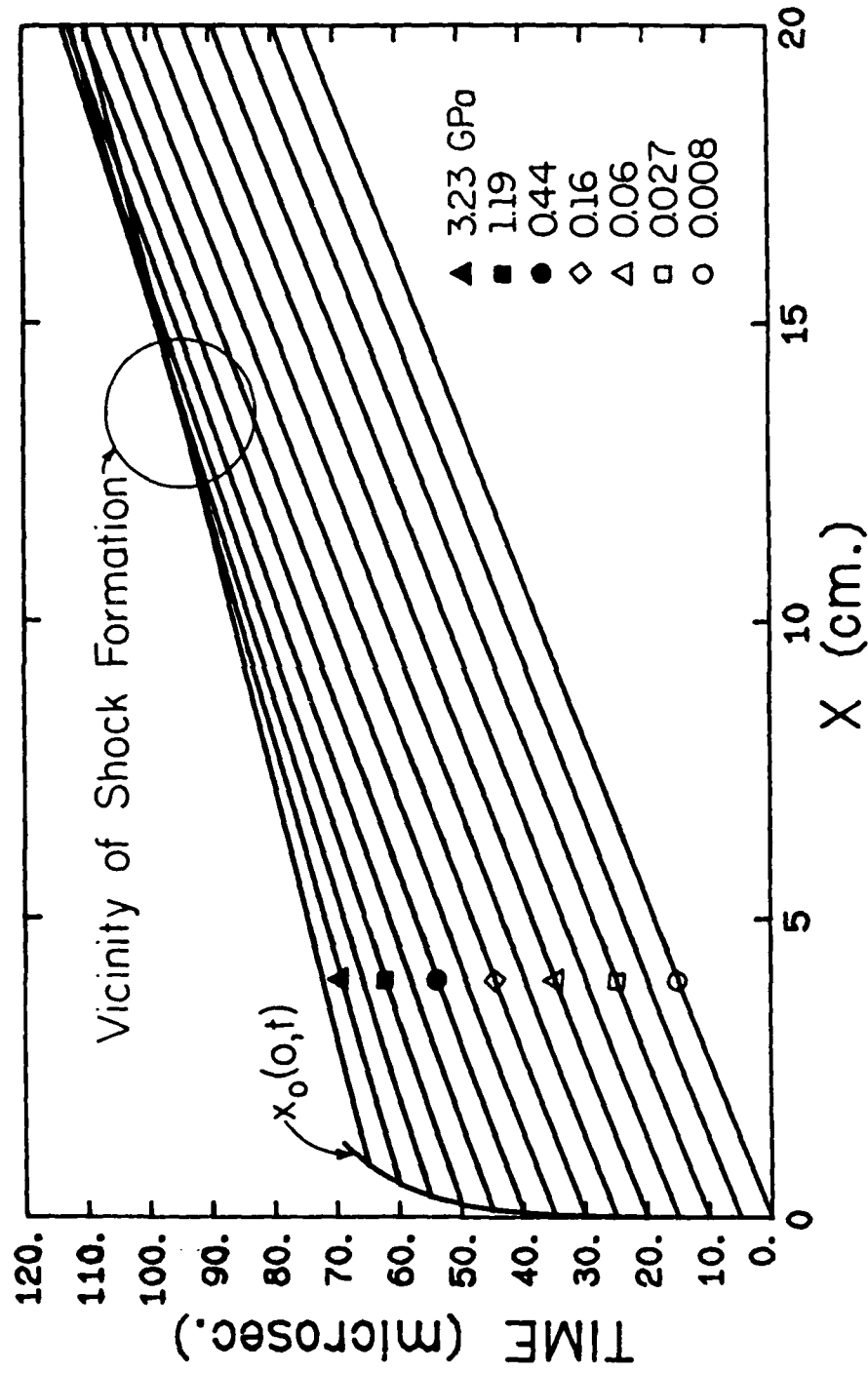


Figure 1.3 Lines of constant stress in homogeneous material (HMX) being stressed at $x=0$, taken from Reference [10].

Recently Coyne, Butler and Krier [10] studied the propagation of stress waves into porous HMX. During their investigation they found it difficult to employ the method of characteristics while utilizing a version of the more realistic Mie-Grünsien equation of state. Instead they used the Tait equation of state, which does not properly represent the isentrope, to obtain a numerical solution of the conservation equations by a Lagrangian finite differencing technique. This solution was to be verified by comparing results to those obtained by the method of characteristics. Depicted in Figure 1.4 are the results of the comparison. Eventually the modified Mie-Grüneisen relation was incorporated in the finite difference code to model stress wave propagation in a porous nonreactive material.

The "Pop-plot" is named after its originator, Nickalous Popaloto, and delineates the shock pressure strength to run-up distance to detonation on a log-log scale. Figure 1.5 is an example of a "Pop-plot" which was obtained by Dick [11] for porous HMX. Due to the hazards associated when experimenting with explosives and the difficulties in obtaining accurate results, there is little data on run-up distances to detonation for granular explosives. However, using a data acquisition technique different from the standardized wedge test, J. J. Dick obtained "Pop-plot" data for porous samples of HMX of initial density $\rho_0 = 1.24 \pm 0.04 \text{ g/cm}^3$ [11]. The wedge test records the trajectory of a shock as the wave travels through a wedged shaped sample by photographic techniques. Different from the standardized test, Dick measured only the total time that the wave resided in the cylindrical sample, thereby producing a "Pop-plot" through extensive runs and statistical analysis.

Setchell [12] also ran experiments on initiation behavior of granular explosives. Utilizing Laser Velocity Interferometry, Setchell studied "ramp"

Comparison of Stress Wave Propagation
using the Tait E.O.S.

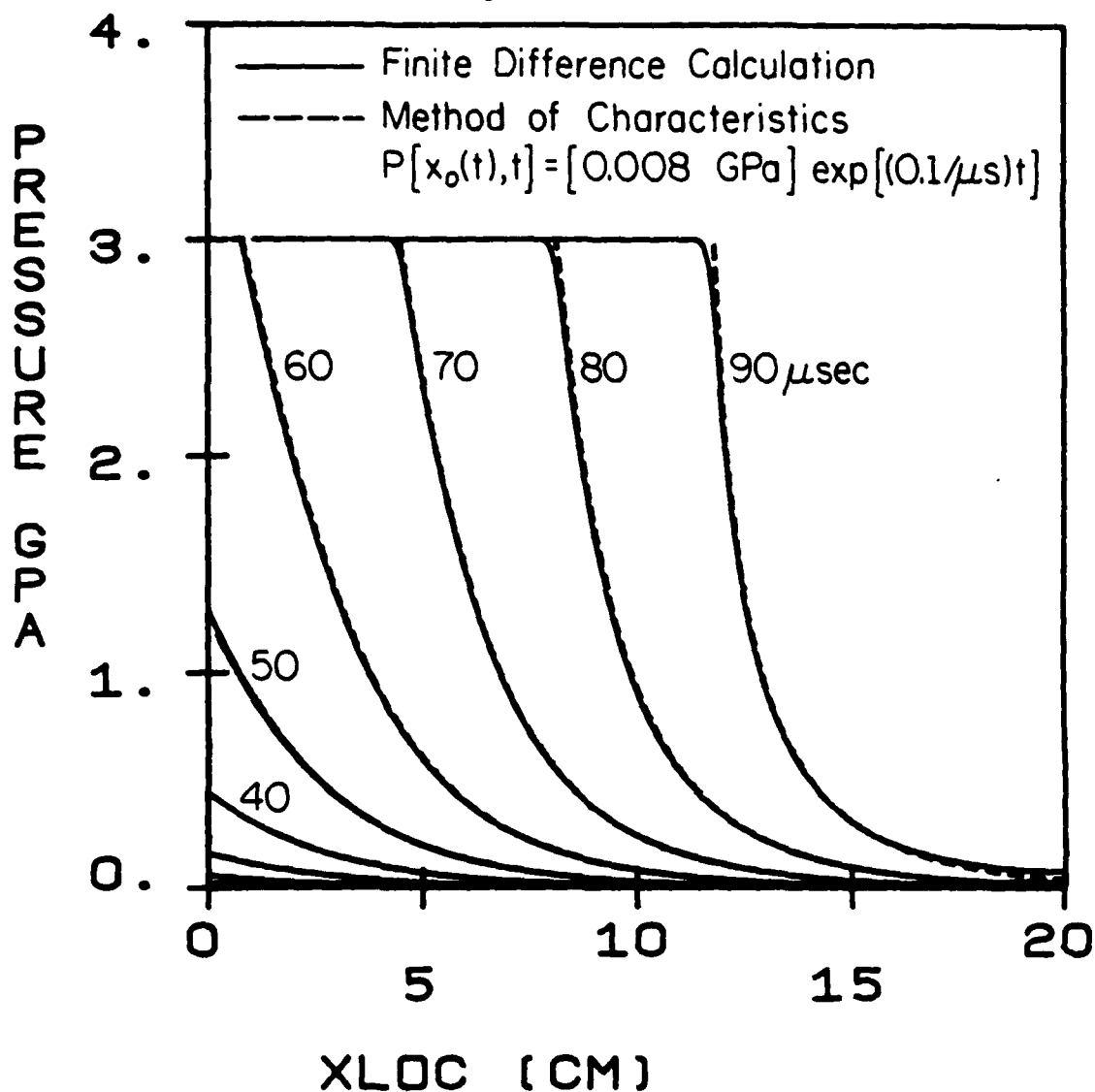


Figure 1.4 Stress wave propagation through solid HMX, from both the finite difference calculation and the method of characteristics. Both utilizing the modified Tait equation of state. Figure taken from Reference [10].

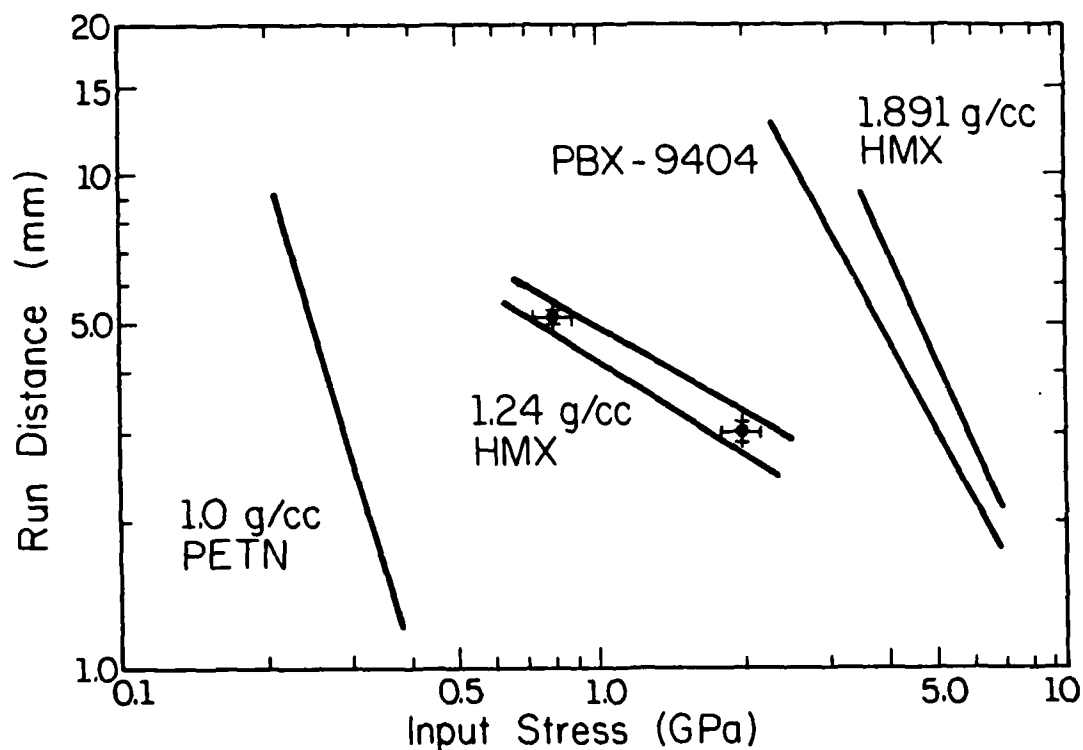


Figure 1.5 Run-up distance to detonation versus input stress for several high-explosives. Uncertainty bars for run-up distance represent one and two standard deviations. Data for HMX (1.24 g/cc) is from Reference [11]. Data for PETN, PBX-9404, HMX (1.89 g/cc) is from Reference [31].

"ramp" waves having a finite rise-time of either 0.3 or 0.8 microseconds. By shock loading pyroceram, a material known to have stress-strain relation with negative curvature, he was able to disperse a shock wave into a wave having a finite rise time. Setchell found, by comparing velocity-time profiles of tests on PBX-9404 shocked to the same peak pressure, that very little chemical energy was released in the tests with ramp waves prior to shock formation. His records indicate that local hotspot generation and ignition are strongly inhibited by finite rates of compression.

1.2 Hot Spot Theory

Although the theory of hot spots as a source for ignition in porous material is widely accepted, there is very little conclusive evidence on the matter of generation. Some of the hypotheses for hot spot generation are shear banding, jetting, shock focusing, and/or adiabatic compression. For more detailed information, see to References [13-16]. Hayes [17] suggests that the total energy deposited by the shock wave can be equated on a mass fraction basis to the sum of the reversible work done in isentropically compressing the bulk of the material plus the irreversible heating of localized hot spots, i.e.,

$$\frac{P + P_0}{2} (v_{T0} - v_T) = W_H e(v_T, T_H) + (1 - W_H) e_I(P) \quad (1.1)$$

In equation (1.1) the left-hand side represents the total energy deposited in the material by the shock of strength, P . The term $e_I(P)$ represents the energy required to isentropically compress the bulk of the material to the final shock pressure, and the remaining energy term, $e(v_T, T_H)$, is the energy

available to irreversibly heat the hot spots. The Hayes model assumes the mass fraction of the hot spots, W_H , to be equal to the preshock specific volume fraction of pores

$$W_H = v_{T0}/v_{S0} - 1 \quad (1.2)$$

Here, the subscript 'T0' represents the initial porous state, and the subscript 'S0' refers to the homogenous initial state. Furthermore, Hayes [17] states that scissing of particular chemical bonds, stemming from the high frequency content in the shock front and the construction of a non-equilibrium temperature, can be responsible for the increase in reactivity and subsequently the decrease in decomposition times for the hot spots observed in his experiments. Figure 1.6 compares the observed decomposition times for hexanitrostilbene (HNS) to times derived from low-temperature Arrhenius kinetics for a hot spot temperature regime. Consequently, the explosion model fails to predict corresponding decomposition times and falls away by a bigger margin as temperature of the hot spots decrease.

1.3 Scope of Our Study

As previously mentioned, only if there is fragmentation of the propellant bed in the burning region, along with proper confinement, will there be sufficient pressurization rates to shock initiate detonation for cast explosives [18]. Consider a rocket motor with a center burning grain configuration as shown in Figure 1.7. To illustrate a DSDT event, a crack in the propellant grain is assumed, and within the crack a packed bed of fragments of known surface-to-volume ratio exist. The fragment filled crack

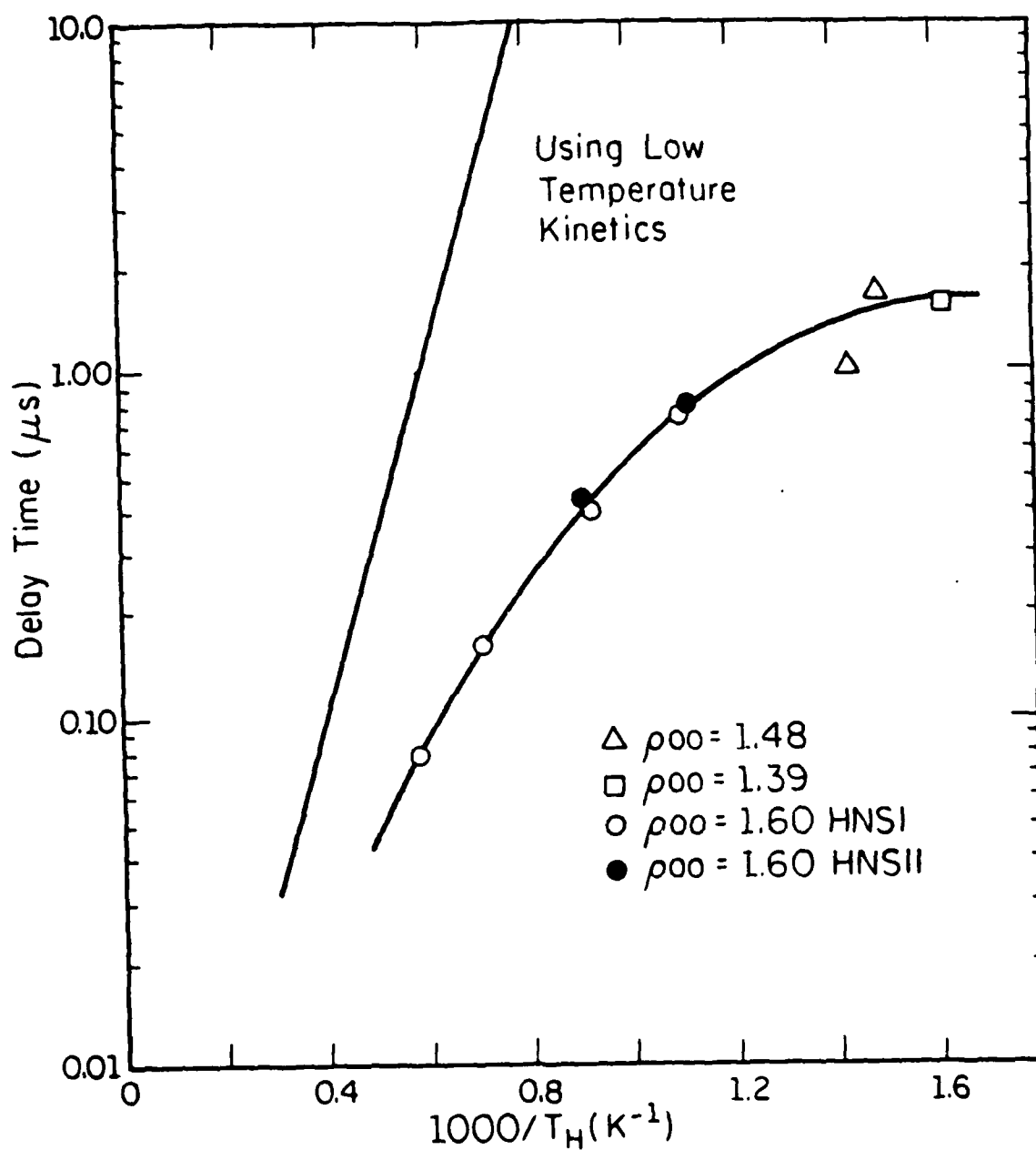
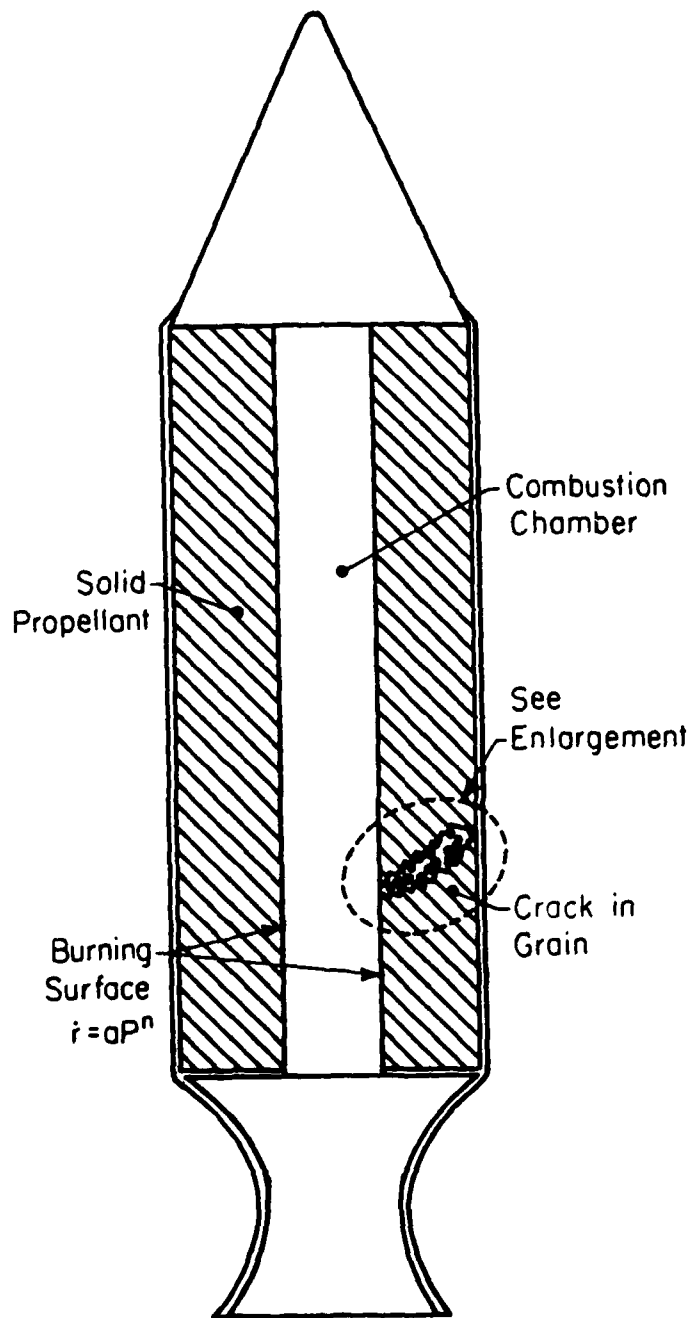


Figure 1.6 Experimentally observed and calculated hot spot decomposition times versus the hot spot temperature inverse for HNS. Figure taken from Reference [17].

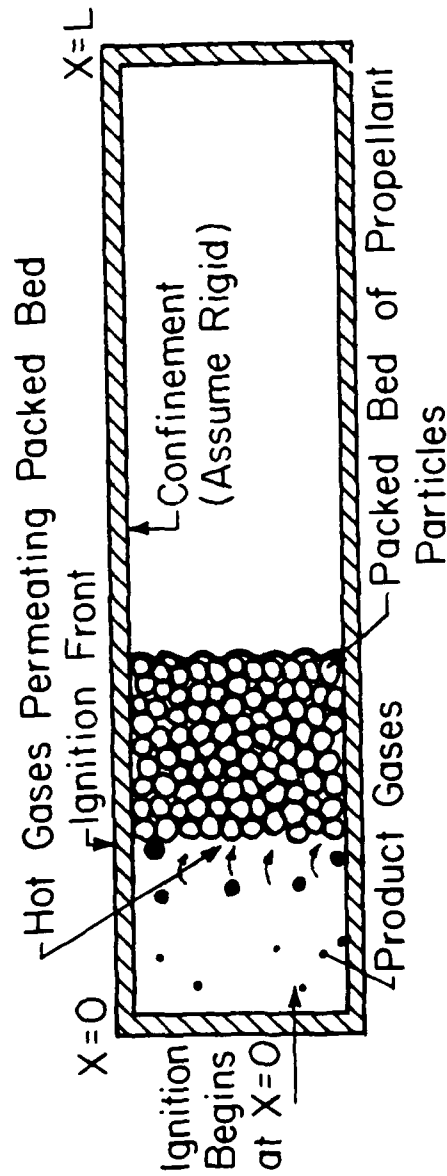


DSDT HAZARD IN ROCKET MOTOR

Figure 1.7 Sketch of solid propellant rocket motor with a crack indicated in the grain.

is enlarged and shown in Figure 1.8. At some arbitrary time, the bed ignites and starts burning at $x=0$ (left-end of figure). Increased product gas generation beyond the level necessary for steady state motor operation originates from the assumed high surface-to-volume ratio of confined sub-millimeter size particles. In other words, the amount of gas being generated by the decomposing propellant far exceeds the amount exiting the nozzle.

If the length of the packed bed is longer than the critical condition for accelerated convective combustion to occur, subsequent detonation is inevitable [19]. However, if the bed length is less than the critical length, pressure gradients produced by the granulated propellant can provide the impetus to shock initiate detonation in the adjacent region of cast explosive, depicted as zone 1 in Figure 1.9. Only stress waves can be transmitted across the zone2/zone1 interface. Even though the solid may contain pores, it is assumed to be impermeable to the flow of hot gases. A schematic representation of the sequence of events leading to Deflagration to Shock to Detonation Transition modeled in this study is shown in Figure 1.10. A value of ϕ equal to unity represents a zone of all gas, while ϕ equal to zero indicates a homogeneous solid. In Figure 1.10, the heavy black dots are representative of microvoids in the cast material. Illustrated in Part B is the collapse of the pores, a result of the stress load transmitted across the granulated bed/cast explosive interface. Parts C and D show the length of the pore collapse zone to increase with time as the lead compression waves travel farther into the explosive. The finite compression waves coalesce into a shock front which then initiates the cast explosive downstream of the interface. From this location a detonation wave propagates through the porous material, while a detonation wave propagates back through the compressed material (Part E).



DSDT IN PACKED BED

Figure 1.8 Enlargement of granulated bed formed in the solid rocket motor, refer to Figure 1.7. Black dots represent reacting particles.

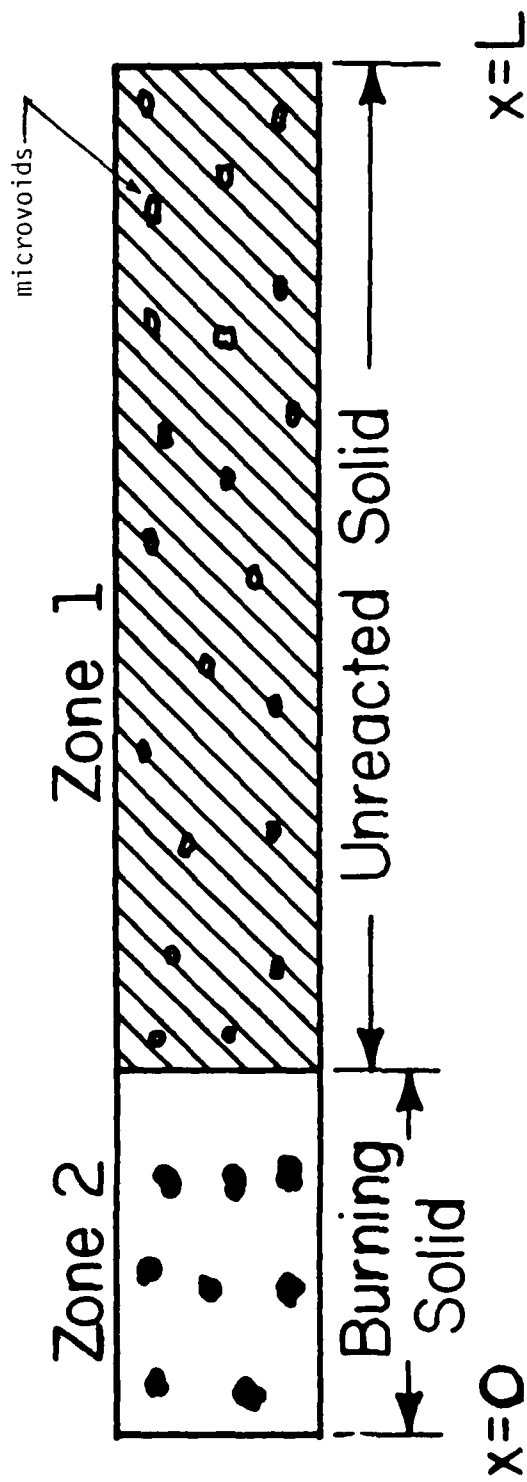
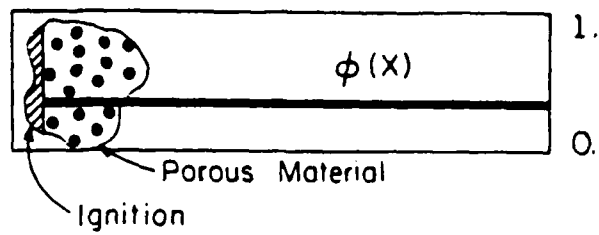
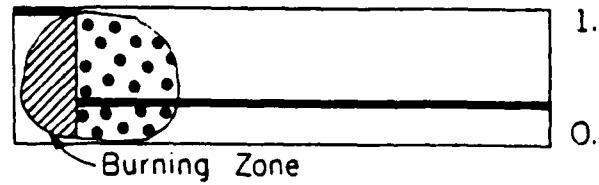


Figure 1.9 Sketch of granulated bed/cast bed configuration.

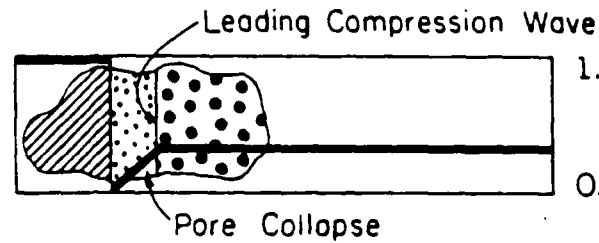
(A) Ignition



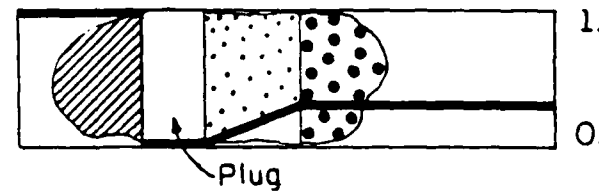
(B) Convective Flame Spreading



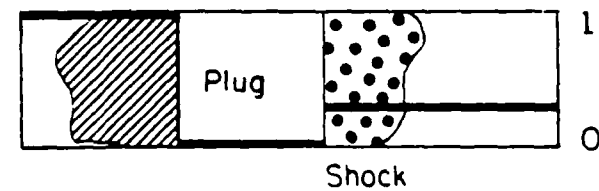
(C) Pore Collapse



(D) Plug Formation



(E) Shock Formation



(F) Shock Initiation (Detonation)

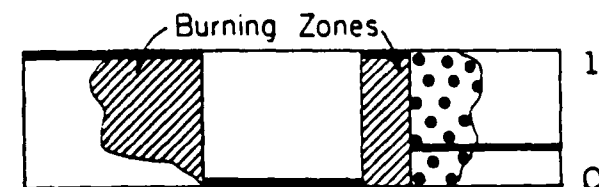


Figure 1.10 Proposed five-part sequence of events leading to DSDT.

The purpose of the research study here is then to model the key elements of the five part scenario. A one-dimensional hydrodynamic Lagrangian finite difference technique is used to numerically solve the conservation equations of mass, momentum, and energy. A pore collapse theory derived by Carroll and Holt [20] which demarcates three regimes of deformation, elastic, elastic-plastic, and plastic is utilized to determine the rate of compaction and the development of the solid plug. Basically, this portion of the code is an extension on previous work done by Coyne [21]. Furthermore, the Hayes hot spot theory is incorporated in the code to define the sensitivity to reaction. By introducing reactive chemistry to the code, a strong effort is made to model the detonation and retonation waves which are initiated by a shock wave generated from ramp wave inputs with rise times on the order of tens of microseconds. It was shown in Reference [19] that rise times of this order are typical for burning, granulated beds which have lengths less than their critical detonation run-up length. Although, Setchell [12] also studied ramp waves, the rise times were faster by an order of magnitude.

CHAPTER 2

MATHEMATICAL AND NUMERICAL ANALYSIS

The equations which mathematically model shock initiation to detonation due to a rapid compression of high explosive containing voids are presented in the sections to follow. Specifically, the material being considered here is HMX, requiring specific constitutive relations. Properties for HMX are listed in Appendix A. The model clearly can be applied to other reactive solids, but an equation of state, a caloric relation, and the material Hugoniot must be known.

2.1 Free Boundary

The first step taken to model DSDT in a porous explosive solid was to determine the pressure gradients produced by the adjacent reacting granulated bed, Zone 2 in Figure 1.9. An analysis by Butler and Krier described in Reference [4], models the accelerating convective burn and rapid pressurization for granulated beds of explosives.

Figure 2.1 presents the predicted pressure rise rate at one location in such a bed. The bed length is always less than the required run-up distance to detonation, λ_{CJ} . Notice that the pressurization rate is strongly dependent on particle size, increasing, as one would expect, with smaller propellant fragments. Subsequently, the rate at which the impermeable bed is being stressed (assuming that such a bed is adjacent to the porous, permeable bed) is defined by the pressure-time functions predicted by the Deflagration to Detonation Transition case documented in Reference [19].

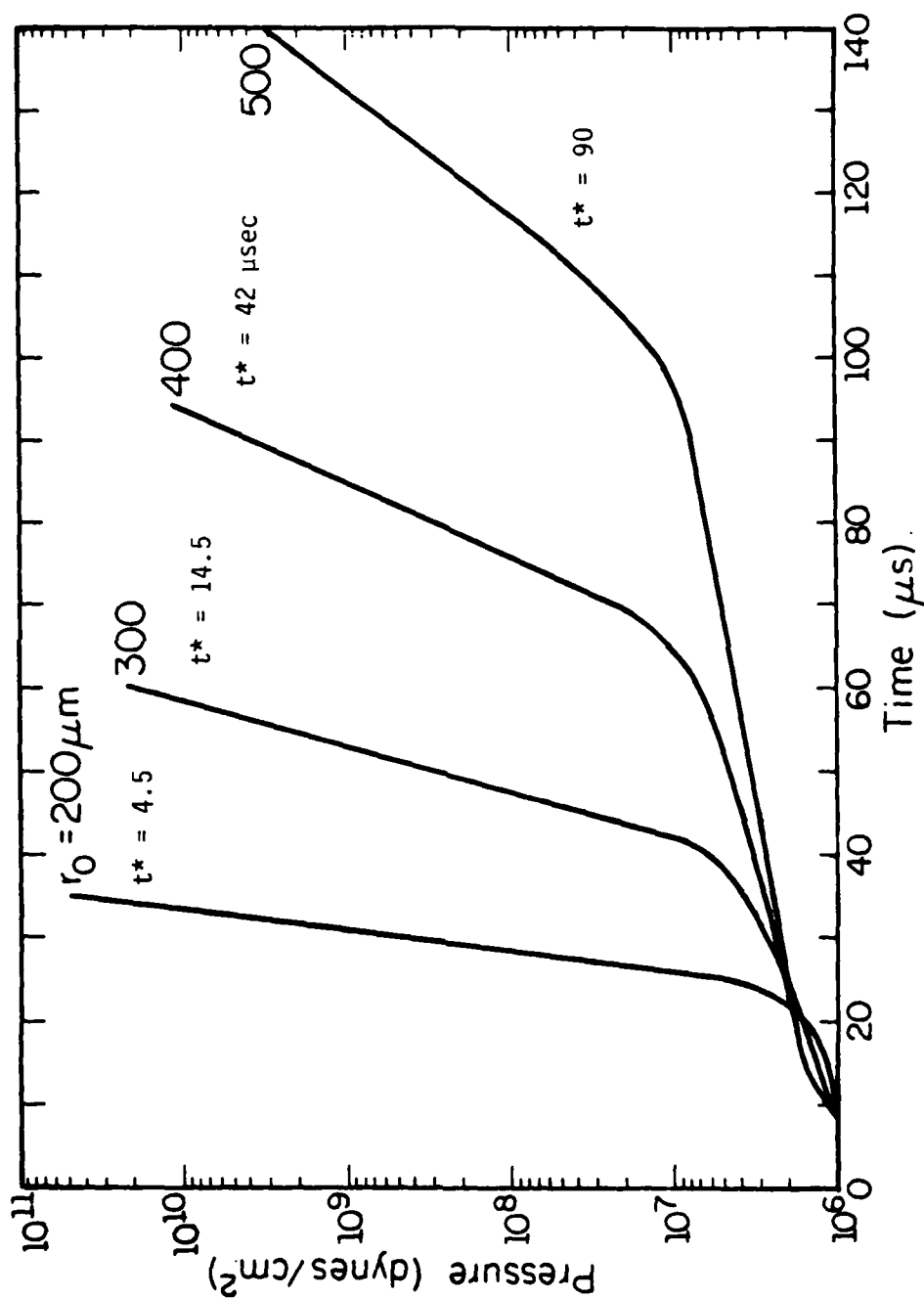


Figure 2.1 Pressure-rise rates in a granular bed of HMX ($\alpha_0 = 1.4286$) predicted by the code in Reference [19].

The pressure-time function here is approximated by a linear p-t relation, with the slope a specific function of the material properties. Therefore to simplify the loading boundary condition at the granulated/cast bed explosive interface, the pressure magnitude of the left free boundary was assumed to satisfy

$$P(t) = (P^* - P_0)(t/t^*) + P_0 \quad t \leq t^* \quad (2.1a)$$

$$P(t) = P^* \quad t \geq t^* \quad (2.1b)$$

Here P^* is the maximum pressure applied to the left boundary, while t^* is the characteristic rise-time for the "ramp" wave to reach the maximum stress at the free boundary. It should be noted that a typical range of t^* includes the interval $1 < t^* < 50$ microseconds. Thus this type of "ramp-loading" is much slower than the "ramp" wave compressions of explosives studied by Setchell [12], where $0.3 < t^* < 0.8$ microseconds. A shock loading to P^* is usually assumed to be $t^* < 0.01$ microseconds.

2.2 Governing Equations

For our hydrodynamic analysis the Lagrangian or material form of the governing equations was chosen, instead of Eulerian form. The Lagrangian coordinates are fixed to the material and follow this material as it moves with time, whereas the Eulerian coordinates are a fixed frame of reference, where mass, momentum, and energy may enter or exit through the control surfaces. Therefore, with the Eulerian formulation, the boundary location must be implicitly determined after each time increment. However, with the Lagrangian description, the location of the free boundary condition is

explicitly known, since the Lagrangian boundary coordinates move with the material boundary.

The inviscid Lagrangian one-dimensional unsteady form of the conservation of mass, momentum, and energy equations are expressed for total mechanical mixture, respectively as

$$\frac{\partial v}{\partial t} = v \frac{\partial u}{\partial h} \quad (2.2)$$

$$\frac{\partial u}{\partial t} = -v \frac{\partial P}{\partial h} \quad (2.3)$$

$$\text{and} \quad \frac{\partial e}{\partial t} = -P \frac{\partial v}{\partial t} + Q \quad (2.4)$$

In equation (2.2 - 2.4), v represents the specific volume; u , particle velocity; e , the specific internal energy; P , the total stress; and Q , the heat added by chemical reaction per unit mass per unit time. The symbols $\frac{\partial}{\partial h}$ and $\frac{\partial}{\partial t}$ indicate the partial derivatives with respect to the Lagrangian spatial coordinate and time, respectively. For comparison purposes, the Eulerian form of the conservation of mass, momentum, and energy equation, respectively, would be,

$$\frac{\partial v}{\partial t} = -u \frac{\partial v}{\partial x} + v \frac{\partial u}{\partial x} \quad (2.5)$$

$$\frac{\partial u}{\partial t} = -u \frac{\partial u}{\partial x} - v \frac{\partial P}{\partial x} \quad (2.6)$$

$$\frac{\partial e}{\partial t} = -u \frac{\partial e}{\partial x} - Pu \frac{\partial v}{\partial x} - P \frac{\partial v}{\partial t} + Q \quad (2.7)$$

where the symbol $\frac{\partial}{\partial x}$ denotes the partial derivative with respect to the Eulerian spatial coordinate. Notice that equations (2.5 - 2.7), in absence of the convective flux terms, are identical to equations (2.2 - 2.4). Since the same mass is contained in a given Lagrangian control volume throughout the variation of time the convective flux terms do not appear in equations (2.2 - 2.4).

Generally, the Lagrangian form of the governing equations are easier to incorporate into a numerical solution technique, since it is clear that they are in a simpler form than the Eulerian, and, most importantly, one has the advantage when dealing with a free or moving boundary condition. To provide mathematical closure to the governing equations, for an inert material, an equation of state is needed, since the three equations (2.2) to (2.4) involve four unknowns.

2.3 Constitutive Relations

From the Second Law of Thermodynamics, there exists a unique relationship between the material equation of state, $P_S(v_S, T_S)$, and the caloric equation of state, $e_S(v_S, T_S)$. One way of relating the two state equations is through Helmholtz free energy function and its thermodynamic derivatives. Therefore $P_S(v_S, T_S)$ and $e_S(v_S, T_S)$ must satisfy the reciprocity relations.

$$P_S = - \frac{\partial \psi}{\partial v_S} \quad (2.8)$$

$$e_S = \psi - T_S \frac{\partial \psi}{\partial T_S} \quad (2.9)$$

In equations (2.8) and (2.9), T represents temperature, P , pressure, e , specific internal energy, v , specific volume, and ψ Helmholtz free energy.

The subscript s denotes a solid material, while the symbols

$\frac{\partial}{\partial v}$ and $\frac{\partial}{\partial T}$ indicate partial derivatives with respect to specific volume and temperature, respectively. Appendix B gives a review of these fundamental thermodynamic concepts.

With the assumption that the Gruneisen coefficient, Γ , is constant, the Helmholtz free energy function is expressed in the following form (Baer and Nunziato [22]).

$$\begin{aligned} \psi(v_s, T_s) = & J(v_s) + \Gamma C_{v_s} \ln\left(\frac{v_{s0}}{v_s}\right) (T_s - T_{s0}) \\ & + C_{v_s} \left[T_s \ln\left(\frac{T_{s0}}{T_s}\right) + T_s - T_{s0} \right] \end{aligned} \quad (2.10)$$

where c_{v_s} represents the specific heat at constant volume of the solid phase which is also assumed to be a constant. The term $J(v_s)$ in equation (2.10) is a nonlinear volume-dependent function determined from shock Hugoniot experiments [22].

The Gruneisen coefficient is defined by the thermodynamic derivative

$$\Gamma(v) \equiv -v \left(\frac{\partial P}{\partial e} \right)_v \quad (2.11)$$

which characterizes the ratio of thermal pressure to the thermal energy of the lattice. At standard volume, the Gruneisen coefficient, $\Gamma_0 = \Gamma(v_0)$, of a material can be related to other properties, such as the isothermal compressibility of the material at standard conditions, κ_0

$$\kappa_0 = -\frac{1}{v_0} \left(\frac{\partial v}{\partial p} \right)_T \quad (2.12)$$

and the coefficient of thermal expansion at constant pressure, κ_p

$$\kappa_p = \frac{1}{v_0} \left(\frac{\partial v}{\partial T} \right)_p \quad (2.13)$$

Thus an expression can be obtained for the Gruneisen coefficient at standard volume, i.e.,

$$\Gamma_0 = \frac{v_0 \kappa_p}{c_v \kappa_0} = \frac{\kappa_p}{\rho_0 c_v \kappa_0} = \frac{\kappa_p c_0^2}{c_v} \quad (2.14)$$

where c_0 is the ambient sound speed of the material.

Although equations (2.2-2.4, 2.8 and 2.9) form a basis for the mathematical description of a homogeneous material, an additional relation is needed to describe a heterogeneous material. Porosity is defined as the ratio of total volume of the material to the volume occupied by the solid phase, or

$$\alpha \equiv \frac{V_T}{V_S} \quad (2.15)$$

Initially, the volume not occupied by the solid material is assumed to be massless. With the introduction of porosity an additional equation is needed to complete the mathematical description.

Extensive research in the area of mathematically modeling the collapse of a porous material under an applied external load has been performed by Carroll and Holt [20]. In their model the porous matrix is exemplified as a hollow

sphere where the inner and outer radii are chosen such that the overall porosity of the material is accurately portrayed. As previously mentioned in Chapter 1, the model of Carroll and Holt [20] assumed pore collapse to occur in three distinct regimes: (1) elastic phase, where elastic deformation in the solid takes precedence, (2) elastic-plastic phase, where plastic deformation initially starts at the inner radius and subsequently progresses outward until plastic deformation begins to occur at the outer radius, and (3) plastic phase, where plastic deformation occurs throughout the sphere. The so called "P - α relations" for the three particular phases of compaction and the appropriate range over which each applies are given by,

elastic phase $\alpha_0 \geq \alpha \geq \alpha_1$

$$P = \frac{4}{3} \frac{G(\alpha_0 - \alpha)}{\alpha(\alpha - 1)} \quad (2.16a)$$

elastic-plastic phase $\alpha_1 \geq \alpha \geq \alpha_2$

$$P = \frac{2}{3} \gamma \left\{ 1 - \frac{2G}{\gamma\alpha} (\alpha_0 - \alpha) + \ln \left[\frac{2G(\alpha_0 - \alpha)}{\gamma(\alpha - 1)} \right] \right\} \quad (2.16b)$$

plastic phase $\alpha_2 \geq \alpha > 1$

$$P = \frac{2}{3} \gamma \ln \left(\frac{\alpha}{\alpha - 1} \right) \quad (2.16c)$$

where the limits between the three phases are expressed as

$$\alpha_1 = \frac{2G\alpha_0 + \gamma}{2G + \gamma} \quad (2.17)$$

$$\alpha_2 = \frac{2G \alpha_0}{2G + Y} \quad (2.18)$$

Kooker and Anderson [9] have also used the static pore collapse model with the yield stress, Y , and shear modulus, G , expressed as functions of α , namely,

$$Y = Y_0 / (2\alpha - 1)^2 \quad (2.19)$$

$$G = G_0 \exp [-5(\alpha - 1)/\alpha] \quad (2.20)$$

Here, Y_0 and G_0 are the initial yield stress and shear modulus, respectively. Figure 2.2, taken from Reference [21], illustrates the three regimes of deformation for various initial porosities. Notice that the plastic phase approaches unity, complete compaction. During *deformative* compression the pressure of the mechanical mixture is equated to the pressure of the solid

$$P = P_s \quad (2.21)$$

Thus, with the additional parameter α and the " $P - \alpha$ law", a mathematical description for a nonreactive porous material is complete.

The governing equations for the conservation of mass, momentum, and energy represented in Section 2.2 are written in terms of the thermodynamic properties (P, v, T, e) of the mechanical mixture as well as the dynamic variable u . However, during reaction additional relations are needed to separate the individual phase properties of the solid and product gases from those of the

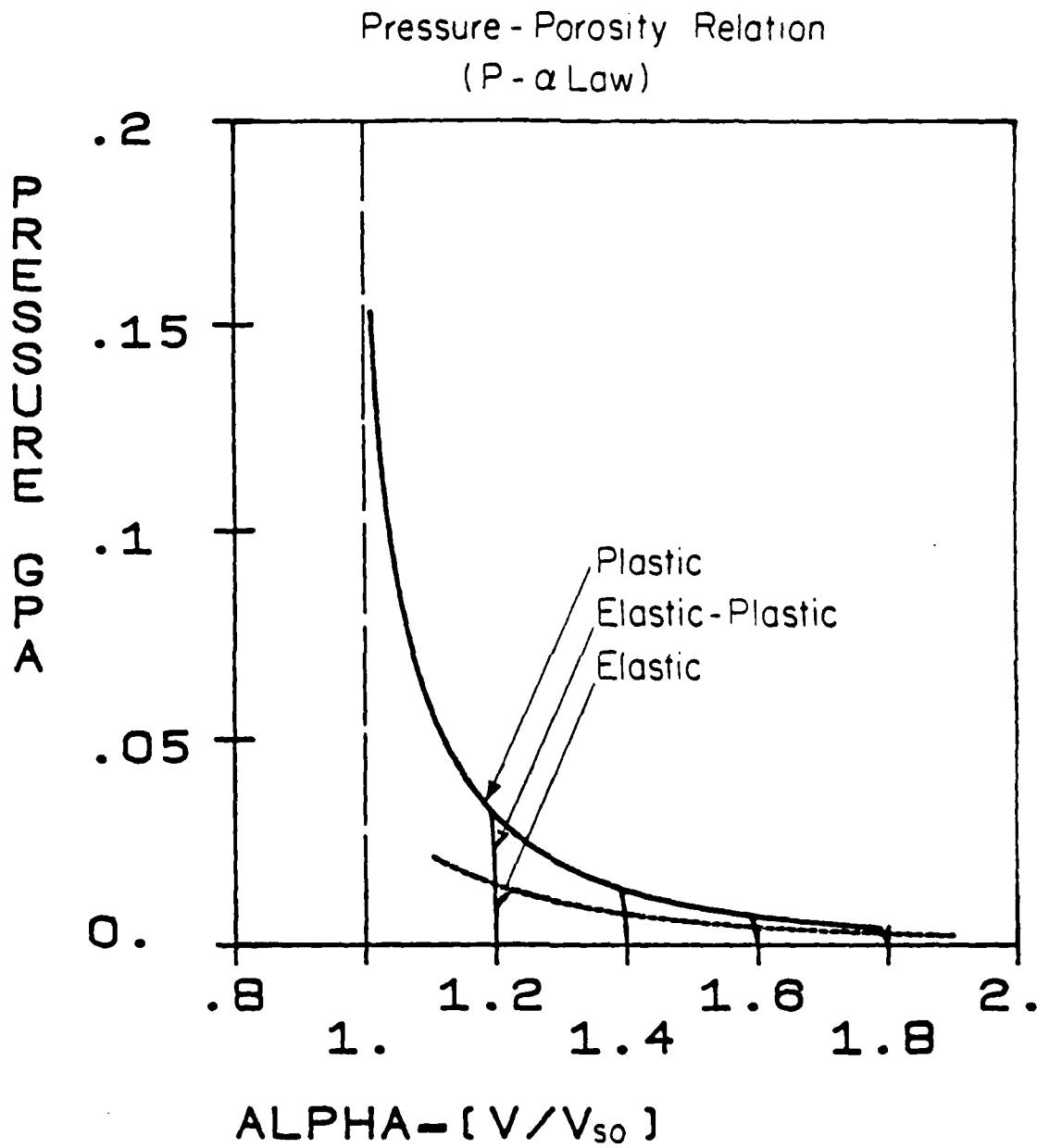


Figure 2.2 Pressure-void volume relationship for porous HMX.
Figure taken from Reference [21].

mixture. Hence, it is conjectured that any arbitrary volume, V_T , within the continuum can contain both the solid and gas phases. Therefore the individual phase volumes sum to the total volume, i.e.

$$V_T = V_g + V_s \quad (2.22)$$

Analogously, the total energy of the mechanical mixture, E_T , is the sum of the total energy of both the solid and gas phase, represented as

$$E_T = E_g + E_s \quad (2.23)$$

With the introduction of a product gas phase in the mechanical system, another constitutive equation must be prescribed. A nonideal covolume equation of state was chosen, similar to the one utilized by Butler and Krier [19], for the product gas phase, namely

$$P_g = \hat{R}T_g (1 + B/v_g)/v_g \quad (2.24)$$

where \hat{R} is the gas constant, and B is a covolume correction term. The value of B is determined from values for pressure, temperature, and density at the Chapman-Jouguet (CJ) state predicted by a thermochemical code, TIGER [23].

$$B = v_{CJ} \left(\frac{P_{CJ} v_{CJ}}{R T_{CJ}} - 1 \right) \quad (2.25)$$

A listing of the CJ values for several loading densities of HMX is given in Table [2.1]. In accordance with the reciprocity relations defined earlier

TABLE 2.1
CJ PARAMETERS PREDICTED BY TIGER [23]

α_0	ρ_{T0} (g/cc)	P_{CJ} (GPa)	T_{CJ} (K)	v_{CJ} (cc/g)	D (mm/ μ s)	β (cc/g)
1	1.9	35.99	3714	0.4073	9.154	5.192
1.056	1.8	31.70	3833	0.4266	8.711	4.815
1.118	1.7	27.97	3931	0.4478	8.301	4.522
1.188	1.6	24.72	4009	0.4713	7.925	4.300
1.267	1.5	21.86	4067	0.4977	7.581	4.139
1.357	1.4	19.30	4106	0.5278	7.267	4.034
1.462	1.3	17.00	4126	0.5627	6.979	3.982

(Equations 2.8-2.9), the caloric equation of state for the product gas phase is expressed as

$$e_g = c_{vg} (T_g - T_{go}) \quad (2.26)$$

where c_{vg} is an assumed constant which represents the specific heat at constant volume of the gas phase. Furthermore, while chemical reaction is present the additional assumptions,

$$P = P_s = P_g \quad (2.27)$$

$$T = T_s = T_g \quad (2.28)$$

are imposed.

2.4 The Localized Hot Spot Temperature

Before specifically discussing the hot spot temperature, it is first important to compare the relative amount of energy associated with shocking a porous material compared to that associated with shocking a homogeneous material. The text by Zeldovich and Raizer [24] provides detailed background. Figure 2.3 taken from Reference [21] delineates the Hugoniot for both a porous and homogeneous matrix of HMX compressed to a volume ratio of $v/v_{s0} = 0.9$. In Figure 2.3 the horizontally shaded area ABC and the crosshatched area A'B'C show the increase in energy of a shocked porous and homogeneous material, respectively. The significant increase in energy associated with shocking a porous material compared to a homogeneous material is conjectured to be the cause for a porous material to be more sensitive to shock initiation of the detonative reaction than a homogeneous material.

Shock Hugoniots of Solid and Porous HMX

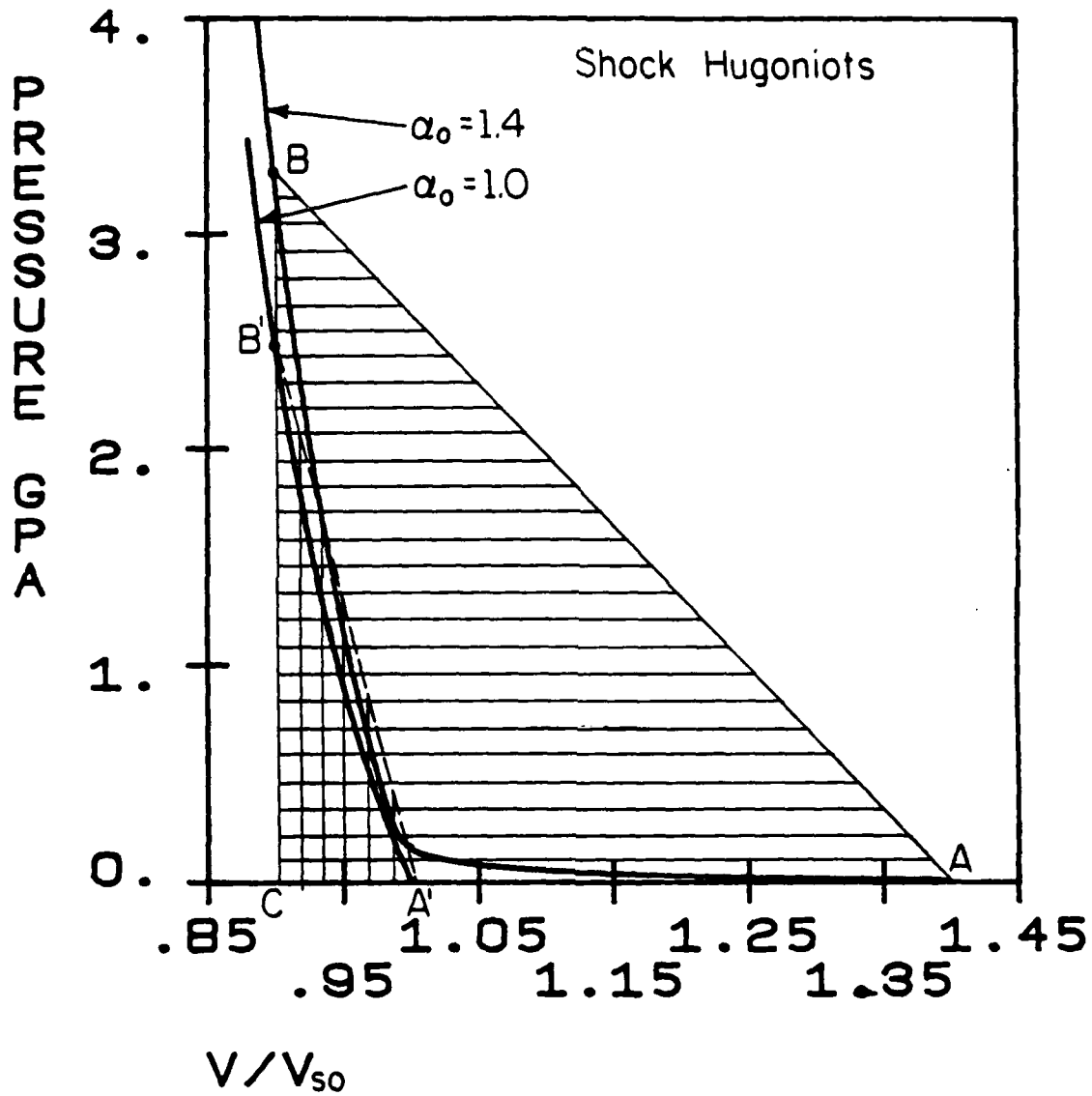


Figure 2.3 Shock Hugoniots for solid and porous HMX compressed to a volume ratio of $v/v_{so} = 0.9$, taken from Reference [21].

Referring back to Figure 1.5, a "Pop-plot" for various propellants, one can see verification of this. Note the significant decrease in run-up distance to detonation for a porous material compared to a nearly homogeneous material, shocked to the same peak pressure. In addition, triangle ABA', shown in Figure 2.3, is representative of the amount of irreversible energy deposited by shocking a porous material.

As mentioned previously in Chapter 1, the theory developed by Hayes [17] suggests that the total energy deposited by the shock can be equated by the reversible work done in compressing the bulk material plus the irreversible heating of the localized hot spots. The Equations (1.1 and 1.2) underlying the theory, are rewritten as

$$\frac{P+P_0}{2} (v_{T0} - v_T) = W_H e_s(v_s, T_H) + (1-W_H) e_s(v_s, T_I) \quad (2.29)$$

$$\text{and} \quad W_H = \frac{v_{T0}}{v_{s0}} - 1 \quad (2.30)$$

where T_H represents the hot spot temperature. For a porous material, the total energy of the mechanical mixture is assumed to equal the total energy of the solid. Therefore, the isentrope energy, $e_I(P)$, can be expressed as

$$e_I(P) = e_s(v_s, T_I) \quad (2.31)$$

where T_I is the temperature defined by isentropic compression. A relation for the isentropic temperature is obtained from Reference [24] and is written as

$$T_I = T_0 \left(\frac{v_{s0}}{v_s} \right)^{\gamma_0} \quad (2.32)$$

With this formulation one can calculate the hot spot temperature. A model is now needed to incorporate this hot spot temperature into the kinetics which represent how rapidly the solid explosive will gasify (explode).

2.5 The Combustion Model

Following the simplification used by Mader [25], a first order Arrhenius burn model was chosen to describe the chemical reaction (decomposition) rate of the solid material, expressed as

$$\frac{dW}{dt} = -z W \exp (-E^*/\bar{R}T^*) \quad (2.33)$$

In Equation (2.33) W denotes the mass fraction of unreacted explosive, z , frequency factor, E^* , activation energy, \bar{R} , universal gas constant, and T^* the characteristic burn temperature. The symbol $\frac{d}{dt}$ indicates a total derivative with respect to time.

At first the characteristic burn temperature was represented by the localized hot spot temperature, but Equation (2.33), utilizing values of z and E^*/\bar{R} (referred to as activation temperature) obtained from Nunziato [26], resulted in too slow of a reaction rate. Hayes [17] also came to this conclusion, based on experiments with a similar propellant, HNS. Since no decomposition times for hot spots are available for HMX, we therefore fit our model directly to Hayes data. By extracting several points from the curve in Figure 1.6, decomposition time was found to be a parabolic function of hot spot temperature, i.e.,

$$\log \tau = -0.6744703 \left[\frac{1000}{T_H} \right]^2 + 2.2482343 \left[\frac{1000}{T_H} \right] - 1.9132332 \quad (2.34)$$

where τ represents the decomposition time in microseconds. The data used by Hayes showed that a detonation occurred for a corresponding temperature of 619 K but did not for a corresponding lower temperature of 561 K, therefore 600 K was the temperature selected for the lower limit in applying expression (2.34) in the decomposition model.

To incorporate the decomposition time determined by Equation (2.34) into the combustion model, Equation (2.33) was integrated to define a new activation temperature corresponding to the predicted hot spot decomposition time. Therefore, by integrating Equation (2.33), the following expression is obtained

$$\frac{E^*}{R} = T_H \ln \left[\frac{\ln W_B}{-Z \tau} \right] \quad (2.35)$$

where W_B is the mass fraction remaining after chemical decomposition of the hot spot has occurred. Bearing in mind that this model is based on HNS rather than HMX, the activation temperature predicted from Equation (2.35) is bounded by the value given by Nunziato [26]. Subsequently, after the hot spot has decomposed, the characteristic burn temperature is defined by one of the following two values; (1) the bulk temperature or (2) the average of the bulk and hot spot temperature. These are then two distinct cases which are referred to as model CB1 and CB2, and are expressed below (along with the limits in which they apply) as

Model CB1

$$W_B \geq W \geq 0$$

$$T^* = T \quad (2.36)$$

Model CB2

$$W_B \geq W \geq 0$$

$$T^* = (T_H + T)/2.0 \quad \text{if } T_H > T \quad (2.37a)$$

$$T^* = T \quad \text{if } T_H \leq T \quad (2.37b)$$

Both models were used in the numerical solution technique. Based on the interpretation of the predicted results, model CB2 was eventually assumed better. A comparison of such results are presented in the next chapter along with the explanation of why model CB2 was chosen over CB1.

2.6 Review of the Key Assumptions

Before proceeding onto the description of the numerical solution technique a list of the key assumptions made in each portion of the solution technique is presented below.

Homogeneous Material

Solid Phase

- 1) the Gruneisen coefficient, $\Gamma \equiv -v \left(\frac{\partial P}{\partial e} \right)_v$, is constant.
- 2) the specific heat at constant volume, c_{VS} , is constant.

Gas Phase

- 1) the specific heat at constant volume, c_{vg} , is constant.

Porous Material

- 1) the Gruneisen coefficient, $\Gamma \equiv -v \left(\frac{\partial P}{\partial e} \right)_v$, is constant.
- 2) the specific heat at constant volume, c_{vs} , is constant.
- 3) the voids initially in the material are regarded as being massless.

Reactive Material

- 1) the Gruneisen coefficient, $\Gamma \equiv -v \left(\frac{\partial P}{\partial e} \right)_v$, is constant.
- 2) the specific heat at constant volume, c_{vs} , is constant.
- 3) the specific heat at constant volume, c_{vg} , is constant.
- 4) reaction does not initiate until the voids initially within the matrix of the material have completely collapsed.
- 5) the temperature of the gas phase equals the temperature of the solid phase which equals the temperature of the mechanical mixture
- 6) the pressure of the gas phase equals the pressure of the solid phase which equals the pressure of the mechanical mixture

Consequently, the subscripts of the parameters just equated will be dropped in the section which follow.

Table [2.2] presents a method of procedure for solving the flow equations which summarizes the logic, the manner in which these assumptions constrain the results, and the iteration pathways to assure convergence of all dependent variables.

TABLE 2.2

PROCEDURE FOR SOLVING THE FLOW EQUATIONS

- 1) Solve for the conservation of mass, Equation (2.2).
- 2) Solve for the conservation of momentum, Equation (2.3).
- 3) Solve for W , the mass fraction.
 - (i) If the pores initially contained in the matrix of the material have not collapsed, $W=1$ (no reaction).
 - (ii) If the initial pores have collapsed and the hot spot temperature, calculated from Equation (2.29), is less than 600 K, use Equation (2.33) to obtain a value for W .
 - (iii) If the initial pores have collapsed and the hot spot temperature is greater than 600 K, use Equations (2.33), (2.34), and (2.35) to determine a value for W .
- 4) Solve for the conservation of energy, Equation (2.4).
 - (i) Homogeneous Material
 - (1) Solid Phase - Solve for the remaining thermodynamic parameters, (P,T) , knowing that the total internal energy of the mechanical mixture is equal to the total internal energy of the solid, while utilizing the assumption that r and c_{vS} are constants.
 - (2) Gas Phase - Solve for the remaining thermodynamic parameters, (P,T) , knowing the total internal energy of the mechanical mixture equals the total internal energy of the gas, while making use of the assumption that c_{vG} is a constant.

- (ii) Porous Material - Solve for the remaining thermodynamic parameters, (P, v_s, T) . Utilizing the assumption that the initial voids are massless implies that the total internal energy of the mechanical mixture is equal to the total internal energy of the solid. Furthermore, an iterative technique must be used to equate the pressure predicted by the "P- α " law to the pressure of the solid by varying the specific volume of solid.
 - (iii) Reactive Material - Solve for the remaining thermodynamic parameters, (P, v_g, v_s, T) , by employing the assumption that the temperature of the gas and solid are equal to each other. In addition, the pressure of the gas and solid can be equated by utilizing an iterative method whereby the specific volume of the solid is varied.
- 5) Determine the hot spot temperature by employing Equations (2.29)-(2.32). However, the hot spot temperature is only calculated after complete pore collapse and before reaction begins.

2.7 Numerical Solution Technique

The equations presented in the previous sections of Chapter 2 completely define the hydrodynamics and thermodynamic state of a continuous, porous medium. A finite difference technique patterned after the WONDY code [27] was utilized to solve the system of equations. At the initial time, $t = 0$, the bed of porous propellant/explosive is discretized into J cells labeled from left to right as $j = 1, 2, 3, \dots, J$. The thermodynamic properties, pressure, temperature, internal energy, and specific volume, are assumed to be constant over the width of each cell. At the boundaries of the cells, the parameters, particle velocity, and spatial locations are defined. Figure 2.4 illustrates the location of the points of evaluation of the variables in time and spatial frames, where the steps in time are represented chronologically as $n-1$, n , $n+1$. Furthermore, Table [2.3] presents the sequence in which the fluid motion equations are solved, which are written in their finite difference approximation form. Steps (1-8), in Table [2.3], are performed to model stress wave propagation in a non reactive porous material while steps (1-4) and (5⁺-9⁺) outline the procedure in modeling the reaction of the propellant.

All variables are initially specified for each cell, located throughout the bed. Following, the second time step is obtained by first determining the velocity of the free boundary from the conservation of momentum equation, written as

$$u_{1/2}^{n+1/2} = u_{1/2}^{n-1/2} + (p_{bc} - p_1)/M_1 \quad (2.38)$$

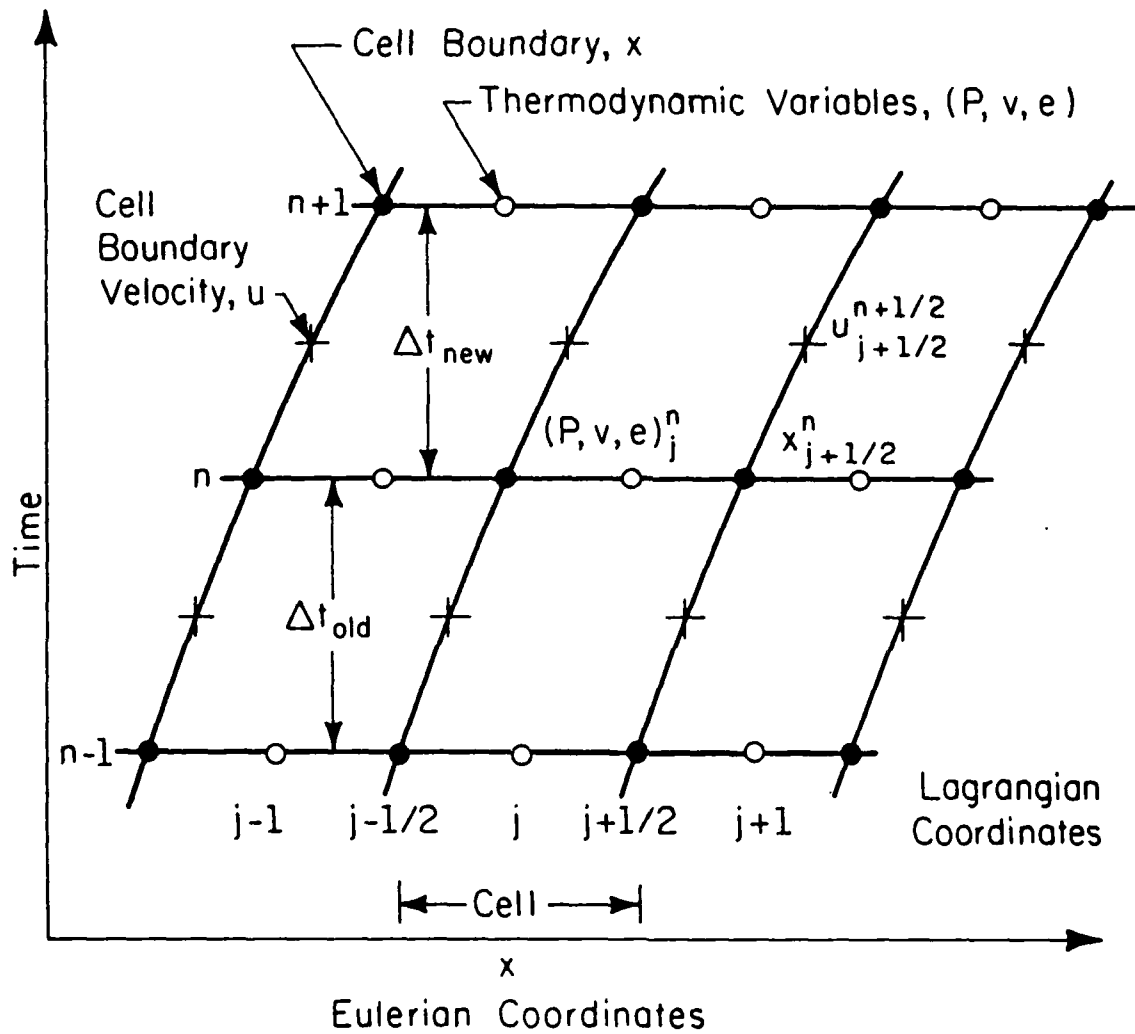


Figure 2.4 Representation of finite-difference cells indicating how the variables are defined with respect to the Lagrangian indices and Eulerian coordinate system. Figure taken from Reference [21].

Table 2.3
Lagrangian Finite-Difference Equations

$$1) \quad u_j^{n+1/2} = u_j^{n-1/2} + \frac{1}{4} (\Delta t^{n+1/2} + \Delta t^{n-1/2}) \frac{[(P+q)_{j-1}^n - (P+q)_j^n]}{(M_j + M_{j-1})}$$

where $\Delta t^{n+1/2} = t^{n+1} - t^n$

$$M_j = (h_j^{n+1/2} - h_j^{n-1/2}) / v_j^n = \text{constant}$$

$$2) \quad h_j^{n+1} = h_j^{n-1/2} + \Delta t^{n+1/2} u_j^{n+1/2}$$

$$3) \quad v_j^{n+1} = (h_j^{n+1/2} - h_j^{n-1/2}) / M_j$$

$$4) \quad (i) q_{j(1)}^{n+1} = 2.0 (ARV1)^2 (u_j^{n+1/2} - u_j^{n-1/2})^2 / v_j^{n+1}$$

where $q_{j(1)}^{n+1} = 0$ if $u_j^{n+1/2} < u_j^{n-1/2}$

$$(ii) q_{j(2)}^{n+1} = ARV2 (h_j^{n+1/2} - h_j^{n-1/2}) C_j^n (v_j^n - v_j^{n+1}) / \Delta t^{n+1/2}$$

where $q_{j(2)}^{n+1} = 0$ if $v_j^{n+1} > v_j^n$

$$(iii) q_j^{n+1} = q_{j(1)}^{n+1} + q_{j(2)}^{n+1}$$

$$5) \quad p_j^{n+1} = f(\alpha_j^{n+1}) \text{ determined by Equations (2.16-2.20) in Section (2.3)}$$

where $\alpha_j^{n+1} = v_j^{n+1} / (v_s)_j^{n+1}$

6) T_j^{n+1} determined from $e_j^{n+1} = (e_s)_j^{n+1}$

where $e_j^{n+1} = e_j^n + [(P_j + q_j)^{n+1} + (P_j + q_j)^n] \frac{\Delta v}{v} + \Delta Q$

$$(e_s)_j^{n+1} = C_{vs}(T_j^{n+1} - T_0) + J[(v_s)_j^{n+1}] - r C_{vs} T_0 \ln \left[\frac{v_{so}}{(v_s)_j^{n+1}} \right]$$

$$\frac{\Delta v}{v} = \frac{2v_j^n v_j^{n+1} (v_j^n - v_j^{n+1})}{(v_j^n + v_j^{n+1})^2}$$

$\Delta Q = 0$ no reaction

7) $P_j^{n+1} = (P_s)_j^{n+1} = \{ r C_{vs} (T_j^{n+1} - T_0) (v_s)_j^{n+1} + \frac{\partial}{\partial v_s} [J((v_s)_j^{n+1})] \} / [(v_s)_j^{n+1}]^2 + P_0$

8) $C_j^{n+1} = \{ C_s^* \}^{1/2}$

$$C_s^* = (v_s)_j^{n+1} \left\{ \frac{\partial}{\partial v_s} [(P_s)_j^{n+1}] \right\}$$

partial derivative evaluated
at constant temperature

5)* (i) $w_j^{n+1} = w_j^n - 1/2 w_j^n (\Delta t^n + 1/2 + \Delta t^n - 1/2) z \exp \left[\frac{-\hat{T}}{(T_H)_j^*} \right]$ if $1 \geq w_j^{n+1} \geq w_B$

where $-\hat{T} = \text{Equation (2.35)} \geq -\frac{E^*}{R}$

$(T_H)_j^*$ is determined from Equation (2.29)

(ii) $w_j^{n+1} = w_j^n - 1/2 w_j^n (\Delta t^n + 1/2 + \Delta t^n - 1/2) z \exp \left[-\frac{E^*}{R T_j^*} \right]$ if $w_B \geq w_j^{n+1} \geq 0$

where C81 $T_j^* = T_j^n$

* see explanation on page 45

$$\text{CB2 } T_j^* = 1/2 [(T_H)_j + T_j^n] \quad \text{if } T_j^n < (T_H)_j$$

$$T_j^* = T_j^n \quad \text{if } T_j^n \geq (T_H)_j$$

$$6)^+ \quad T_j^{n+1} \text{ determined from } e_j^{n+1} = w_j^{n+1} (e_s)_j^{n+1} + (1-w_j^{n+1}) (e_g)_j^{n+1}$$

$$\text{where } (e_g)_j^{n+1} = c_{vg} (T_j^{n+1} - T_o)$$

$$\Delta Q = (w_j^n - w_j^{n+1}) H_{DET}$$

$$7)^+ \quad p_j^{n+1} = R T_j^{n+1} [1 + \beta / (v_g)_j^{n+1}] / (v_g)_j^{n+1}$$

$$\text{where } (v_g)_j^{n+1} = \frac{v_j^{n+1} - w_j^{n+1} (v_s)_j^{n+1}}{(1-w_j^{n+1})}$$

$$8)^+ \quad p_j^{n+1} = (p_s)_j^{n+1}$$

$$9)^+ \quad c_j^{n+1} = \frac{v_j^{n+1}}{\left\{ \frac{(v_s)_j^{n+1}}{\alpha_j^{n+1} c_s^*} + \frac{(v_g)_j^{n+1} (\alpha_j^{n+1} - 1)}{\alpha_j^{n+1} c_g^*} \right\}}^{1/2}$$

$$\text{where } c_g^* = 3 \hat{R} T_j^{n+1} + 6 \beta \hat{R} T_j^{n+1} / (v_g)_j^{n+1}$$

* The localized hot spot temperature is determined after complete compaction and the values used for specific volume correspond to the pressure strength of the shock that initiated compaction.

with q , the artificial viscosity which will be described later, being set equal to zero. In Equation (2.38), P_{bc} is the pressure at the free boundary condition described by Equations (2.1a and b). Notice, as shown in Table [2.3], the conservation of mass is expressed in two steps (2 and 3), thus enabling a solution for the location of the Lagrangian spatial coordinates, for each step in time, explicitly. Steps (5-7) and (6⁺-8⁺) have to be solved implicitly, therefore an iterative technique must be utilized for their solution, while the remaining steps are all solved explicitly.

To insure stability of the solution over time, an expression for the time step was taken from Reference [27] and is written here as

$$\Delta t_j^{n+3/2} = \frac{K_{t1} \Delta h_j^{n+1}}{\text{VARB} + \{(\text{VARB})^2 + (C_j^{n+1})^2\}^{1/2}} \quad (2.39a)$$

$$\text{and } \text{VARB} = B_2 C_j^{n+1} + 2 B_1^2 \left(-\frac{1}{v} \frac{\partial v}{\partial t}\right) \Delta h_j^{n+1} \quad (2.39b)$$

where K , B_1 and B_2 are constants while

$$\left(-\frac{1}{v} \frac{\partial v}{\partial t}\right) = \frac{2 (v_j^n - v_j^{n+1})}{(v_j^n + v_j^{n+1}) \Delta t^{n+1/2}} \quad (2.39c)$$

Furthermore, the time step is never assigned a value greater than five nanoseconds, which is to insure stable solution during decomposition. Also to insure stability of solution, q , the artificial viscosity term was introduced to conservation of momentum and energy equations of the mechanical mixture.

Artificial viscosity is employed in the numerical finite-difference technique to prevent an infinite slope of the pressure wave, $\frac{dP}{dx}$, which would asymptotically occur when a shock wave is formed. Essentially, by utilizing

artificial viscosity, the shock wave is spread over a finite number of Lagrangian cells. A time-intensive effort was required before a proper expression for artificial viscosity was found which gave reproducible results. The expression for artificial viscosity, presented in Table [2.3] as step (4), is a combination of a quadratic equation, taken from Reference [28] (which essentially spreads the shock wave) and a linear equation, taken from WONDY [27] and subsequently modified (which dampens the oscillation that might occur throughout the bed).

Sound speed is introduced only to provide mathematical closure for the artificial viscosity expression and Equation (2.39). Steps (8 and 9⁺) in Table [2.3] represent the expressions which are assumed to sufficiently describe the sound speed in a porous and two phase material, respectively.

The numerical solution technique described above was incorporated into a code given in Appendix C.

CHAPTER 3

NUMERICAL RESULTS

This chapter will present several cases which capture a five-part scenerio of Deflagration to Shock to Detonation, as illustrated in Figure 1.10. All the cases that will be presented numerically model a ten centimeter long bed of HMX, either initially homogeneous or initially porous. The bed was discretized into two hundred Lagrangian finite-difference cells, thus corresponding to an initial grid spacing of five tenths of a millimeter, ($\Delta x = 0.05$ cm). Earlier studies, by Coyne, Butler and Krier [10], employed the same initial grid spacing for modeling stress wave formation and propagation in an explosive medium. In addition, the values of the coefficients for artificial viscosity are $ARV1=2.0$ and $ARV2=0.1$, which are used for all cases shown in the sections to follow (unless explicitly stated otherwise). Also, as stated in Chapter 2, the CB2 combustion model is utilized unless explicitly stated otherwise. All propellant properties are listed in Appendix A.

The following sections will discuss and present computed results for shock initiation to detonation for both homogenous and porous materials. Validation of the model, based on several typical cases of "ramp" wave initiation to detonation in a porous material, is also included. In addition, a comparison of the two combustion models (CB1 and CB2), is presented, including calculations for different parameters.

3.1 Shock Initiation of Detonation

The first calculations considered a purely homogeneous bed of HMX. Since the bed is purely homogeneous (no voids exist), the characteristic burn temperature is represented simply as the temperature of the bed. Also different from the general void containing cases, analysis for a homogeneous material requires an artificial viscosity formulation documented in Reference [27]. A shock strength of 10 GPa, i.e., $P^*=10$ GPa and $t^*=0.02$ μ sec, was used to initiate the stress waves that produce detonative reactions in the bed. A different criteria was needed to initiate reaction here, since the temperature produced by shocking the homogeneous medium was not sufficient in initiating reaction utilizing the explosion model. If a temperature greater than 450 K is reached, a value of 0.85 is assigned for the mass fraction, thus artificially inducing reaction. Subsequently, a detonation was produced in the bed, as clearly shown in Figure 3.1, which exhibits the pressure profile of the detonation wave as it propagates through the bed. Listed in Table [3.1], are the CJ parameters predicted by the computer code (presented in Appendix C) along with the CJ parameters predicted by TIGER [23]. Although the CJ parameters predicted by code do not agree exactly with those predicted by TIGER, the results are acceptable.

Problems arose, however, when trying to produce a shock wave in a porous material. Figure 3.2, taken from Reference [21], shows the velocity magnitude of the free boundary as a function of time for a homogeneous case ($\alpha_0 = 1$), and two porous cases ($\alpha_0 = 1.2$, and $\alpha_0 = 1.4$), produced by a "ramp" wave with $P^* = 3$ GPa and $t^* = 40$ μ sec. One can clearly see a "jump" in the velocity magnitude for both porous cases contrasting with the homogeneous case which shows a smooth transition to a steady value. Coyne, Butler and Krier [10]

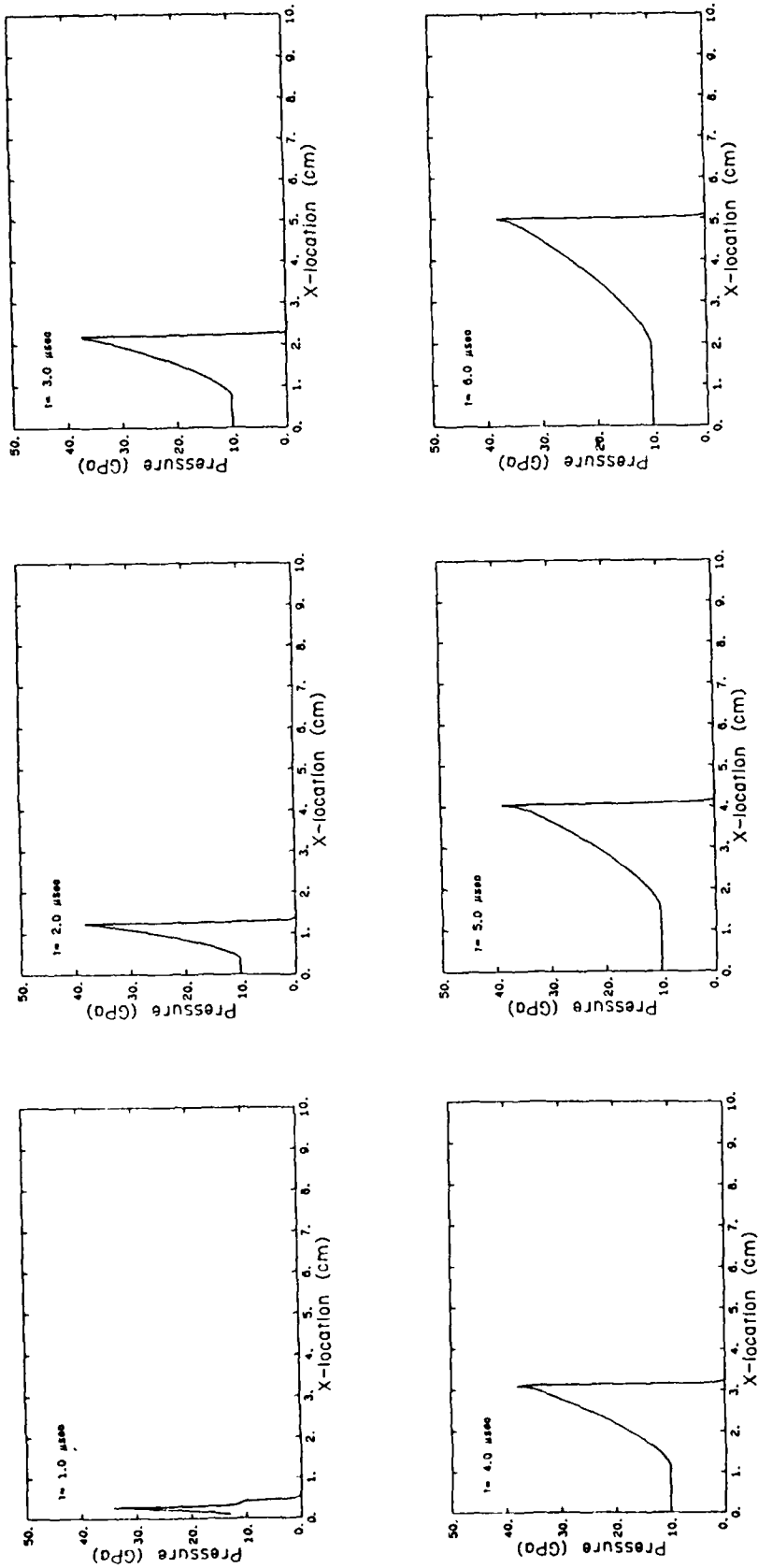


Figure 3.1 Predicted pressure distribution history for a homogeneous bed of HMX
 $(\alpha_0 = 1, p^* = 10 \text{ GPa}, t^* = 0.02 \text{ } \mu\text{sec})$.

TABLE 3.1

PREDICTED CJ PARAMETERS FOR HOMOGENEOUS HMX

	P_{CJ} (GPa)	T_{CJ} (K)	v_{CJ} (cc/g)	D (mm/ μ)
TIGER [23]	35.99	3714	0.4073	9.154
Our Code	38.90	3953	0.4041	9.39

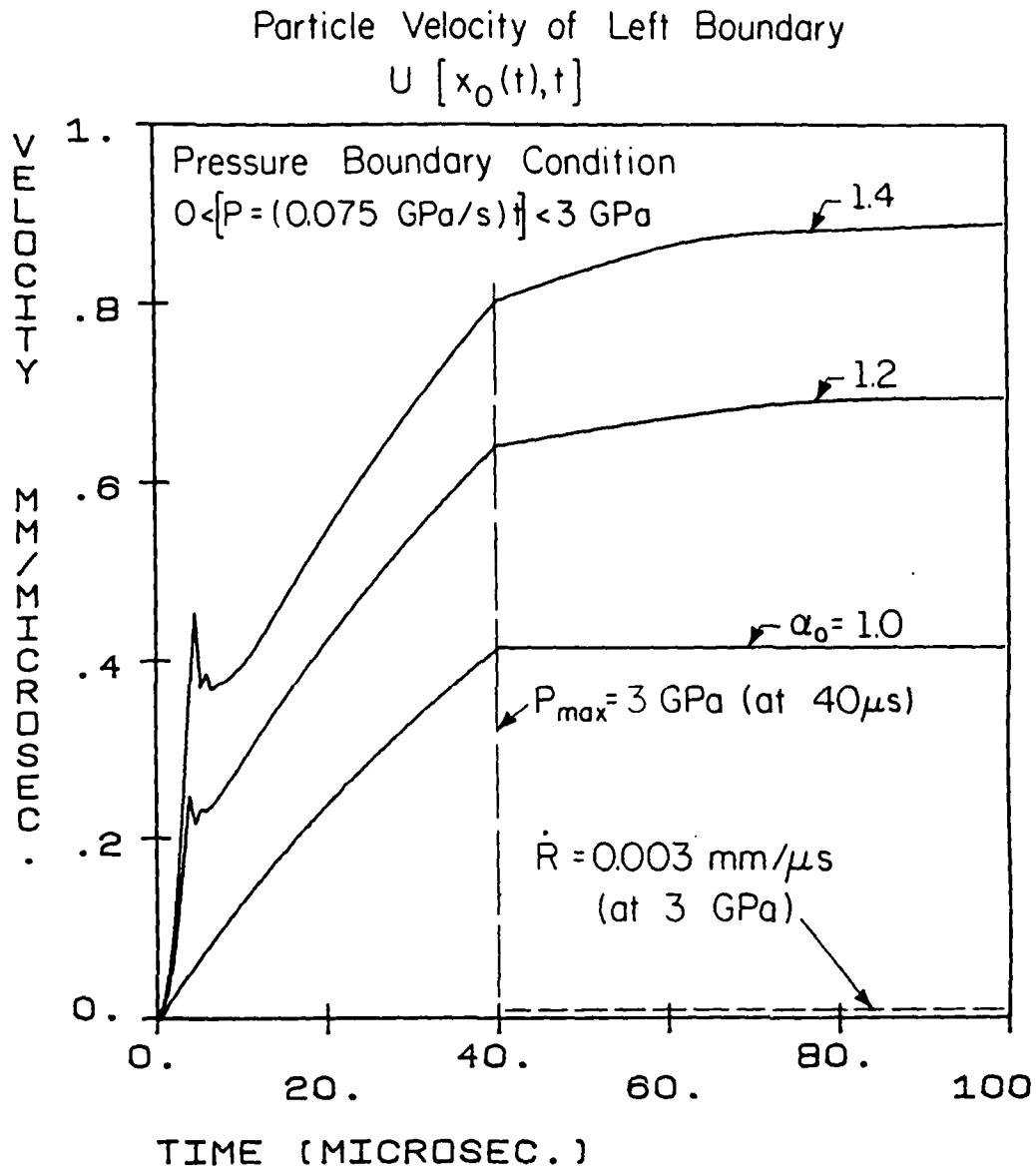


Figure 3.2 Velocity of the left boundary as a function of time from the finite difference initial porosities compared with the velocity of a one-dimensional regressive burn, $\dot{r} = 0.001 \text{ mm}/\mu\text{sec}$ P (GPa). Figure taken from Ref. [21].

attributed the jumps in velocity magnitude to be caused by the pore collapse model and not by numerical inaccuracies. Therefore to introduce a shock wave into a porous explosive, a specific "ramp" wave is required, while considering the propellant bed to be inert until the compression wave has achieved the desired strength. A condition, $P^* = 2$ GPa and $t^* = 10$ μ sec, was used to create the shock wave in a porous explosive case, $\alpha_0 = 1.5322$. Figure 3.3 illustrates the pressure profiles leading to a steady detonation. The predicted steady CJ values for pressure, specific volume and temperature are 19.49 GPa, 0.5544 cc/g and 4597 K with a corresponding detonation velocity of 7.082 mm/ μ sec, values which are proper for HMX with a density of $\rho_0 = 1.24$ g/cc, reduced from the crystalline density of $\rho_0 = 1.90$ g/cc when $\alpha_0 = 1$.

3.2 Validation of the Model

As mentioned in Chapter 1, accumulating accurate experimental data for shock initiating a porous explosive is difficult. However, J. J. Dick [11] was successful in obtaining "Pop plot" data through extensive runs and statistical analysis for samples of porous HMX, namely, $\alpha_0 = 1.5322$. Several calculations were made here assuming a porosity identical to the one used in Reference [11] by J. J. Dick, varying the shock strength in order to produce a theoretical "Pop plot". For comparison, Dick's results are displayed in Figure 3.4 as solid lines, along with the computed results (shown by the dashed line). It is clear from Figure 3.4, that although the calculated run-up to detonation distances do not fall in the uncertain range of Dick's experimental results, the model does predict an almost identical slope. The quantitative disagreement could stem from utilizing calculated decomposition times for the hot spots based on experimental data obtained for a similar yet

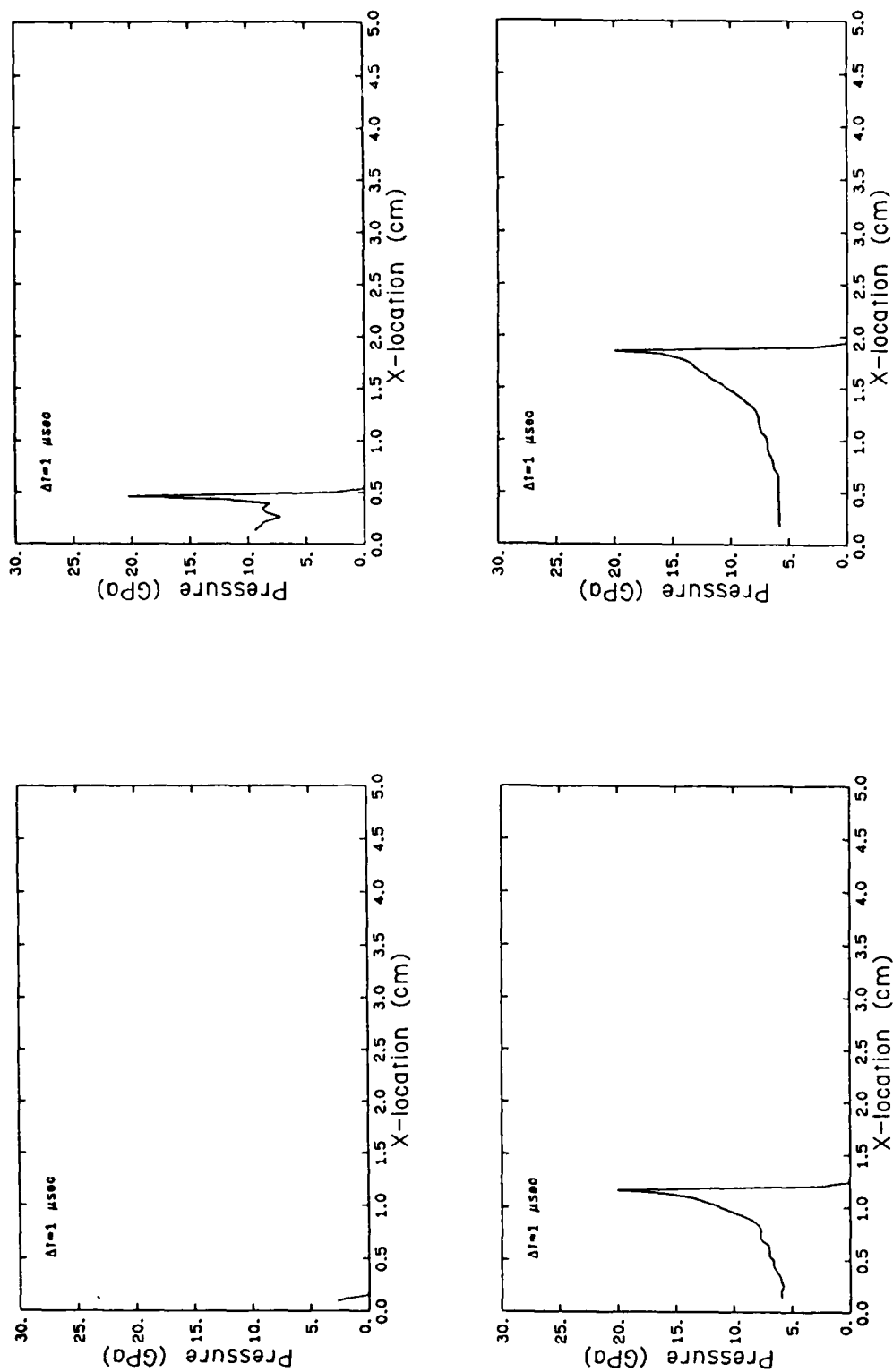


Figure 3.3 Predicted pressure distribution history for a shock initiated porous bed of HMX displayed at intervals of one microsecond. ($\alpha_0 = 1.5322$, $p^* = 3 \text{ GPa}$)

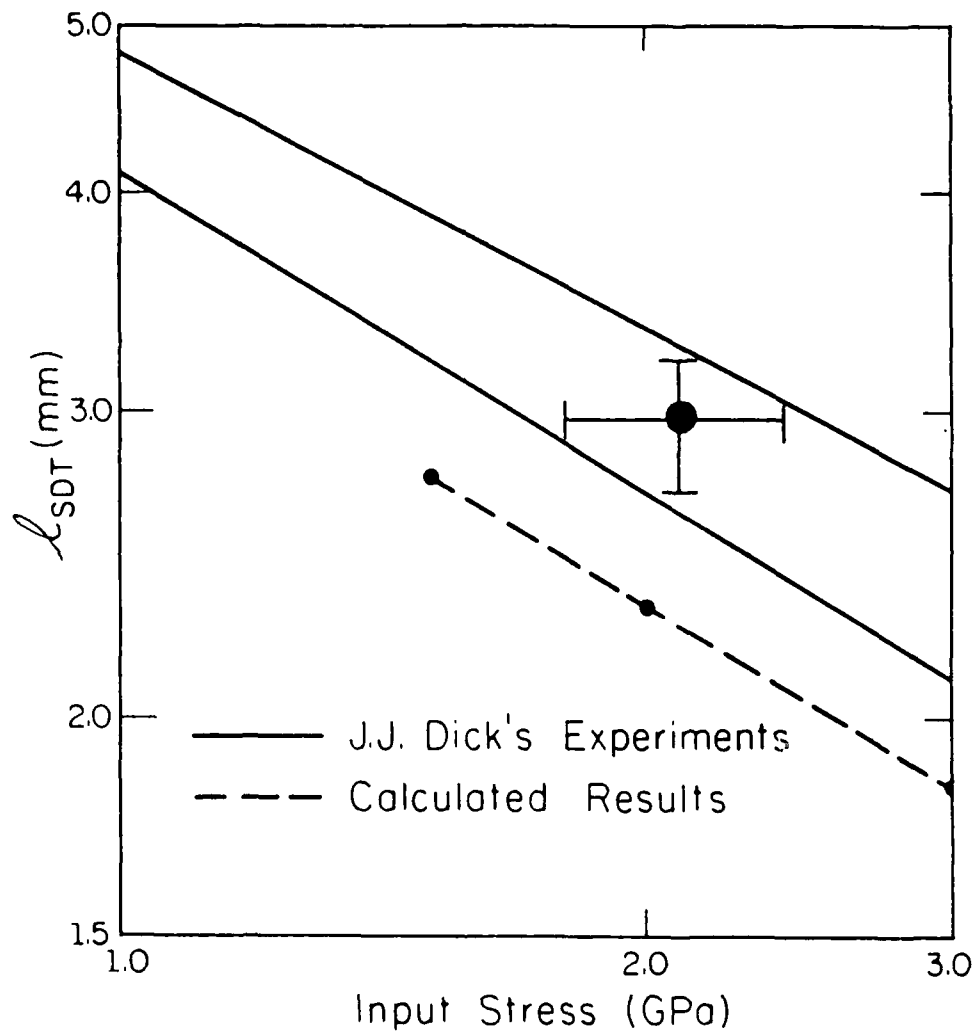


Figure 3.4 A comparison of numerically predicted and experimentally observed [11] run-up distance versus input pressure for a porous bed of HMX ($\alpha_0=1.5322$)

different propellant, HNS. Furthermore, Hayes' hot spot model was based on experimental results for porosities ranging from $1.0875 < \alpha_0 < 1.2518$, where Dick's experiment and the calculations were conducted for a higher porosity, $\alpha_0 = 1.5322$. Finally, a true shock can never be precisely modeled since the stress wave must be spread over several grid elements, a discrepancy in the predicted results. Nevertheless, within the limitations of the model, the results predicted are exceptionally good.

3.3 Typical Cases

Several cases were chosen with various maximum input stresses, characteristic rise times and porosities to test the model trends. The first case considered an initial porosity of $\alpha_0 = 1.1176$, initiated by a "ramp" wave having a maximum input pressure of $P^* = 2$ GPa and characteristic rise time of $t^* = 10$ μ sec. Figures 3.5-3.9 illustrate the distribution history of several key parameters, namely P , α , $(1-W)$, T_H , and T . For this particular case, six specific segments in time were chosen for illustration purposes. The first time shown in all the five separate figures is 10 μ sec. By viewing Figure 3.5, one can see that the compression wave has propagated into the bed to a distance of 1.5 cm. Notice even though the left boundary has reached the maximum input stress, shown approximately at a location of 2 mm into the bed, the shock front has not fully developed. Figure 3.6 illustrates the closure of the voids as a result of the compression wave, or in other words, displays the formation of the solid plug.

One can see from Figure 3.7, at 10 μ sec, that the reaction has not commenced. As time progresses the compression waves coalesce, strengthening the shock front which in turn deposits larger amounts of (irreversible) energy

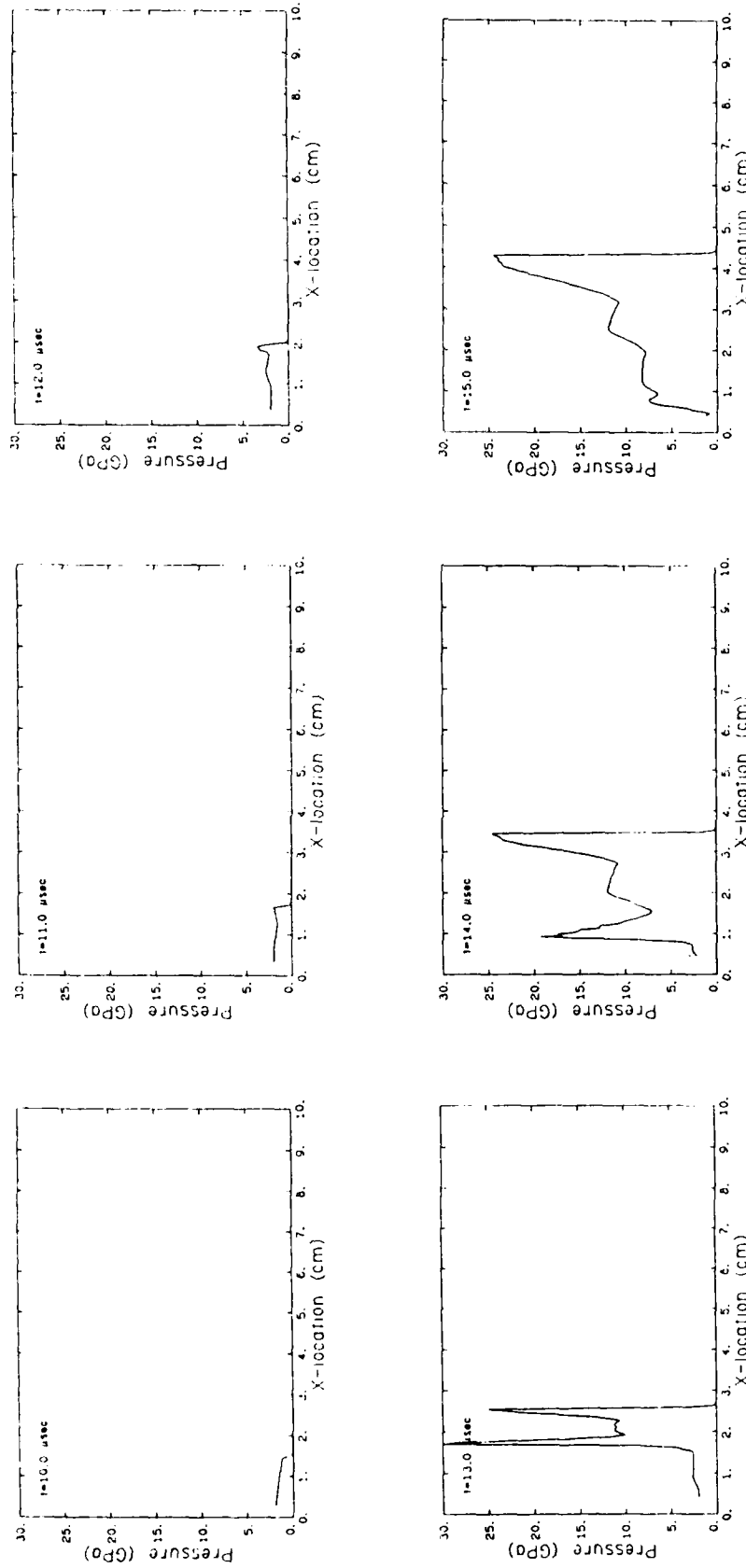


Figure 3.5 Predicted pressure distribution history for a porous bed of HMX
 ($\alpha_0 = 1.1176$, $p^* = 2$ GPa, $t^* = 10$ μ sec).

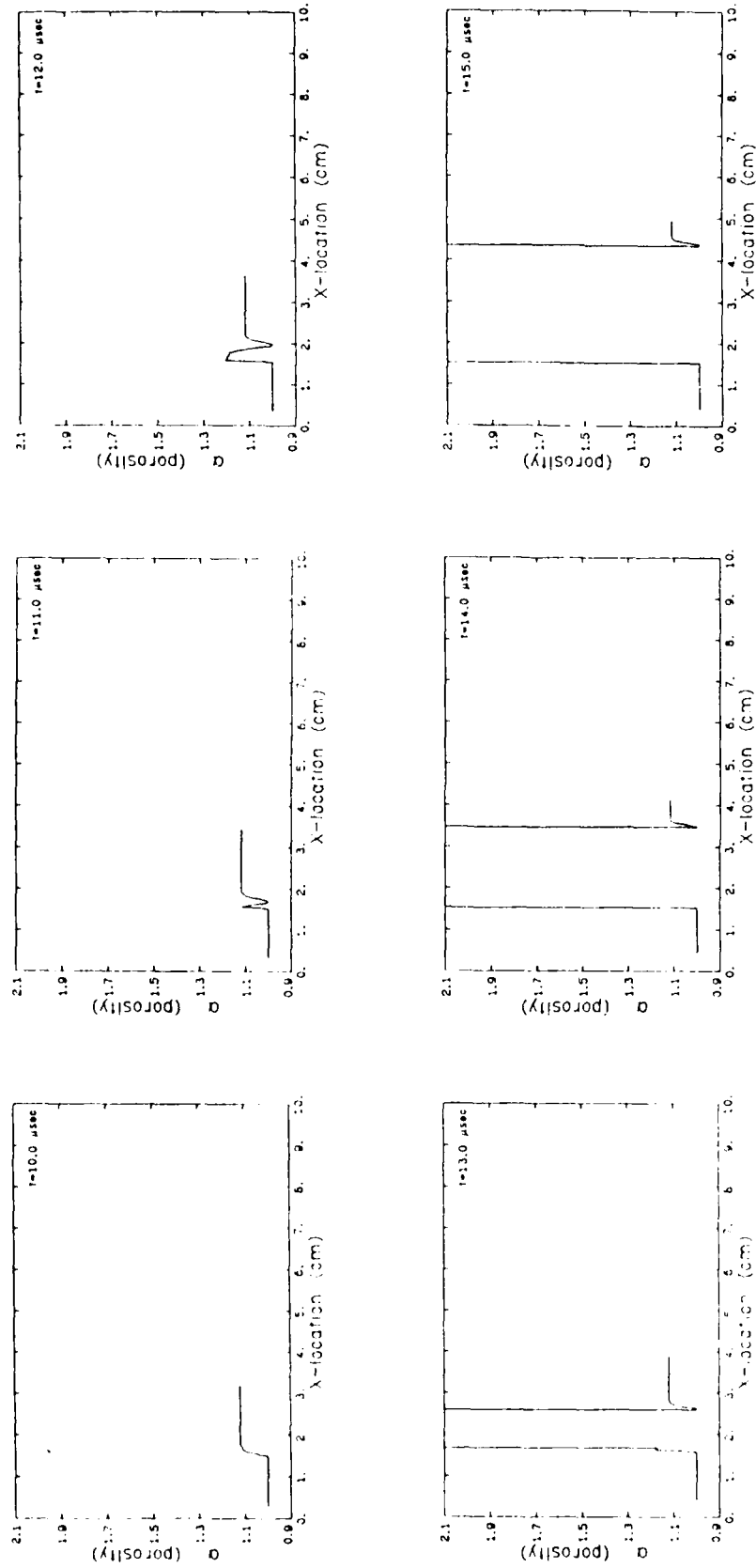


Figure 3.6 Predicted porosity distribution history for a porous bed of HMX
 ($\alpha_0 = 1.1176$, $P^* = 2$ GPa, $t^* = 10 \mu\text{sec}$).

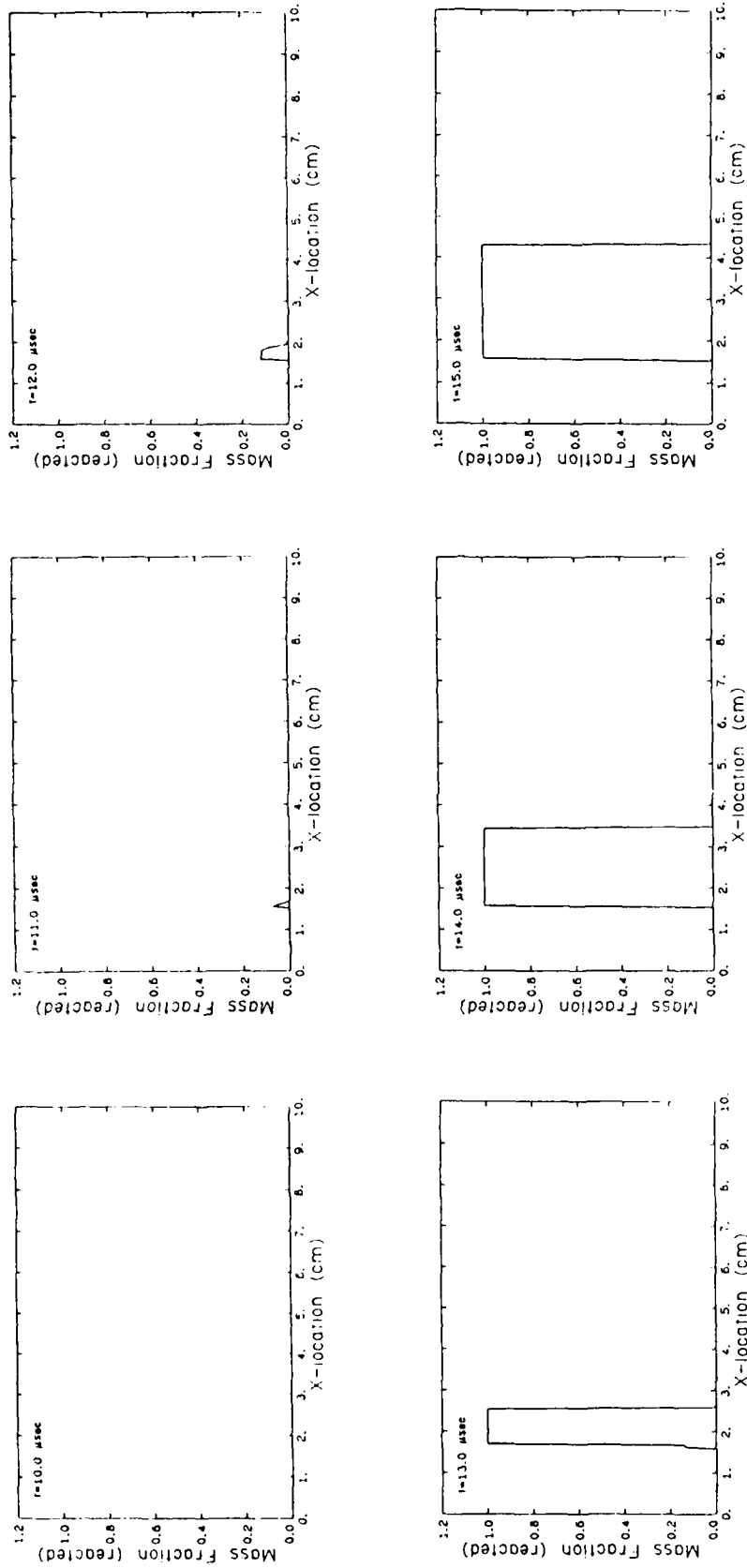


Figure 3.7 Predicted unreacted mass fraction distribution history for a porous bed of HMX
 $(\alpha_0 = 1.1176, P^* = 2 \text{ GPa}, t^* = 10 \mu\text{sec})$.

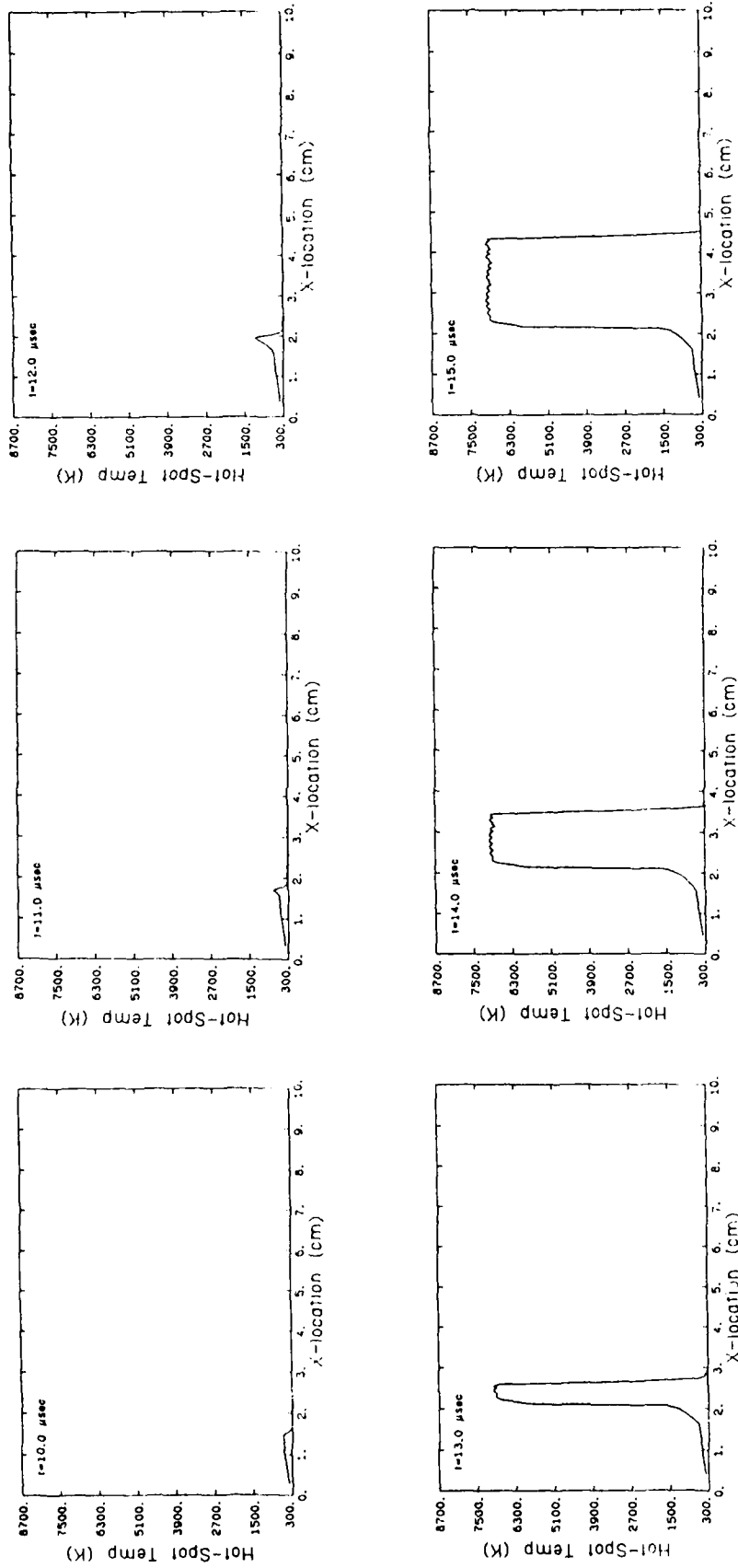


Figure 3.8 Predicted hot spot temperature distribution history for a porous bed of HMX
 $(\alpha_0 = 1.1176, p^* = 2 \text{ GPa}, t^* = 10 \mu\text{sec})$.

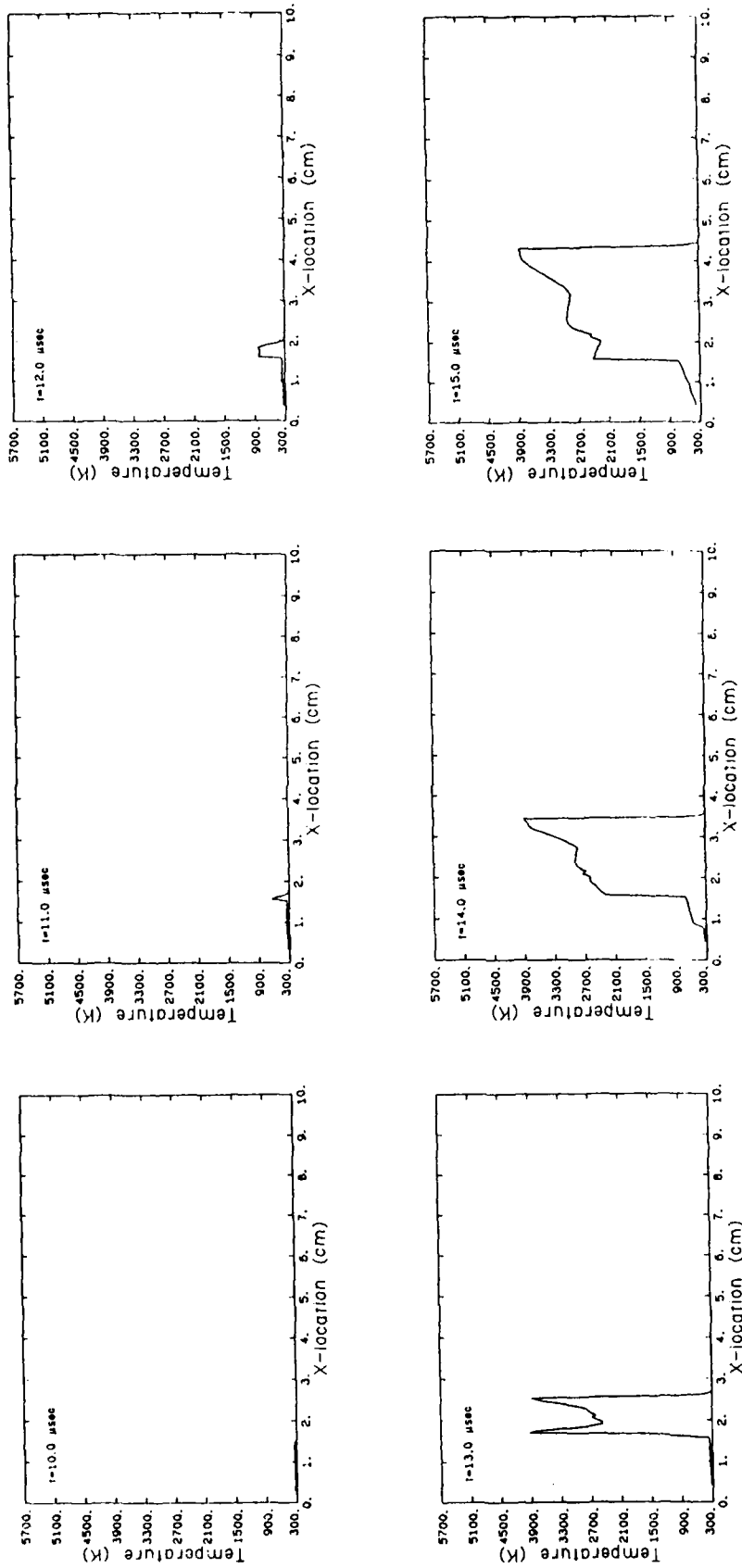


Figure 3.9 Predicted temperature distribution history for a porous bed of HMX
 ($\alpha_0 = 1.1176$, $p^* = 2$ GPa, $t^* = 10 \mu\text{sec}$).

into the voids prompting an increase in the hot spot temperature. Figure 3.8 exhibits this steady increase by the positive slope of the hot spot temperature profile. Furthermore, one can see that the hot spot temperature is much greater than the material temperature of the bed, the latter depicted in Figure 3.9.

As time progresses to 11 μsec , Figure 3.7 shows reaction has begun. This occurrence can also be viewed by an increase in porosity (α), as displayed in Figure 3.6 at that instant. Induced by the initiation of propellant decomposition an increase in strength of the compression front occurs, as seen in Figure 3.5. The effect of the strengthened compression front is a rise in the hot spot temperatures as illustrated in Figure 3.8. Also because of the reaction, there is a predicted increase in the bulk temperature, exhibited in Figure 3.9 at $t = 11 \mu\text{sec}$.

At the third time presented, 12 μsec , the degree of reaction has increased, again shown in Figure 3.7 and in Figure 3.6. With the increase in the degree of reaction, the chemical energy further contributes to strengthen the compression front, as illustrated in Figure 3.5. In turn, a stronger shock strength prompts a higher hot spot temperature, depicted in Figure 3.8, and the additional chemical energy also stimulates a rise in the material temperature, as shown in Figure 3.9.

At 13 μsec , the decomposition of the propellant is complete in a small region of the bed near $x = 2 \text{ cm}$, as pictured in Figure 3.7. The porosity distribution, displayed in Figure 3.6 (at 13 μsec), shows compression ahead of the decomposition region. The effect of all of this is a right moving detonation wave and a left or rearward moving retonation wave, as illustrated in Figure 3.5. One may notice that the retonation wave has a higher peak

pressure than the detonation wave, since it must travel through a highly compressed material, whereas the detonation wave must propagate through a porous material. The substantial rise in the pressure front subsequently causes an even higher hot spot temperature, due to the overabundant irreversible energy being deposited at the void sites, as shown in Figure 3.8.

At the fifth time shown, $t = 14 \mu\text{sec}$, the region of complete decomposition is greatly enlarged, as illustrated in both Figure 3.6 and 3.7. The chemical energy being released in turn prompts the propagation of the detonation wave further into the propellant bed, as seen in Figure 3.5. However, the detonative reaction has ceased propagating, causing a steady decrease in the left moving wave. One would have expected that the detonation wave would have propagated all the way to the left boundary. However, the Arrhenius kinetics failed to sustain the detonation wave, just as the Arrhenius kinetics failed to initiate reaction in homogeneous material shocked to 10 GPa. Hayes [17] came to the conclusion, for a porous material, that scissoring of molecular chemical bonds induced the experimentally observed decomposition times. It is therefore postulated that a shock of substantial strength may also change the molecular structure of a voidless propellant enhancing reaction. Also at time, $t = 14 \mu\text{sec}$, Figure 3.8 shows that the detonation wave produces a steady hot spot temperature. The oscillations seen in the hot spot temperature are a result of numerical integration inaccuracies.

At the final time shown, $t = 15 \mu\text{sec}$, Figure 3.5 illustrates the steady detonation wave continuing to propagate even further into the bed at a predicted CJ pressure of 24.99 GPa and a corresponding CJ temperature of 3923 K, shown in Figure 3.9.

In addition to the figures just presented, a locus of stress and reaction fronts are shown in Figure 3.10. The dashed line depicts stress wave propagation into the bed, initiating the detonation $t = 12.41 \mu\text{sec}$, at $x = 2.05 \text{ cm}$. The solid lines represent the locus of the right and left traveling detonation fronts. Figure 3.10 also shows the termination point of the detonation wave. An apparent change in velocity may be seen in the left traveling wave at the termination point. The slope of the solid lines correspond to a detonation and detonation velocity of $D = 8.757 \text{ mm}/\mu\text{sec}$ and $R = 9.135 \text{ mm}/\mu\text{sec}$.

A second case is now presented for a material with a higher initial porosity, namely $\alpha_0 = 1.1875$, and with an increased strength "ramp" wave $P^* = 4 \text{ GPa}$ and $t^* = 10 \mu\text{sec}$. Figures 3.11-3.15 depict the pressure, porosity, mass fraction reacted, hot spot temperature, and bulk temperature distribution for fixed time segments. One can see from Figure 3.11 that the detonation occurs just behind the compression front and in the following time the stress front is overtaken by the detonation wave.

Different from the previous case presented, no detonation takes place. However, a left moving compression can be seen in Figure 3.11. If a chemical change does occur when a homogeneous material is strongly shocked (enhancing the sensitivity to reaction), as postulated earlier, a detonation would have been caused. Also illustrated in Figure 3.11 is the steady state detonation wave having a CJ pressure of 24.39 GPa and a corresponding CJ temperature of 4173 K depicted in Figure 3.15. The physical plane, shown in Figure 3.16, illustrates a detonation velocity, $D = 8.255 \text{ mm}/\mu\text{sec}$, but no detonation wave. The detonation occurs at a run-up distance of $x = 4.83 \text{ mm}$ at $t = 4.96 \mu\text{sec}$.

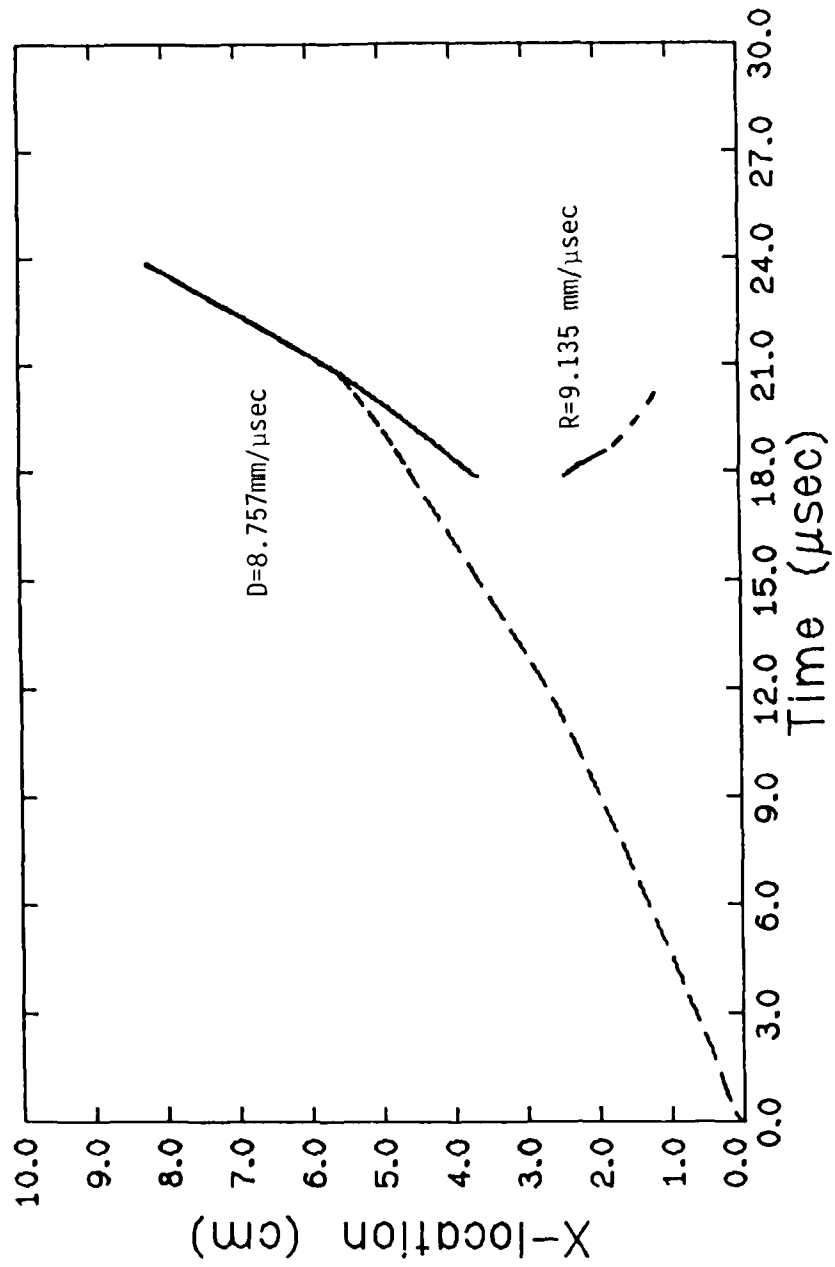


Figure 3.10 Physical plane, showing locus of compression, detonation and detonation fronts ($\alpha_0=1.1176$, $p^*=2\text{ GPa}$, $t^*=10\text{ }\mu\text{sec}$).

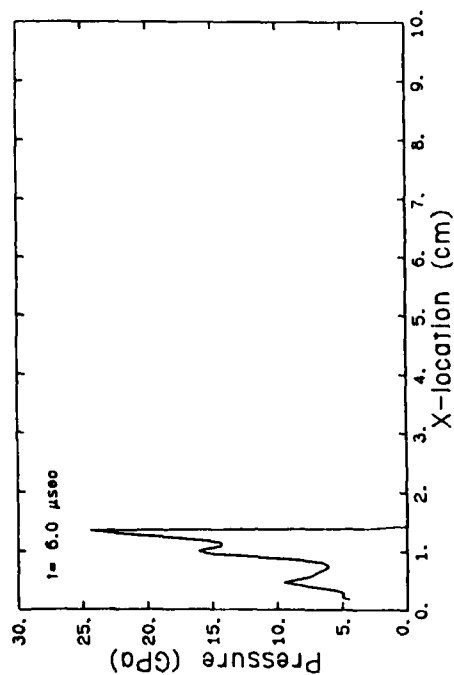
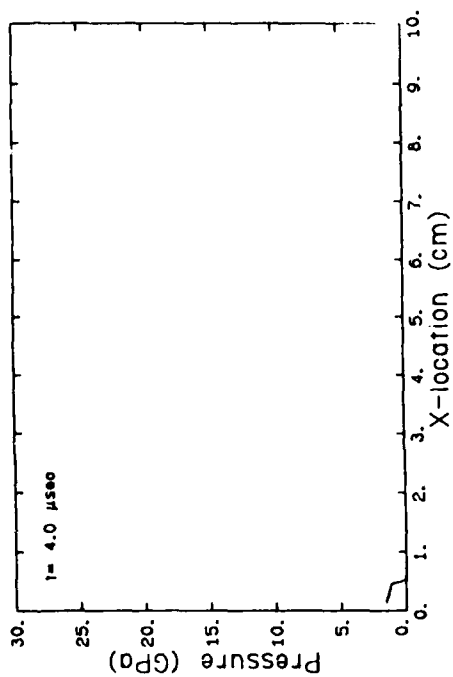
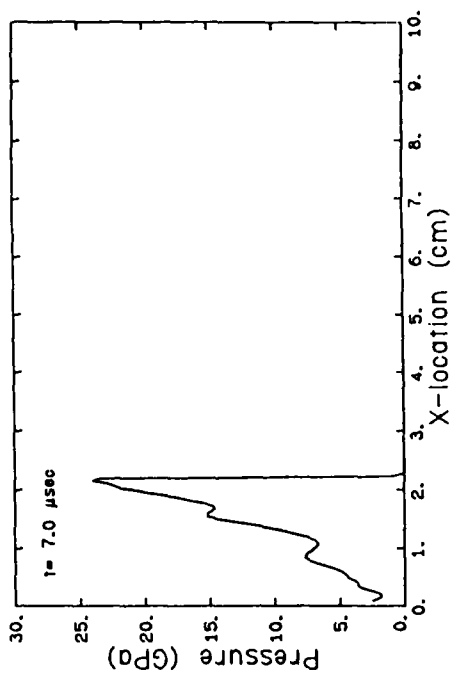
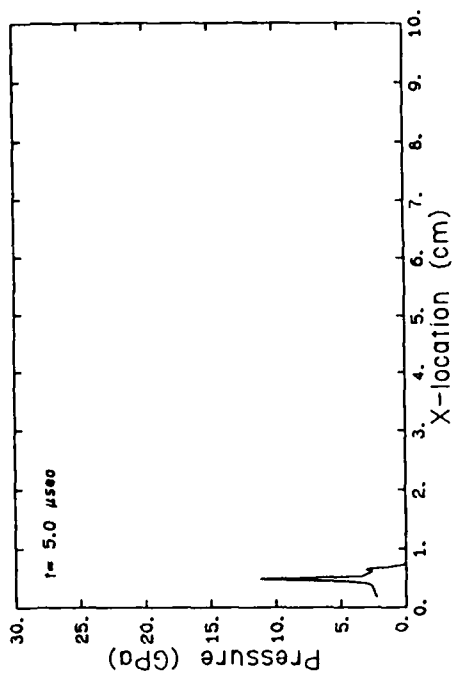


Figure 3.11 Predicted pressure distribution history for a porous bed of HMX
 $(\alpha_0 = 1.1875, p^* = 4 \text{ GPa}, t^* = 10 \mu\text{sec})$.

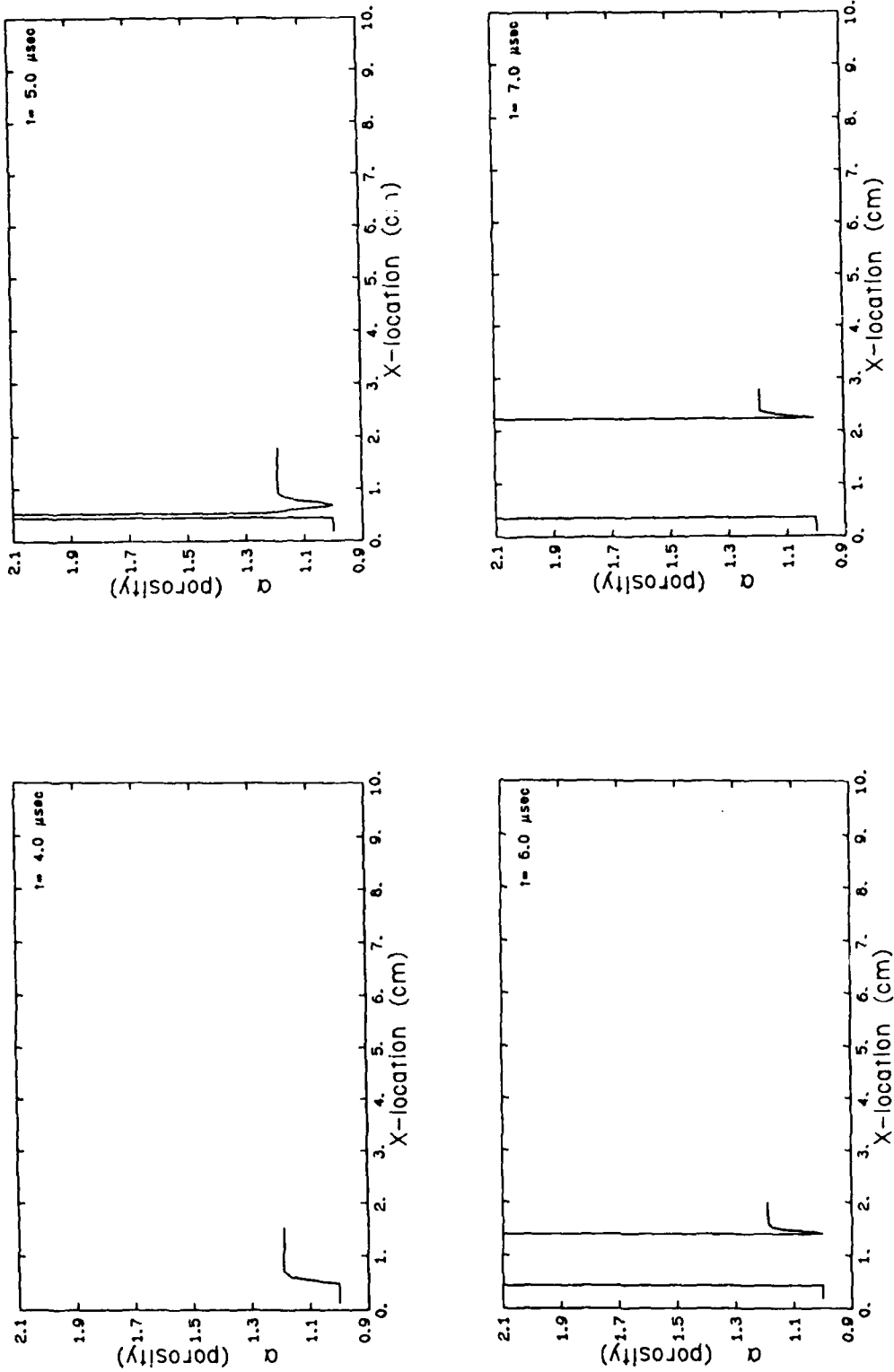


Figure 3.12 Predicted porosity distribution history for a porous bed of HMX
 $(\alpha_0 = 1.1875, p^* = 4 \text{ GPa}, t^* = 10 \mu\text{sec})$.

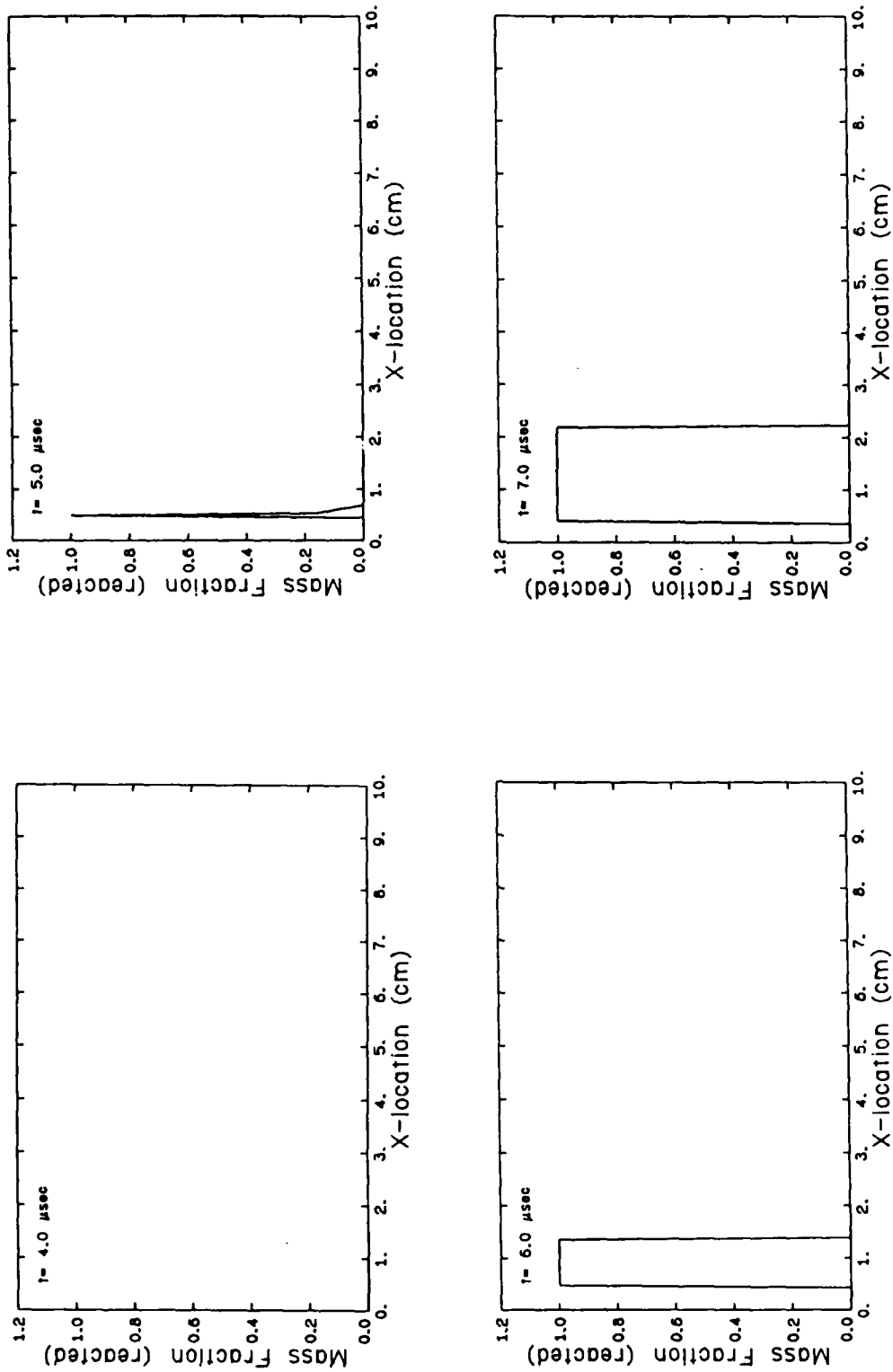


Figure 3.13 Predicted unreacted mass fraction distribution history for a porous bed of HMX ($\alpha_0 = 1.1875$, $P^* = 4$ GPa, $t^* = 10 \mu\text{sec}$).

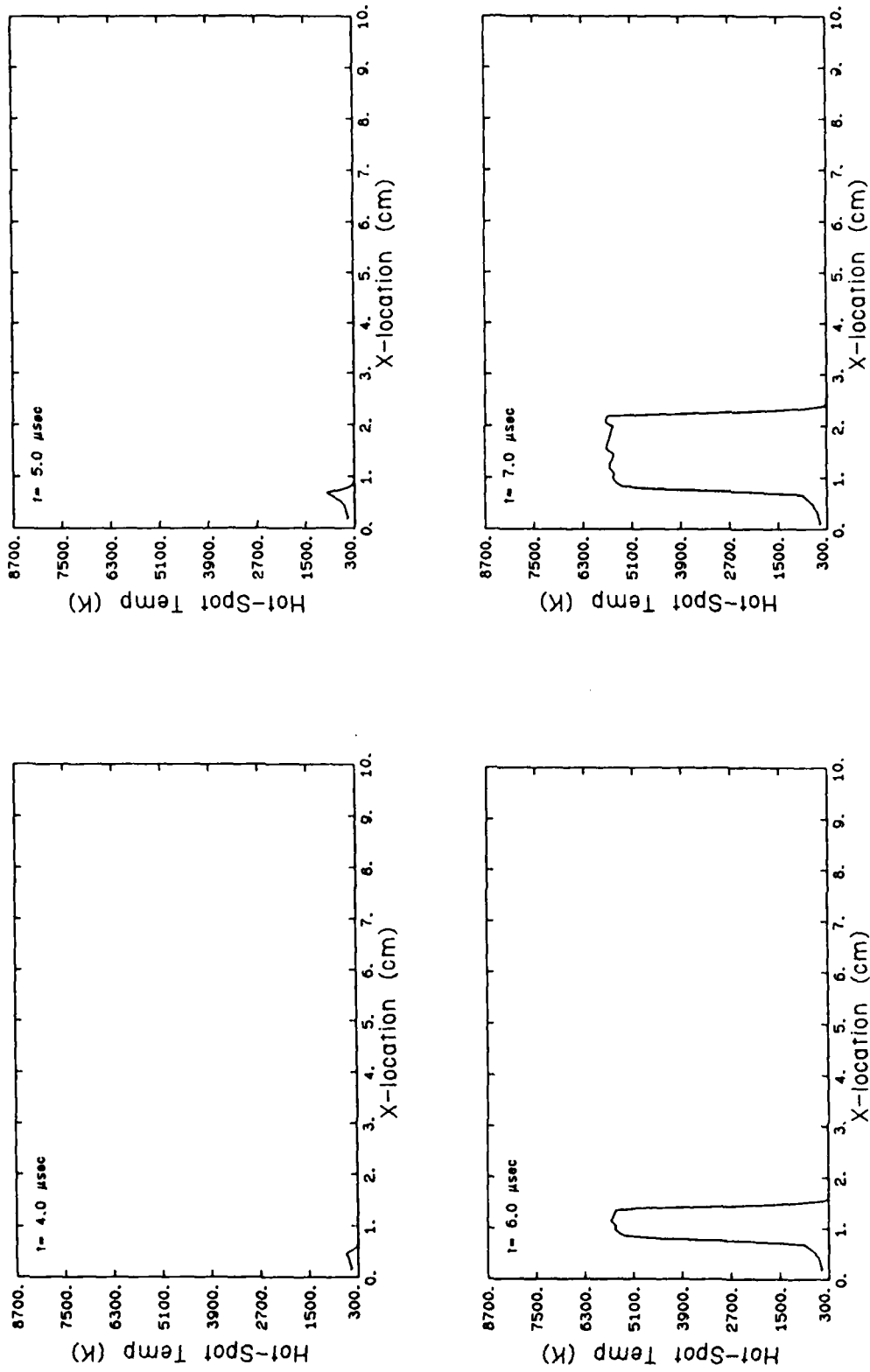


Figure 3.14 Predicted hot spot temperature distribution history for a porous bed of HMX
 $(\alpha_0 = 1.11875, P^* = 4 \text{ GPa}, t^* = 10 \mu\text{sec})$.

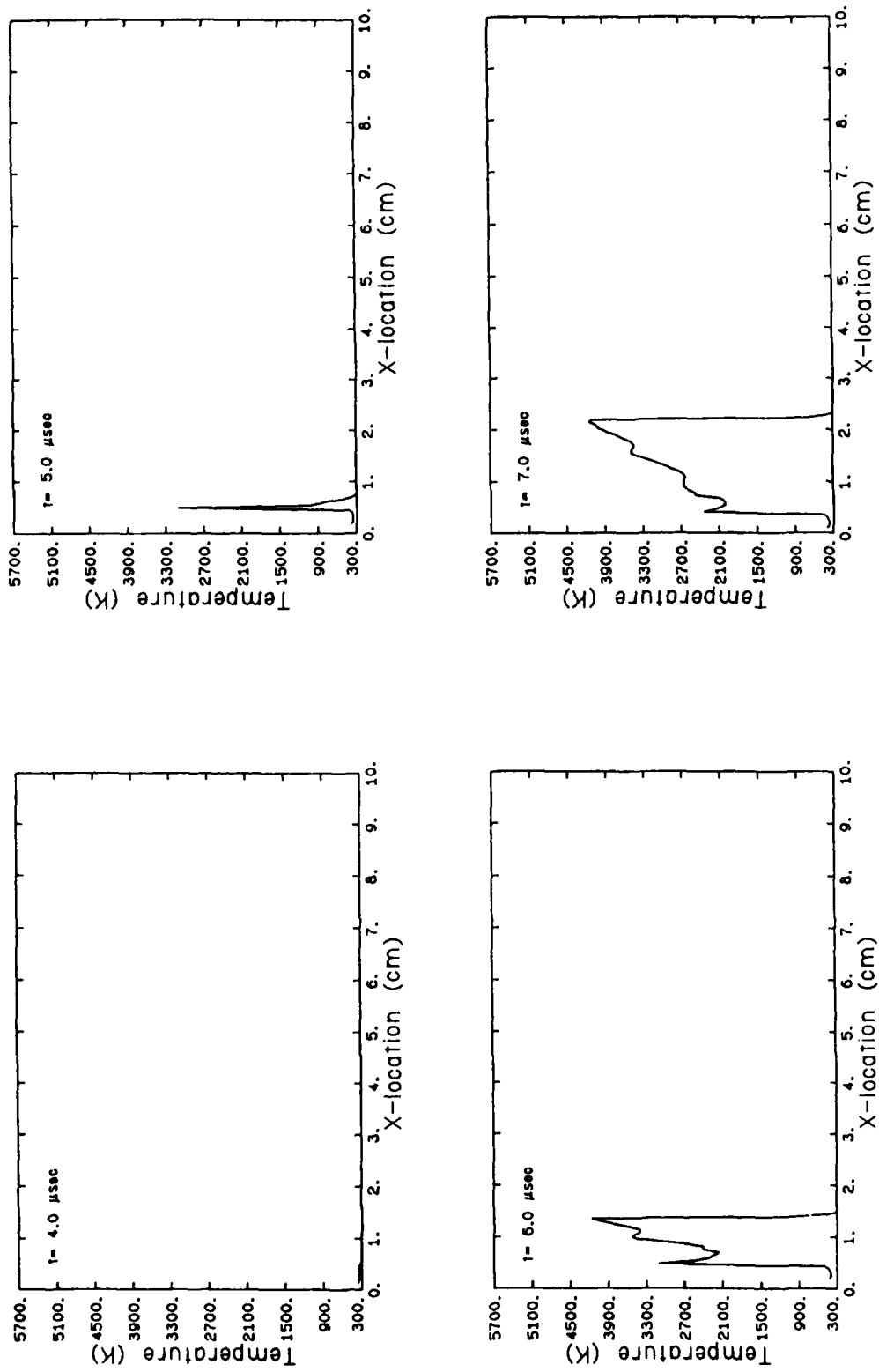


Figure 3.15 Predicted temperature distribution history for a porous bed of HMX
 $(\alpha_0 = 1.1875, p^* = 4 \text{ GPa}, t^* = 10 \mu\text{sec})$.

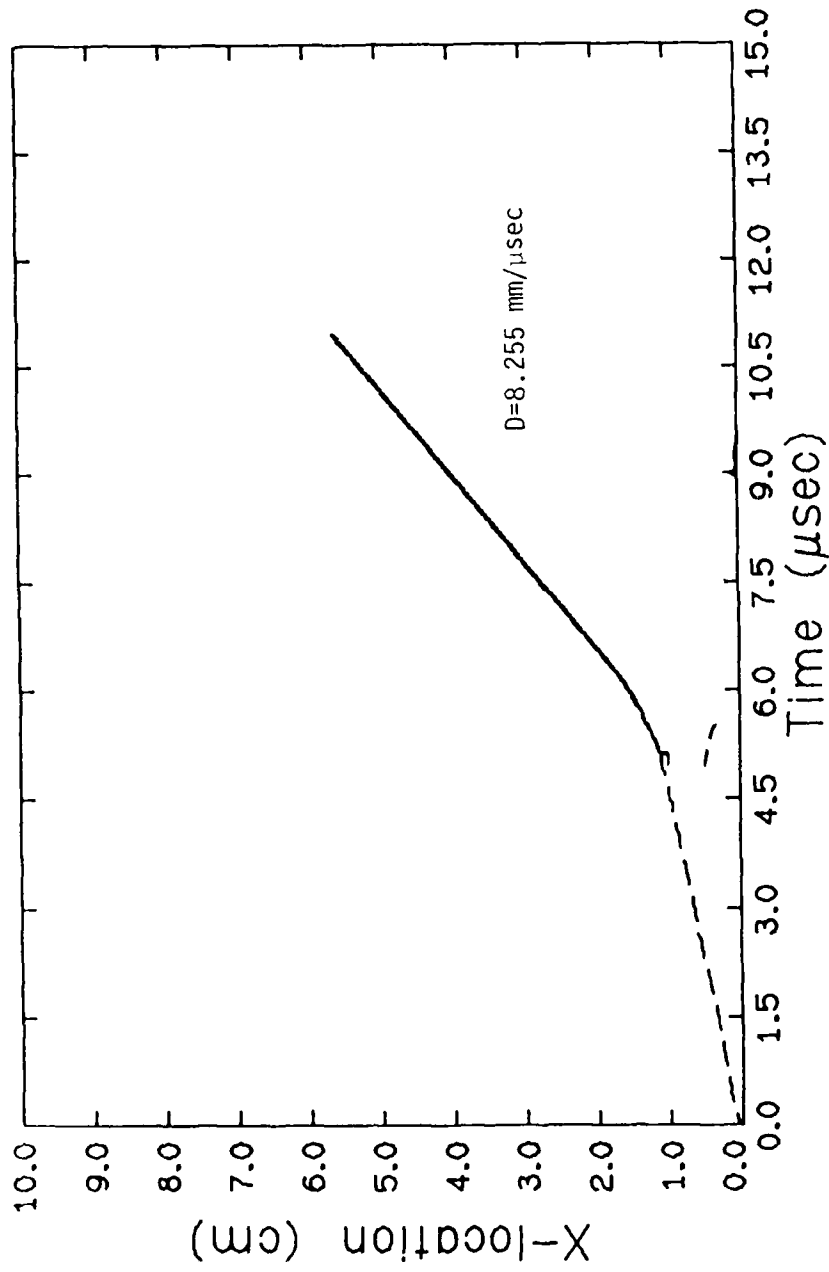


Figure 3.16 Physical plane, showing locus of compression and detonation fronts ($u_0=1.1875$, $p^*=4$ GPa, $t^*=10$ μsec).

The third case treats a material with a relatively high initial porosity, namely $\alpha_0 = 1.4615$ but a relatively weak ramp input wave, $P^* = 2$ GPa and $t^* = 20$ μ sec. Again the five parameters P , α , $(1-W)$, T_H , and T are illustrated in Figures 3.17-3.21, respectively, as time progresses. Similar to the previous case ($\alpha_0 = 1.1875$), no retonation is predicted to occur, but a left traveling compression can be seen. In this particular case a steady CJ pressure of 21.01 GPa and CJ temperature of 4616 K are predicted. One can see a peak in the hot spot temperature in the regime of initial detonation. Since a constant hot spot temperature would be expected after a detonation wave is initiated, the predicted peak in the hot spot temperature (Figure 3.20) is assumed to be caused by inaccuracies in the numerical steps used to obtain a hot spot temperature. The physical plane, shown in Figure 3.22, again presents the location and time of the occurrence of detonation, $x = 2.68$ cm and $t = 21.55$ μ sec. The slope of the solid line represents the detonation velocity, $D = 7.24$ mm/ μ sec.

3.4 Numerical Accuracy Test

In addition to the cases just shown, a comparison was made of the pressure profile for two different initial discretized cell dimensions, depicted in Figure 3.23, for HMX with an initial porosity, $\alpha_0 = 1.2667$, and the imposed stress input condition, $P^* = 5$ GPa and $t^* = 10$ μ sec. One can see that the location of the compression wave for both initial grid spacings is approximately the same for the first two steps illustrated. However, the difference in the pressure magnitudes for the two initial grid spacing is sufficient to cause a detonation wave to be predicted later in the larger initial grid spacing. The corresponding location and time of detonation for

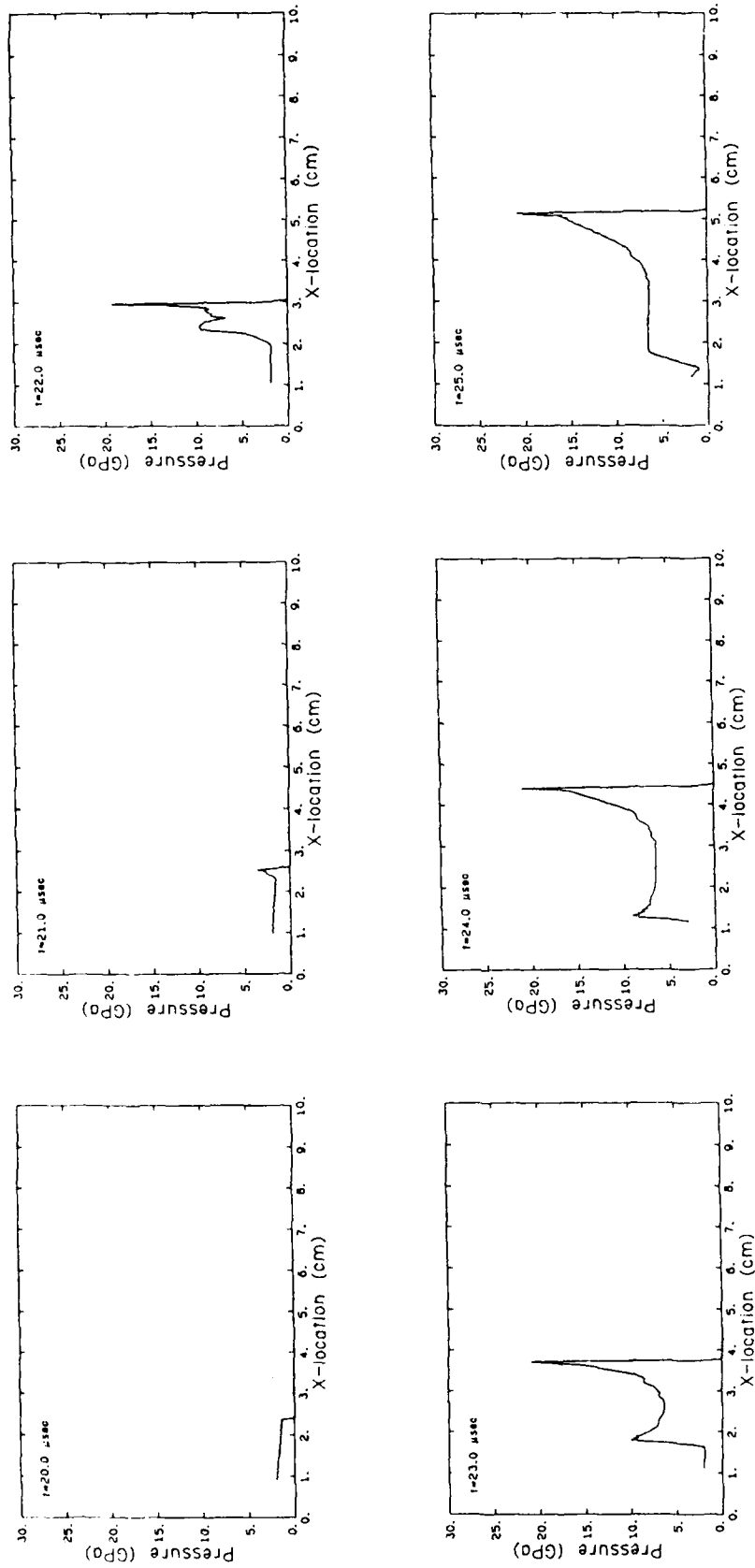


Figure 3.17 Predicted pressure distribution history for a porous bed of HMX
 ($\alpha_0 = 1.4615$, $p^* = 2$ GPa, $t^* = 20 \mu\text{sec}$).

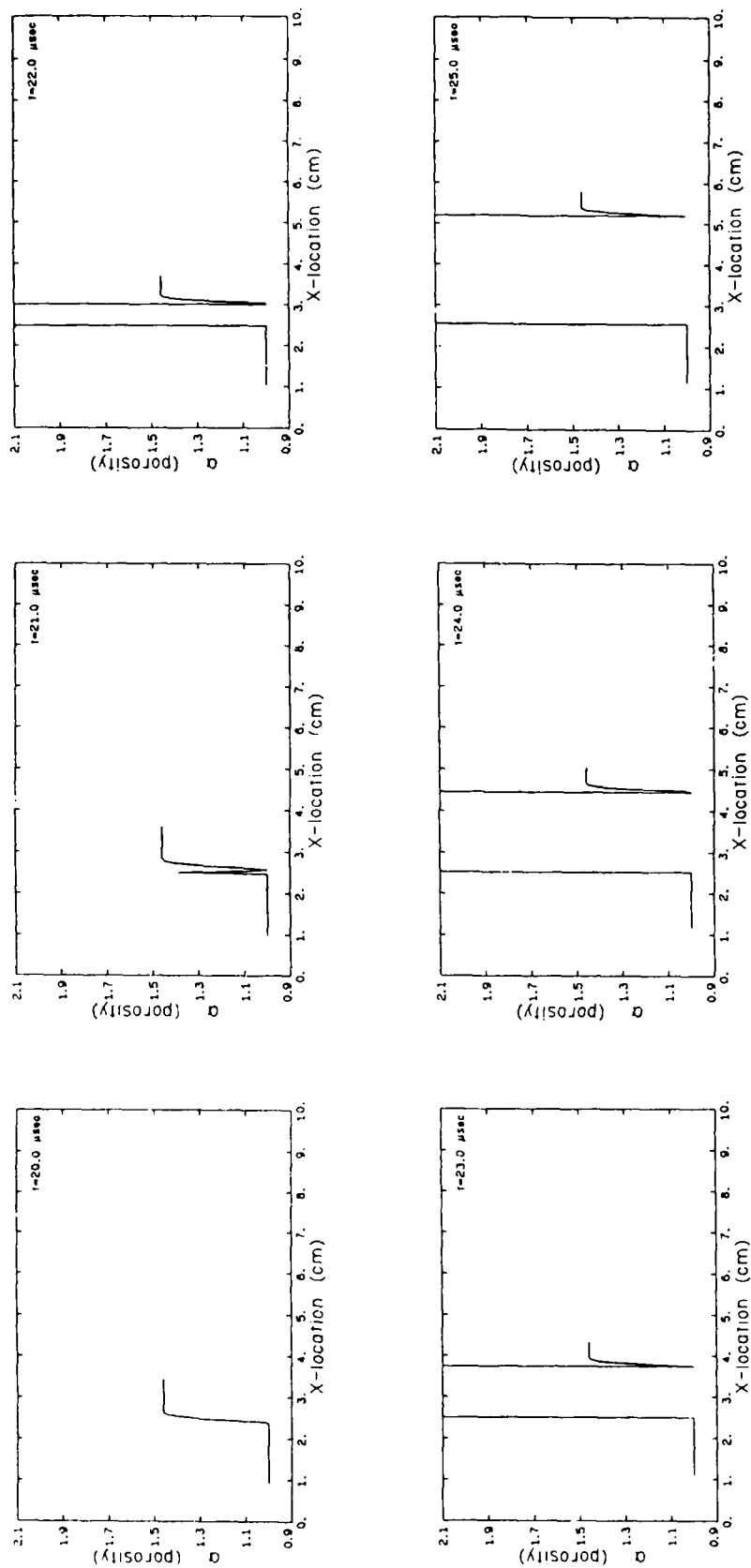


Figure 3.18 Predicted porosity distribution history for a porous bed of HMX
 $(\alpha_0 = 1.4615, p^* = 2 \text{ GPa}, t^* = 20 \text{ } \mu\text{sec}).$

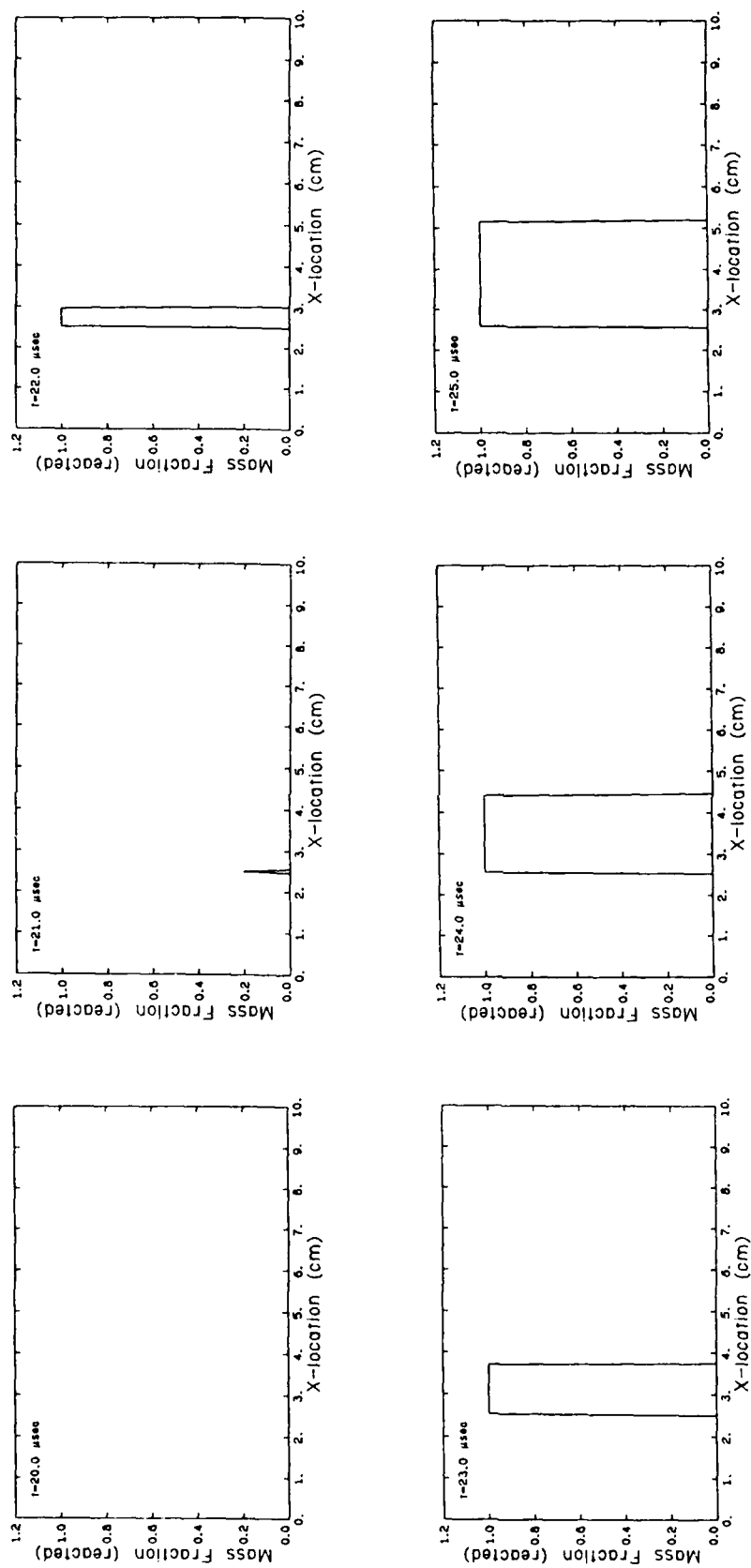
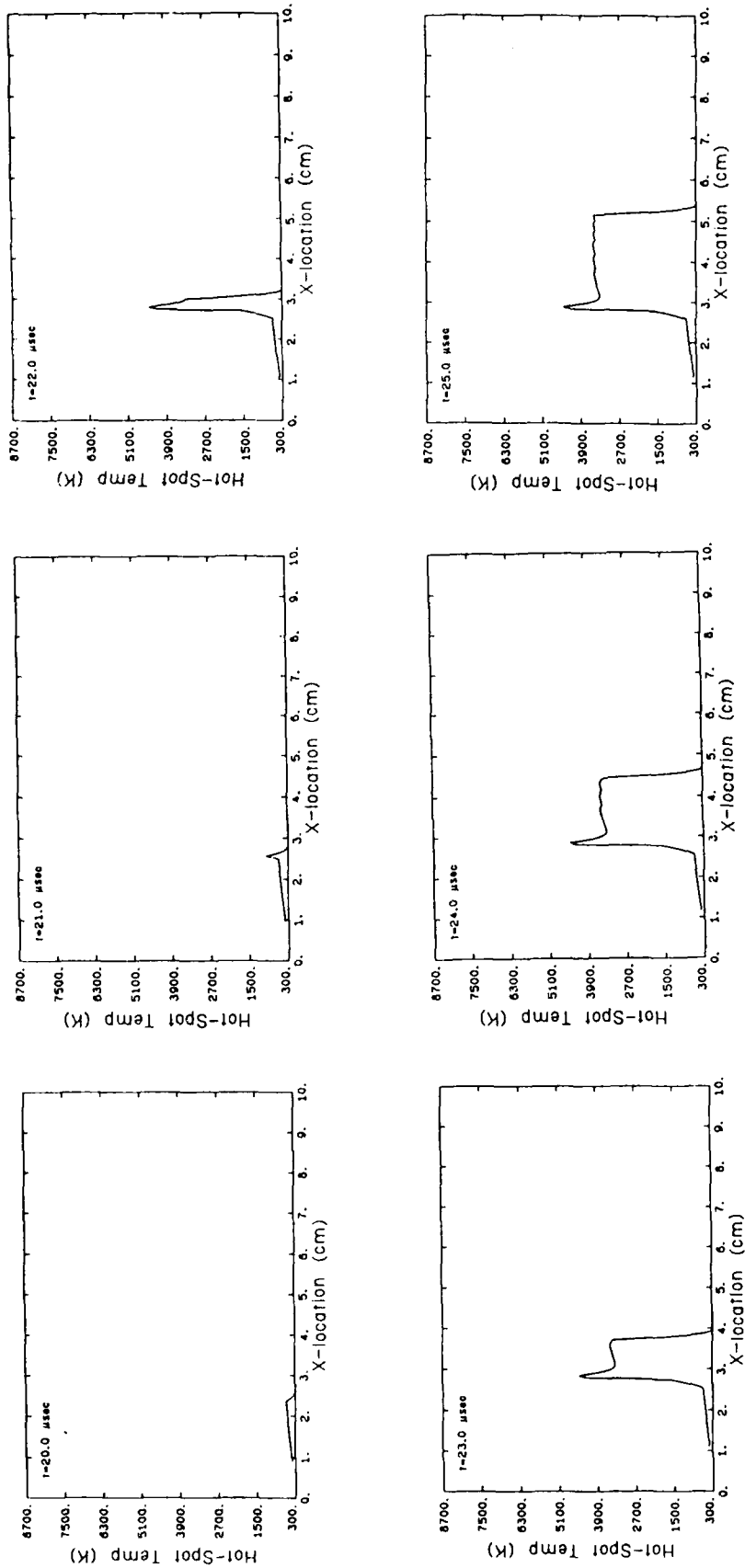


Figure 3.19 Predicted unreacted mass fraction distribution history for a porous bed of HMX
 ($\alpha_0 = 1.4615$, $P^* = 2$ GPa, $t^* = 20$ μsec).



• Figure 3.20 Predicted hot spot temperature distribution history for a porous bed of HMX
 ($\alpha_0 = 1.4615$, $p^* = 2$ GPa, $t^* = 20 \mu\text{sec}$).

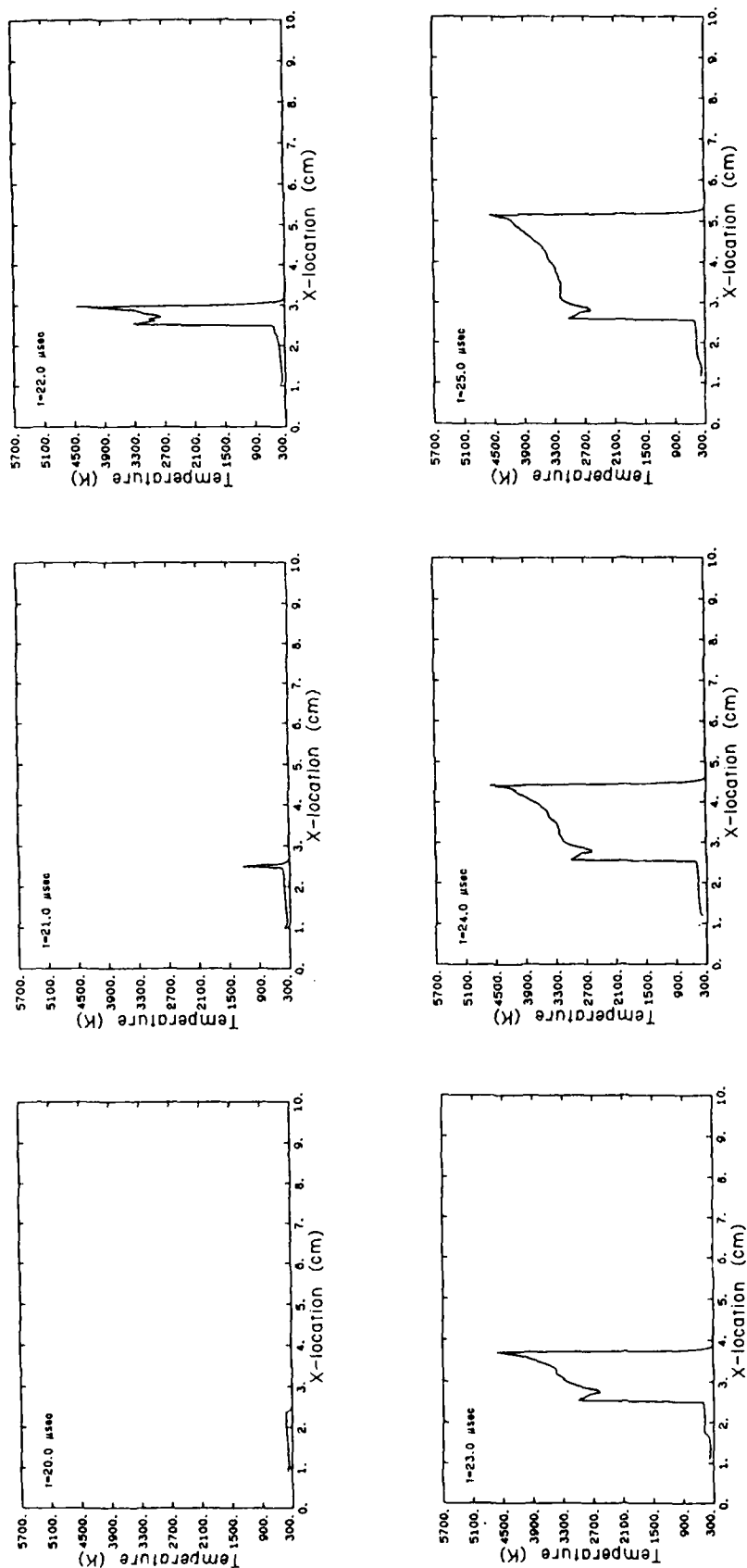


Figure 3.21 Predicted temperature distribution history for a porous bed of HMX ($\alpha_0 = 1.4615$, $p^* = 2$ GPa, $t^* = 20 \mu\text{sec}$).

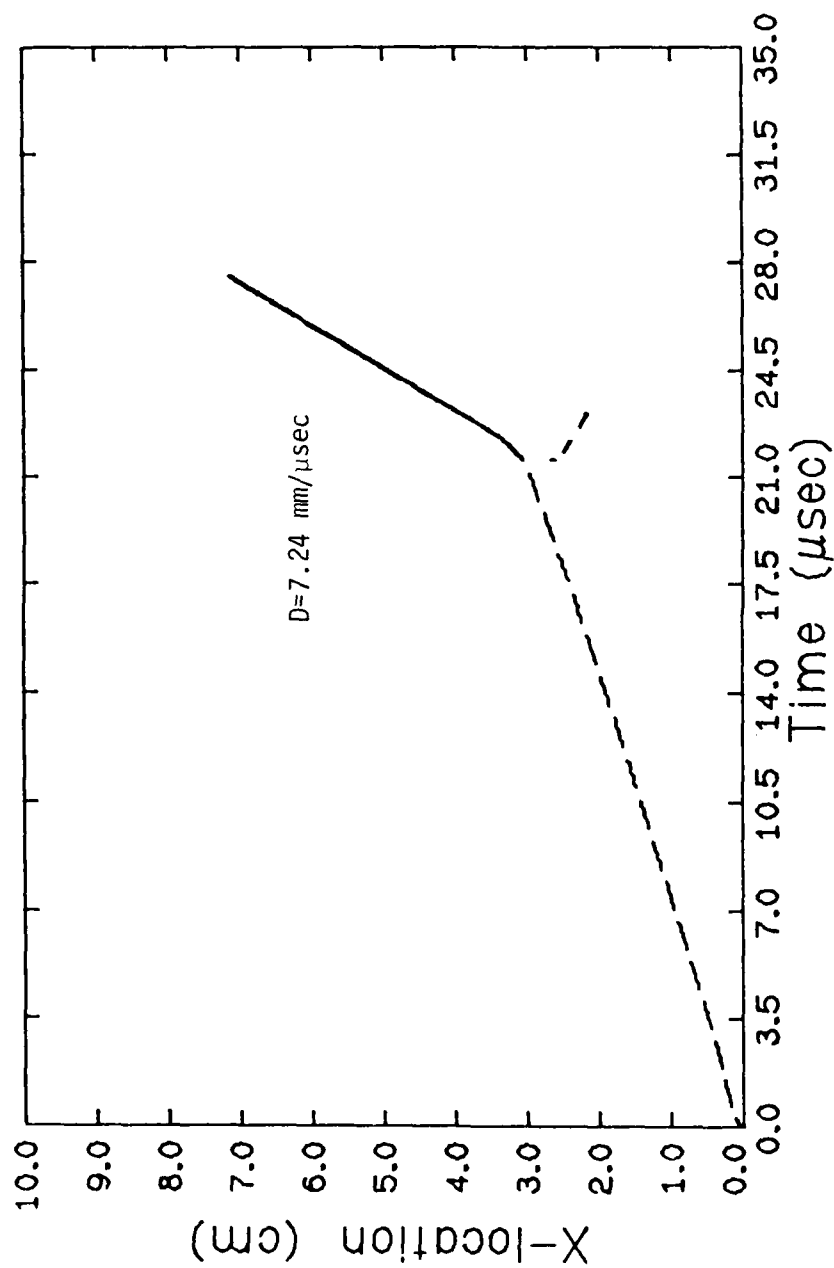


Figure 3.22 Physical plane, showing locus of compression and detonation fronts ($\alpha_0 = 1.4615$, $p^* = 2 \text{ GPa}$, $t^* = 20 \mu\text{sec}$).

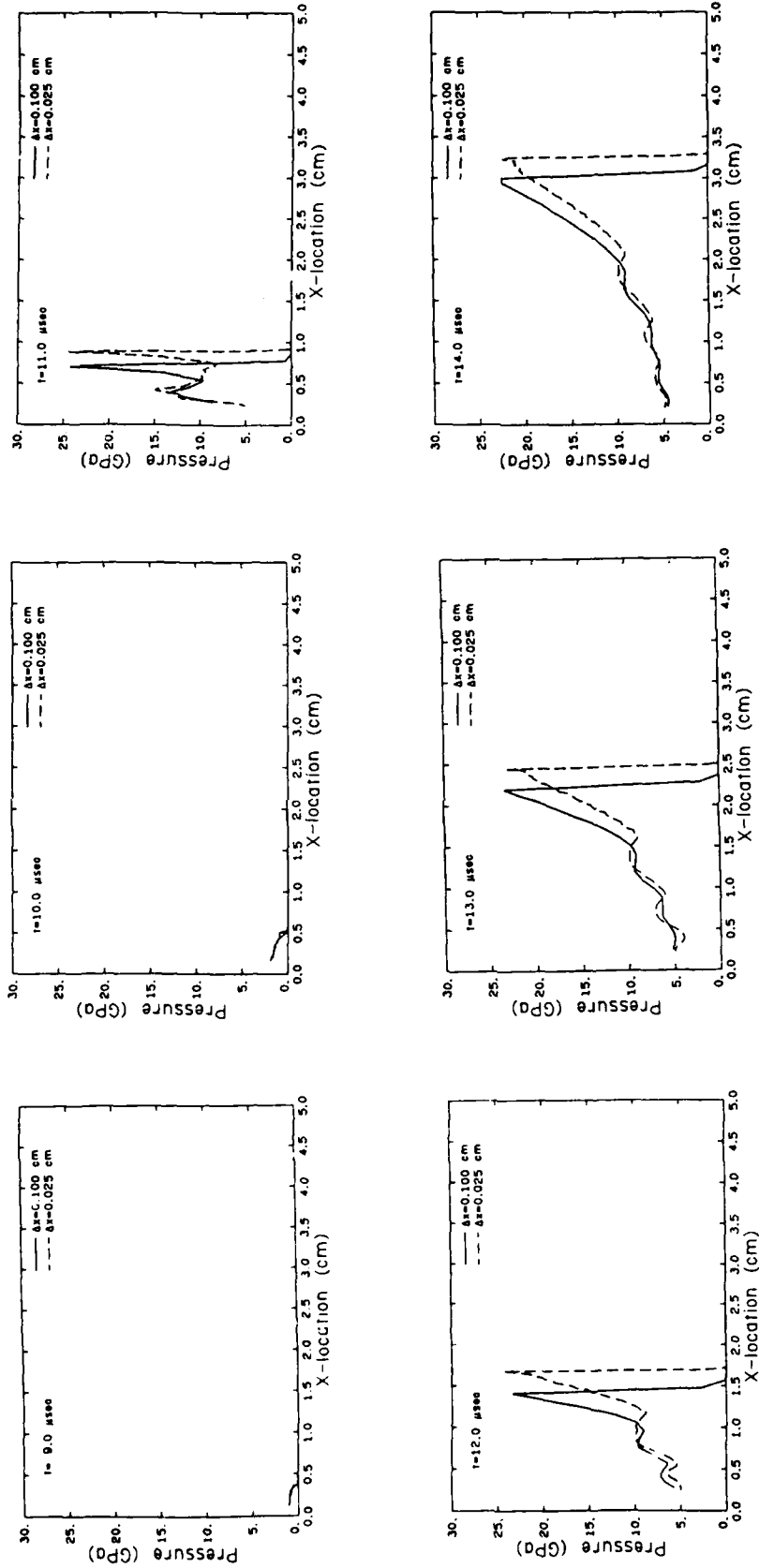


Figure 3.23 Predicted pressure distribution history for a porous bed of HMX utilizing two different initial cell dimensions but the same input conditions ($\alpha_0 = 1.2667$, $p^* = 5$ GPa, $t^* = 10 \mu\text{sec}$).

the initial cell dimensions, $\Delta x = 0.1$ cm and $\Delta x = 0.025$ cm, is $x = 5.189$ mm, $t = 10.65$ μ sec, and $x = 5.668$ mm, and $t = 10.59$ μ sec, respectively. Also notice at $t = 14$ μ sec, the larger initial grid spacing does not capture the peak pressure.

For the majority of cases studied here (and due to a limited amount of computer funds) a minimum initial cell size was chosen as $\Delta x = 0.05$ cm. This value allowed us to retain essential features of the shock initiation physics. Furthermore, for the parametric studies carried out here the basic trends will still be accurate. Nevertheless, quantitative results, such as the point of detonation initiation may be somewhat in error.

3.5 Comparison of the Combustion Models

Shown in Figure 3.24 is a comparison of the predicted shock run-up to detonation length for combustion models CB1 and CB2, for an input condition of $P^* = 2$ GPa and $t^* = 10$ μ sec. The two models agree exactly for the last four high α_0 values studied. However, there is a considerable difference for the low porosity case, $\alpha_0 = 1.1176$. In addition, utilizing combustion model CB1, a detonation was not produced for the low initial porosity of $\alpha_0 = 1.0566$, when $P^* = 2$ GPa and $t^* = 10$ μ sec.

Figure 3.25 illustrates the predicted pressure profile for an $\alpha_0 = 1.1176$, employing CB1. Notice that the detonation is predicted to occur at a much later time, and a substantial distance behind the compression front, as compared to the same case employing CB2, previously shown in Figure 3.5. However, the essential features, that is, detonation and detonation velocities with the same CJ properties are predicted. Figure 3.26 shows the predicted temperature profile with the resulting CJ conditions, while the physical

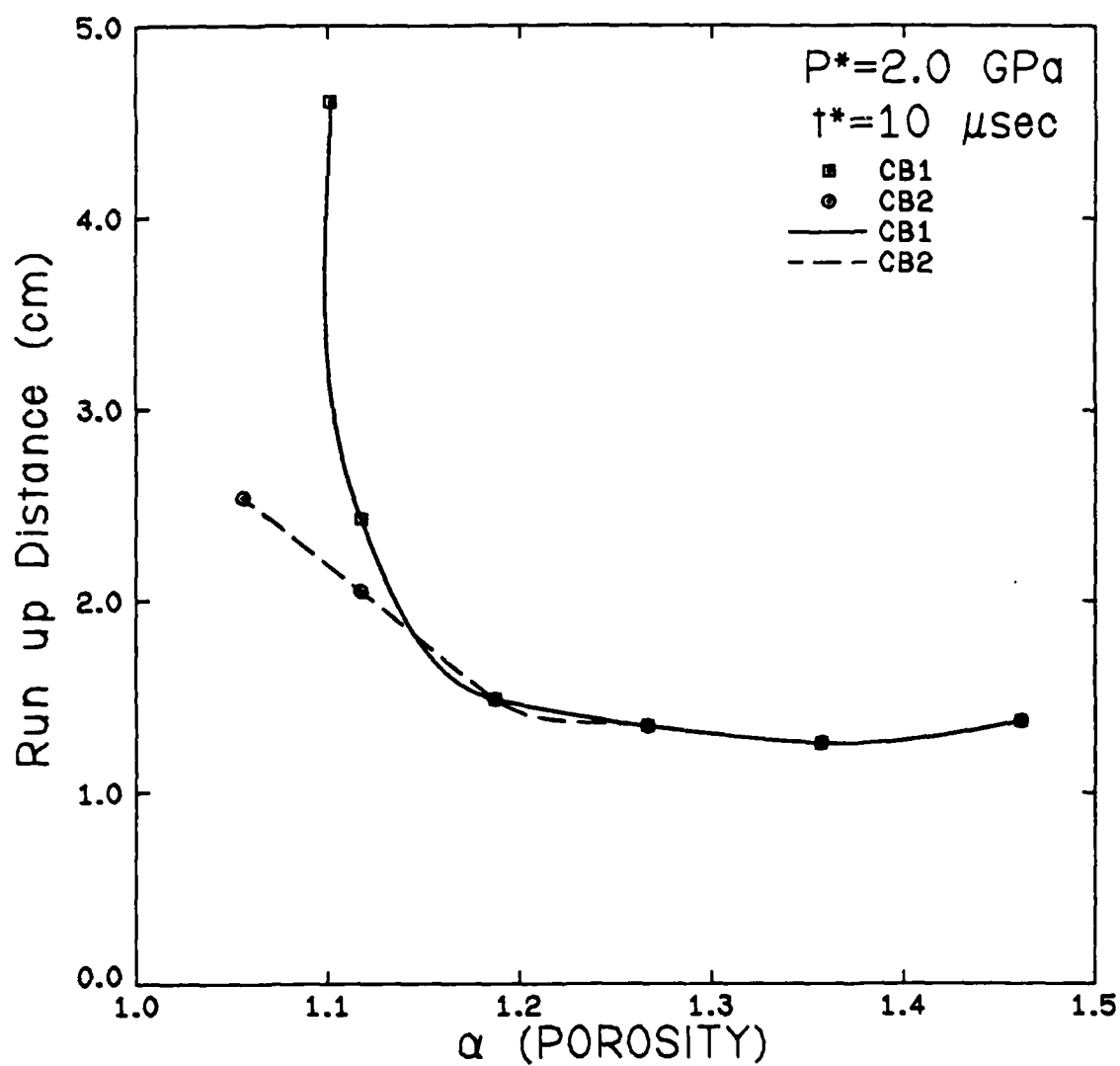


Figure 3.24 A comparison of combustion model CB1's and combustion model CB2's predicted run-up distance versus porosity utilizing a specific input condition ($P^* = 2 \text{ GPa}$, $t^* = 10 \text{ } \mu\text{sec}$).

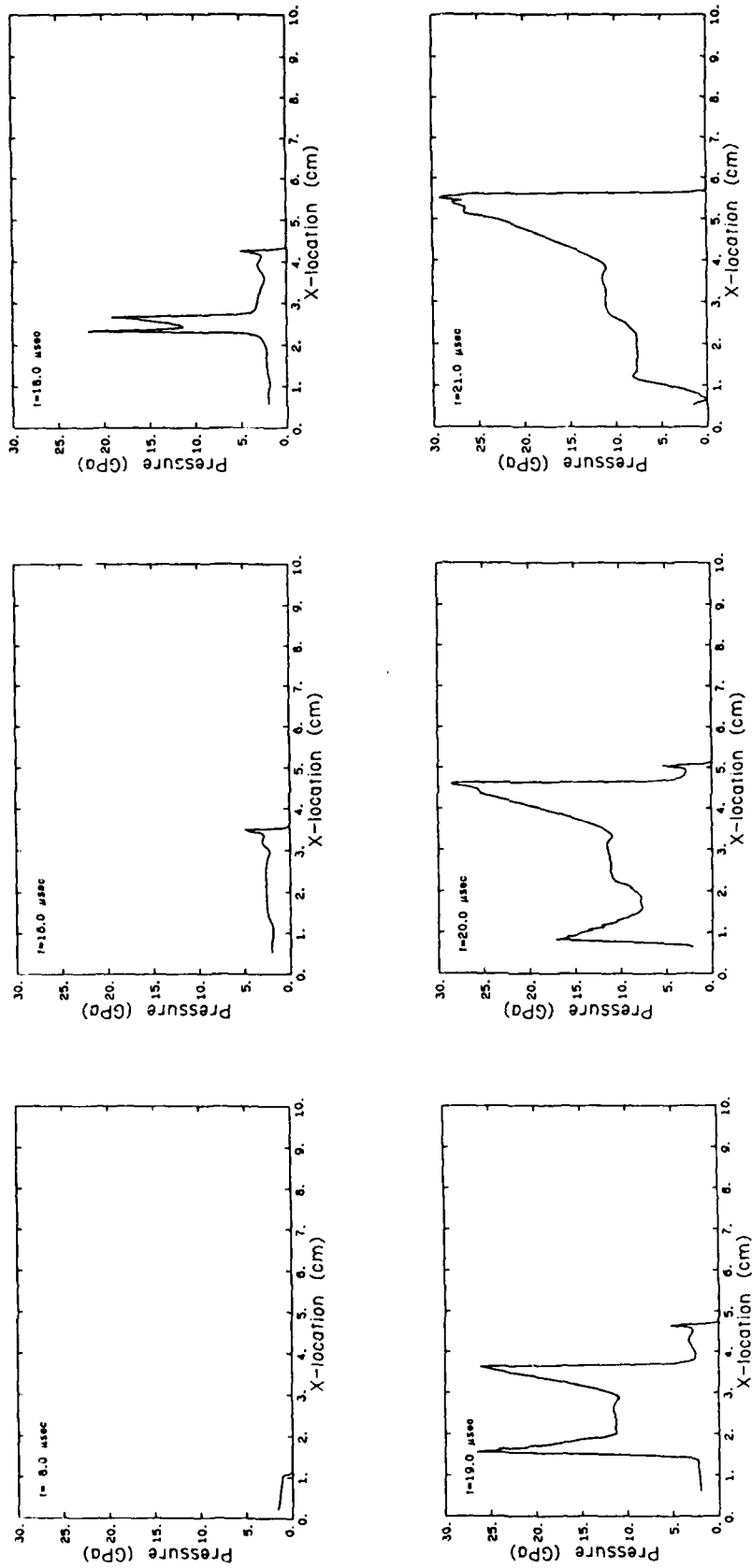


Figure 3.25 Predicted pressure distribution history for a porous bed of HMX utilizing combustion model CBI ($\alpha_0 = 1.1176$, $P^* = 2$ GPa, $t^* = 10 \mu\text{sec}$).

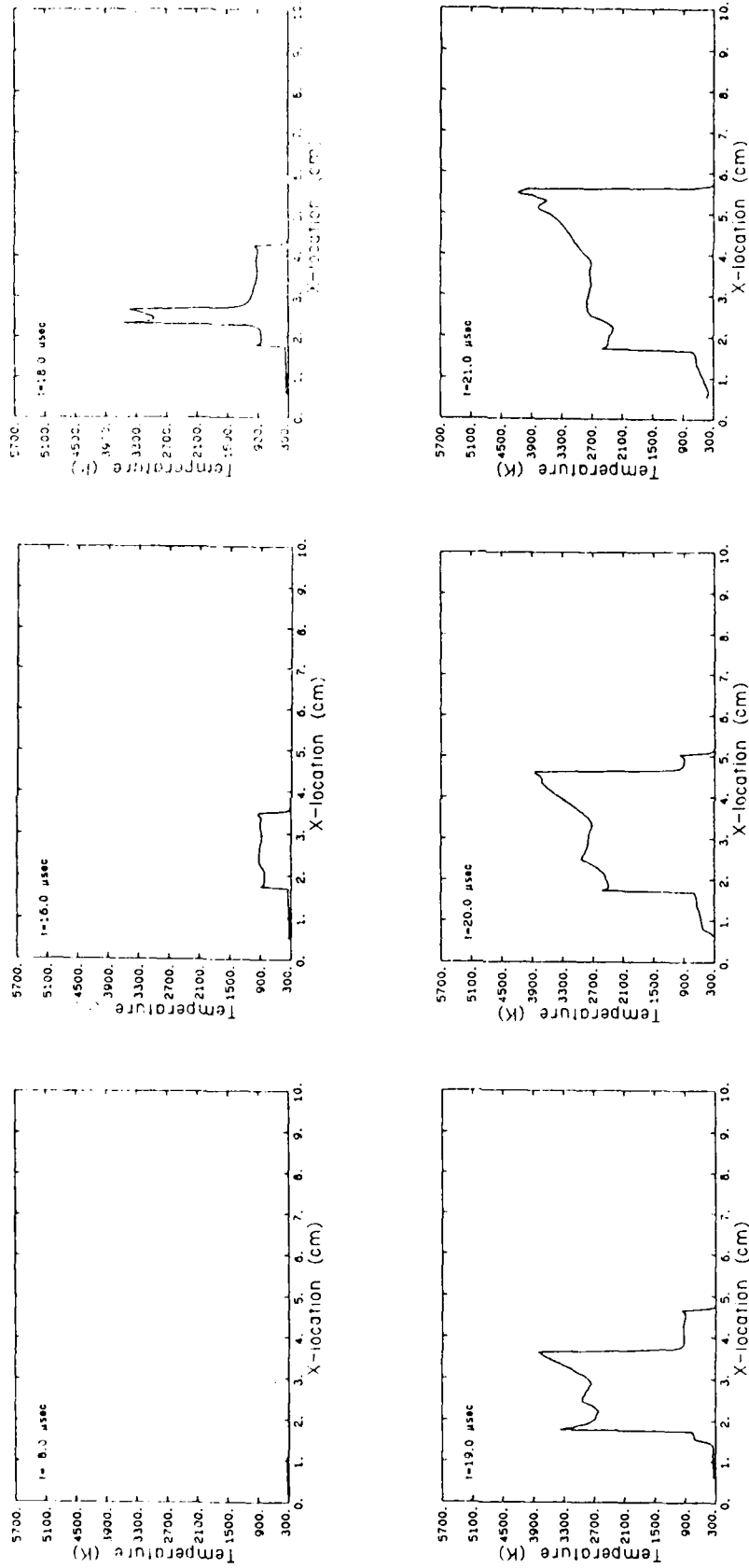


Figure 3.26 Predicted temperature distribution history for a porous bed of HMX utilizing combustion model CB1 ($\alpha_0 = 1.1176$, $P^* = 2$ GPa, $t^* = 10 \mu\text{sec}$).

plane, presented in Figure 3.27, shows the detonation and retonation velocities.

Since CB2 was able to produce detonations in both low porosity cases studied, and only slight disagreements were found in the predicted CJ properties between the models, combustion model CB2 is the logical choice. Table 3.2 lists the CJ parameters along with the detonation velocities for all the porosities studied. Comparing Tables [2.1] with Table [3.2], one can see that, although agreement between the TIGER equilibrium calculations [23] and the predicted results presented in Table [3.2] are not exact, the same qualitative trends are present. However, problems did occur in predicting the proper P_{CJ} . The proper P_{CJ} can be predicted, with some effort, by readjusting the artificial viscosity coefficients for each porosity.

Furthermore, from the results presented in Figure 3.24, one can clearly conclude that α is not a dominant factor in the effective run-up distance to detonation for the interval $1.15 < \alpha_0 < 1.4615$. One would expect a decrease in run-up distance to detonation as the porosity increases. However, for $\alpha_0 = 1.4615$ an actual increase in run-up distance is predicted, although the time to detonation, displayed in Figure 3.28, always decreases monotonically for increasing porosity. A possible cause for the increase in run-up distance can be attributed to the amount of initial void volume. Figure 3.29 portrays the location of the left boundary as a function of time, utilizing an input condition with $P^* = 3$ GPa and $t^* = 40$ μ sec. One can clearly see, an effect of the initial void volume, namely that for the greater porosities the left boundary shifts further into the bed. Since the run-up distance is measured from the initial location of the left boundary to the location of the first Lagrangian finite difference cell to detonate, the

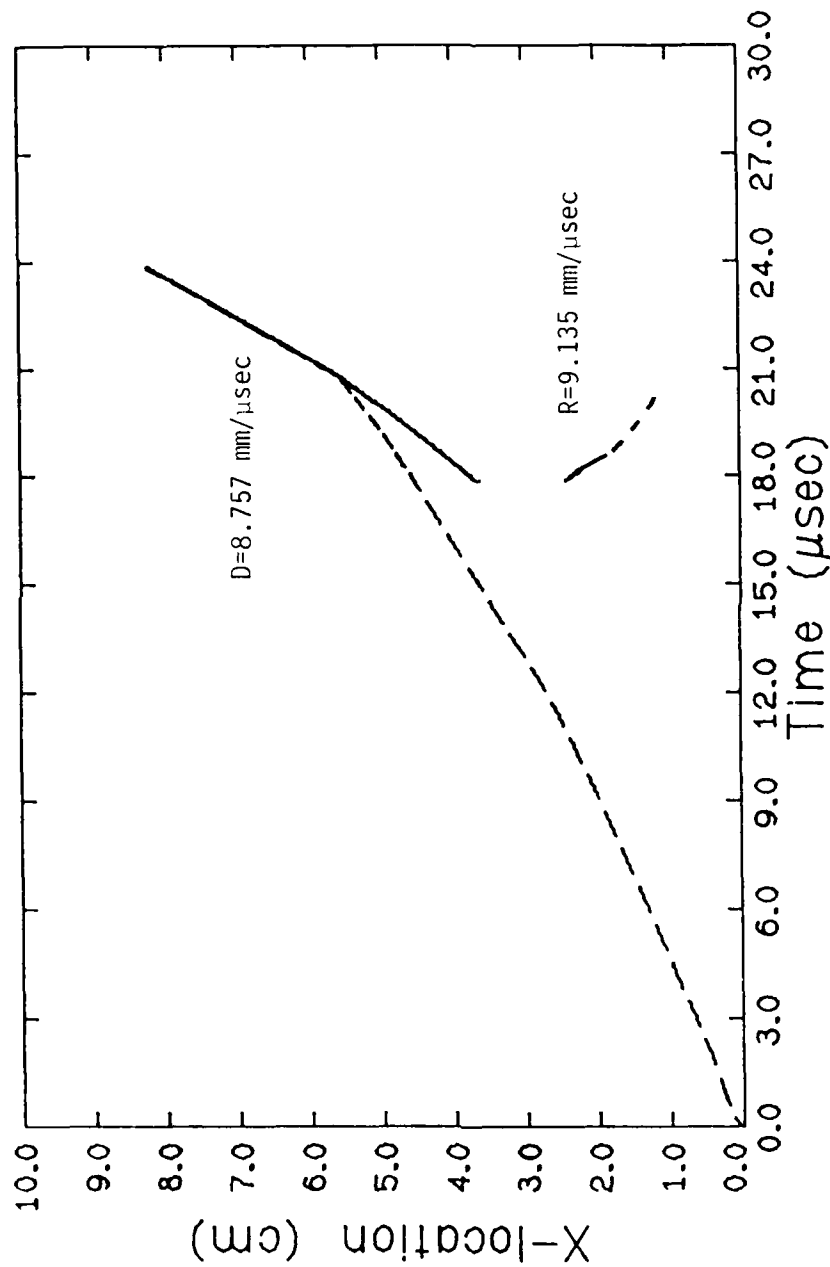


Figure 3.27 Physical plane, showing locus of compression, detonation, and detonation fronts ($\alpha=1.1176$, $p^*=2$ GPa, $t^*=10$ μ sec). In this particular case Combustion model CB1 was utilized.

TABLE 3.2

PREDICTED CJ PARAMETERS

α	ρ_{To} (g/cc)	P_{CJ} (GPa)	T_{CJ} (K)	v_{CJ} (cc/g)	D (mm/ μ sec)
1.0566	1.8	23.76	3532	0.4571	10.48
1.1176	1.7	24.99	3923	0.4752	8.759
1.1875	1.6	24.03	4151	0.4873	8.480
1.2667	1.5	24.13	4371	0.5006	8.133
1.3571	1.4	21.37	4430	0.5206	7.685
1.4615	1.3	21.16	4629	0.5324	7.177

‡ All results produced with a $P^* = 2$ GPa and $t^* = 10 \mu$ sec.

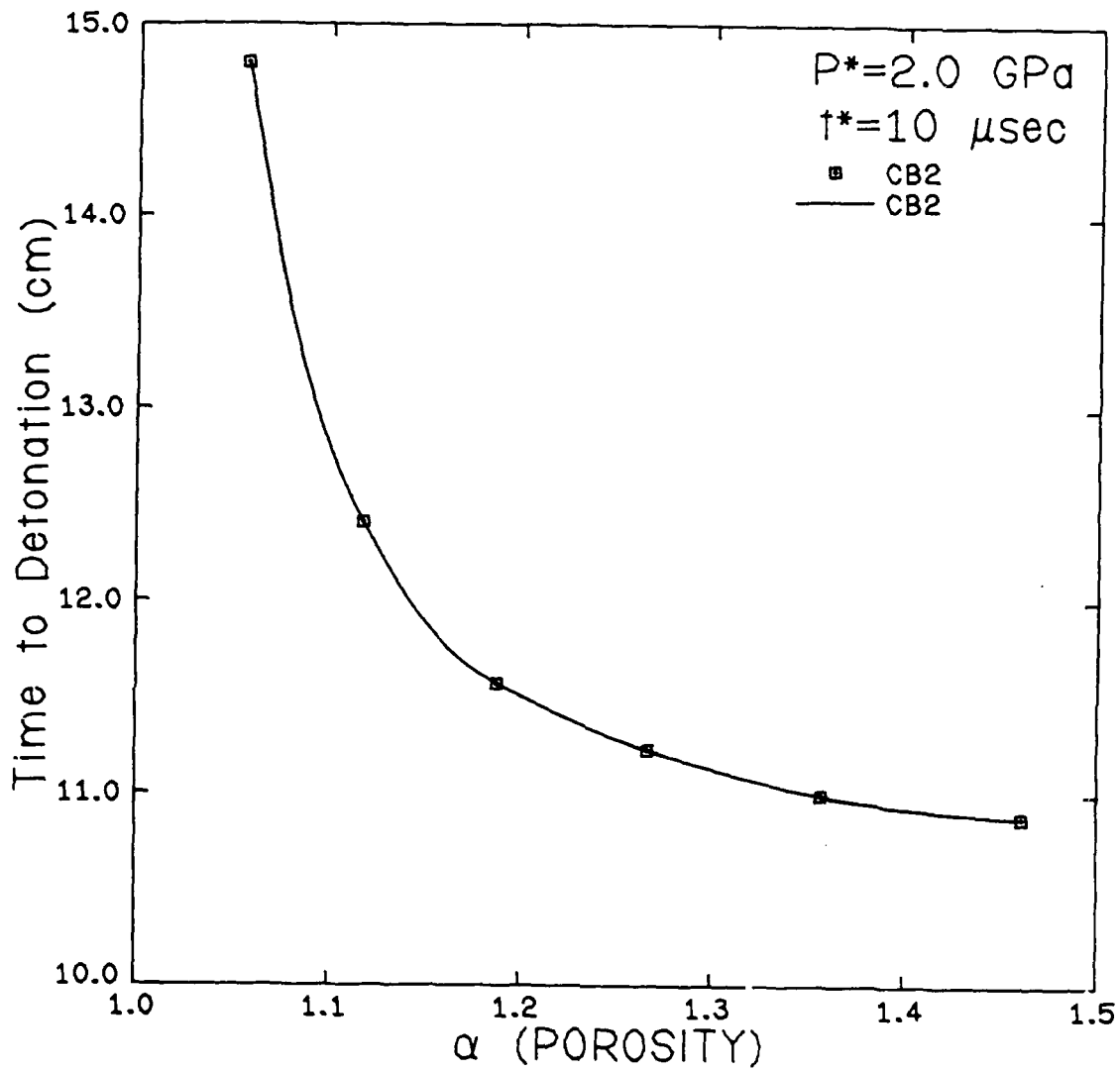


Figure 3.28 Predicted time to detonation versus porosity utilizing combustion model CB2 ($P^*=2.0$ GPa, $t^*=10$ μ sec).

AD-A149 333

ANALYSIS OF SHOCK TO DETONATION TRANSITION (SDT) OF
POROUS HIGH ENERGY PR. (U) ILLINOIS UNIV AT URBANA DEPT
OF MECHANICAL AND INDUSTRIAL ENG. H KRIER ET AL.

2/2

UNCLASSIFIED

SEP 84 UILU-ENG-84-4007 AFOSR-TR-84-1105

F/G 21/9.2

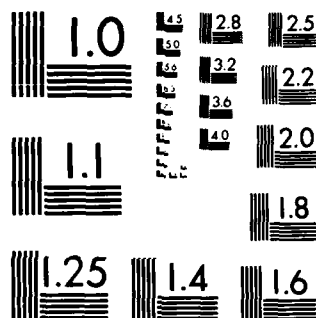
NL



END

FILED

DTIC



MICROCOPY RESOLUTION TEST CHART
NATIONAL BUREAU OF STANDARDS-1963-A

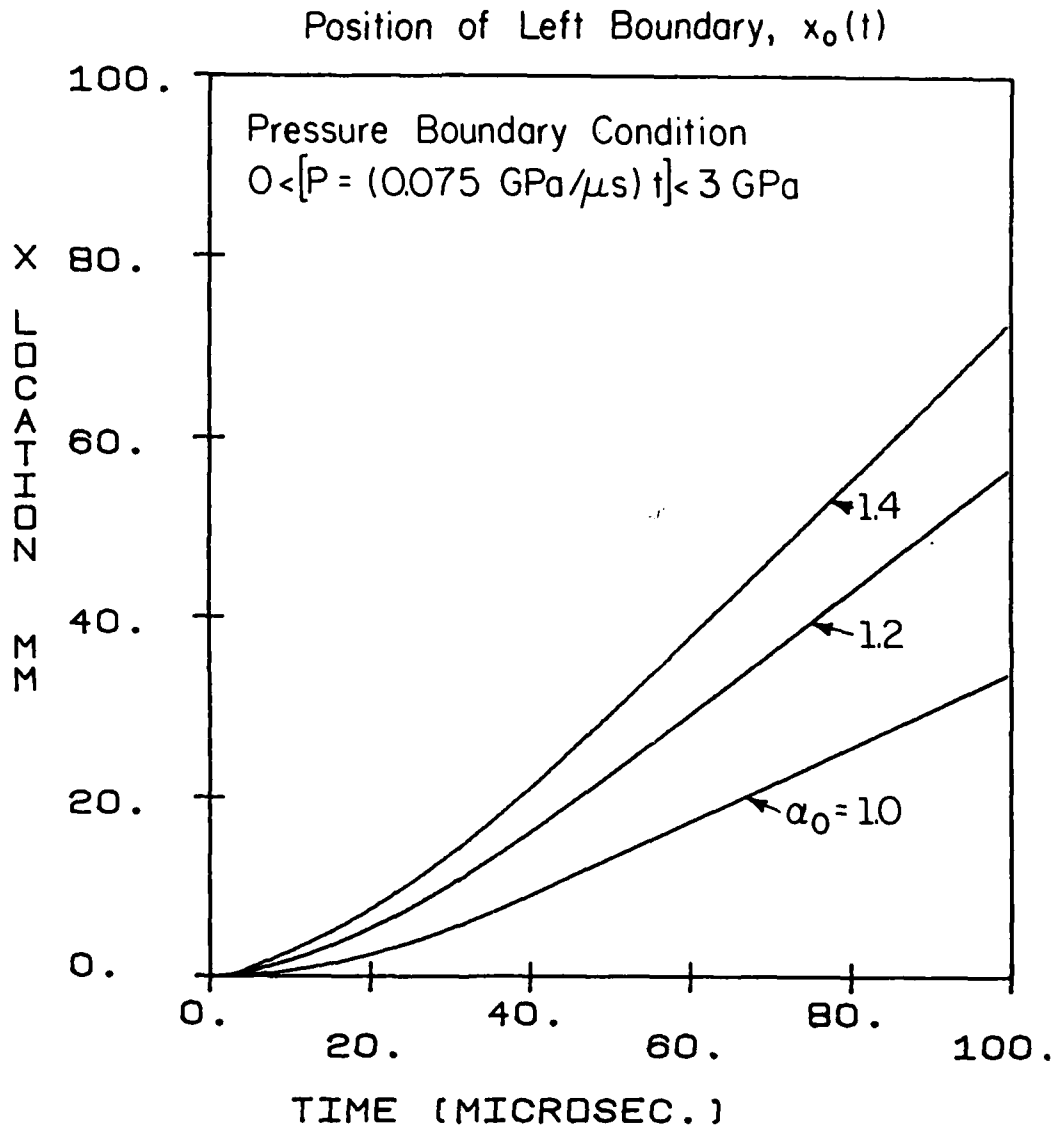


Figure 3.29 Position of the left boundary as a function of time from the finite difference calculations for three different initial porosities, taken from Reference [21]. ($P^* = 3 \text{ GPa}$, $t^* = 40 \mu\text{sec}$).

compaction occurring in the compression front ahead of the point of detonation could be sufficiently large resulting in an increased run-up distance calculated for large porosity conditions. Another probable cause may have been the over extension of Hayes' hot spot theory [17], since the highest porosity he studied was an $\alpha_0 \approx 1.252$.

3.6 Parametric Studies

To conclude the research, two parametric studies were made. The first compared the run-up distances for a fixed porosity ($\alpha = 1.2267$) to various stress input conditions, while the second compared run-up distances for various input pressures with a fixed characteristic rise time ($t^* = 10 \mu\text{sec}$) for different porosities. Figure 3.30 presents the first parametric study. One would expect a greater run-up distance to correspond to a longer characteristic rise time for a specific input pressure, since the compression front will reach the critical pressure needed to initiate detonation later for the longer characteristic rise time. Figure 3.30 demonstrates the occurrence of a longer run-up distance for a specific input pressure corresponding to a longer characteristic rise time. The "Pop plot" (Figure 3.4) shows that for shock initiation of detonation the run-up distance increases with weaker input pressures. Similarly, depicted in Figure 3.30, for "ramp" wave initiation of detonation the run-up distance increases with decreasing input pressures.

By extrapolating data from Figure 3.30 with input conditions having a $P^* = 2 \text{ GPa}$, a long run-up distance to detonation is expected for slow characteristic rise times, displayed in Figure 3.31. Therefore, for low input pressures and critically long characteristic rise times, detonation is not expected to occur in a ten centimeter bed, eliminating the hazard of DSDT.

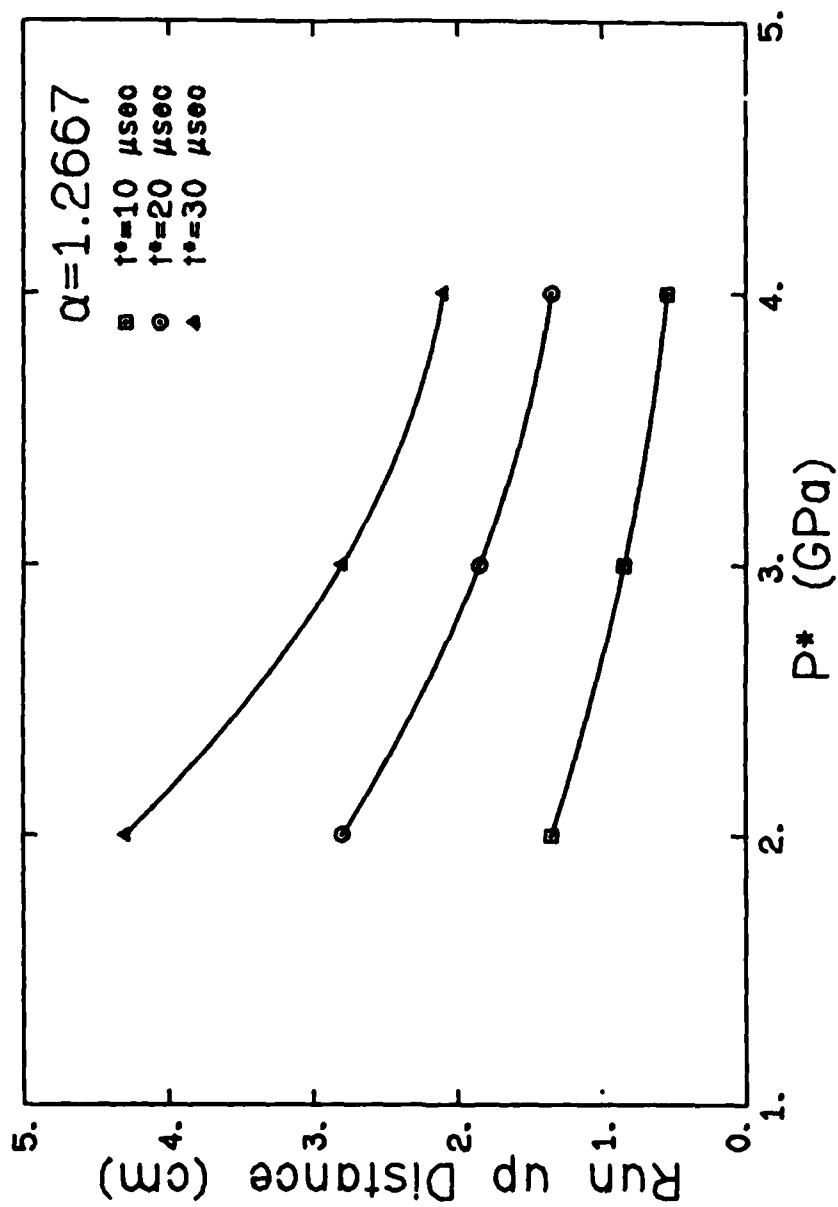


Figure 3.30 Predicted run-up distance versus input pressure for several characteristic rise times ($\alpha_0 = 1.2667$)

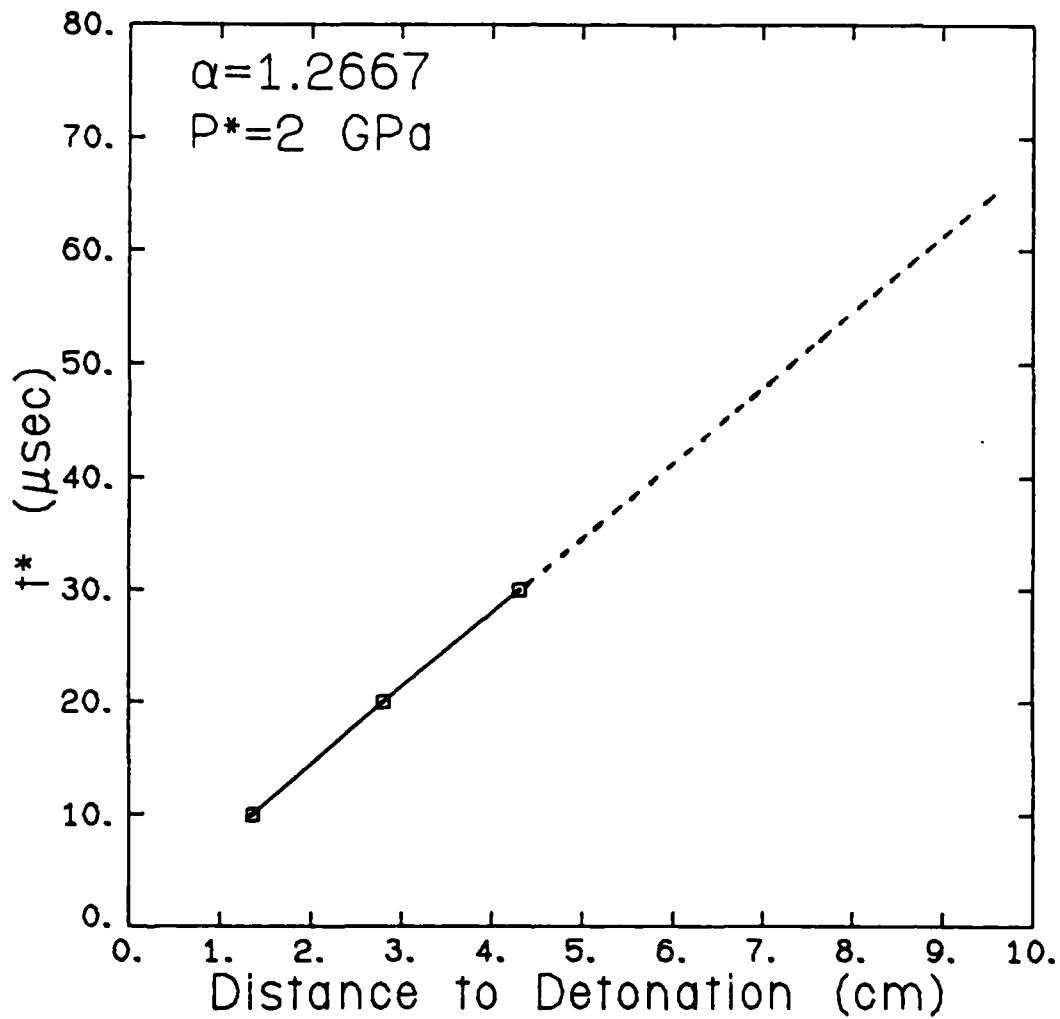


Figure 3.31 An extrapolation to determine the expected run-up distance for relatively long characteristic rise times ($\alpha_0=1.2667$, $P^*=2 \text{ GPa}$).

Moreover, Figure 3.32 shows an increase in run-up distance to detonation to correspondingly weaker input pressures for four specific porosities, $\alpha_0 = 1.1875$, $\alpha_0 = 1.2667$, $\alpha_0 = 1.3571$, and $\alpha_0 = 1.4615$. Evidence of numerical integration errors were encountered for low porosities, $\alpha_0 < 1.15$. Therefore no results are shown. One would expect a higher porosity bed to be more sensitive to detonation than a lower porosity bed, thus resulting in shorter run-up distances. Therefore the curves for different alphas should not cross each other. However, the crossing may be attributed to a coarse initial grid spacing. Although there exists some quantitative errors in Figure 3.32, one may conclude that for porosities, in the interval of $1.15 < \alpha_0 < 1.5$, do not take a dominant role in the run-up distances. Furthermore, at relatively weak inputs, $P^* < 2$ GPa, the run-up distances asymptote to high values, indicating that no detonation would be predicted for input pressures lower than 1.5 GPa.

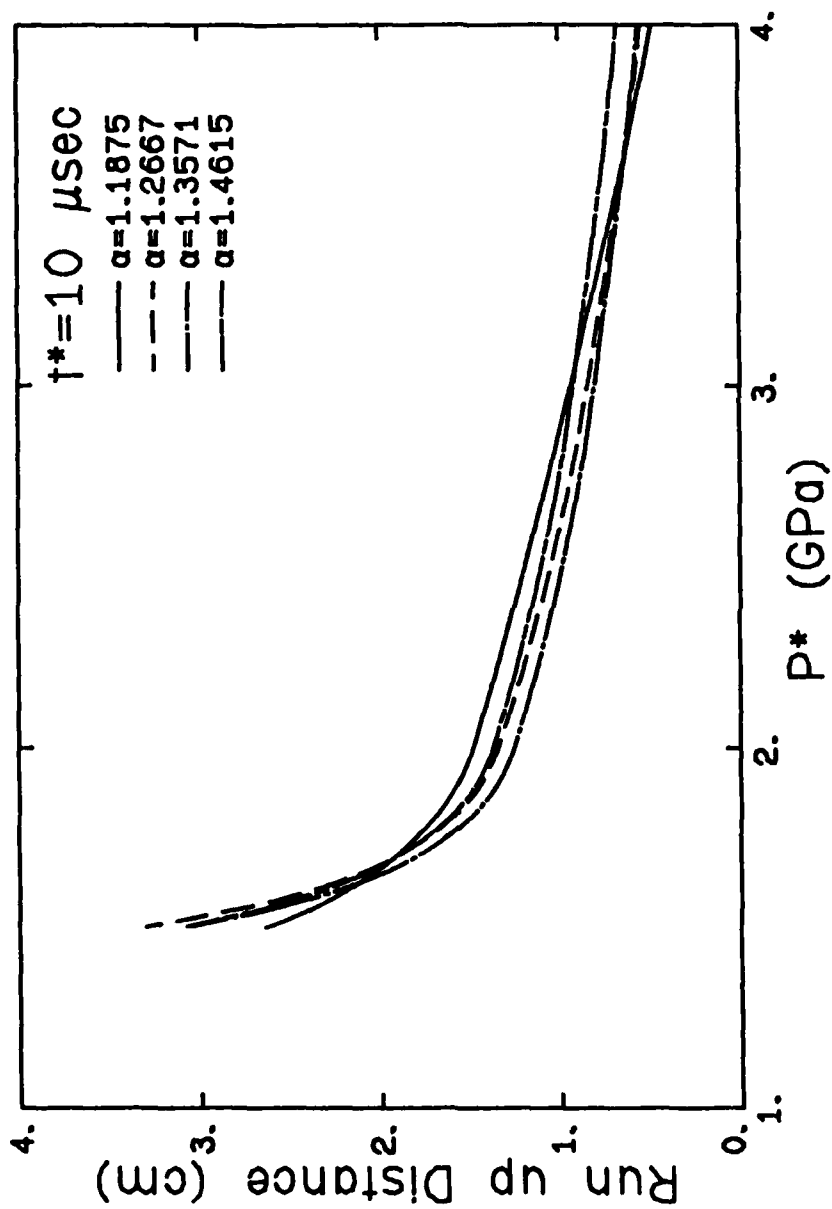


Figure 3.32 Predicted run-up distance versus input pressure for several porosities ($t^* = 10 \mu\text{sec}$).

CHAPTER 4

CONCLUDING REMARKS

The previous chapter presented several numerically produced results which depicted the five-part scenario of Deflagration to Shock to Detonation Transition. Although some integration inaccuracies in the predicted results were encountered, the results clearly showed that "Ramp" wave to Detonation Transition is a prominent hazard associated with porous explosives. One of the purposes of this last chapter is to recommend necessary improvements for further utilization of the code.

4.1 Necessary Improvements

Two areas clearly in need of improvements are: (1) the need for a better integration scheme to define the shock waves, and (2) a better data base to calculate the hot spot temperature and subsequent reaction rates. One of the first steps that should be taken to accurately define the shock would be to reduce the amount of artificial viscosity. By doing this, the shock wave will be spread over a smaller amount of grid spaces. If additional increased computer funding becomes available, it is recommended that the initial finite difference cell sizes be reduced by $1/2$ to $1/4$. The result of both reducing the artificial viscosity and initial cell size will be better representation of the shock structure, which should alleviate most of the numerically encountered problems. Furthermore, a more careful definition of the shock structure will allow a more accurate calculation of the hot spot temperature, since one of the errors associated with the determination of a hot spot temperature stems from the relatively poor numerical representation of the

shock structure. Basically, an inaccurately distributed shock wave results in an error in the evaluation of the irreversible energy, since the compression process is performed over several cells.

Moreover, since the reaction of a porous material initiates and is controlled in the initial stages of decomposition by the hot spot, a better data base is needed to accurately determine the hot spot temperature and decomposition rates. Although the Hayes hot spot theory [17], incorporated in the code, modeled initiation and decomposition exceptionally well for materials with high porosities, the theory began to collapse when α was less than 1.15. Therefore, it is suggested that research should be conducted on the formulation of a model for the localized hot spots on a microscale, both experimentally and theoretically. Also, directly related to the hot spot temperature, experimentally observed decomposition times should be measured for a wider spectrum of porosities. With a better understanding of the formation and decomposition of hot spots, an improvement in the quantitative results should be possible.

In addition to the two areas just mentioned in need of improvement, a dynamic pore collapse model outlined in Reference [20] should be implemented in the code either to validate or contradict the use of the static pore collapse model now employed. Although Kooker and Anderson [9] found in their studies that the static pore collapse theory sufficiently modeled compaction, the inertial and viscous terms contained in the dynamic pore collapse model may be of significance in defining the rapid compression arising from a steady state detonation wave.

4.2 Importance of the Work

Although the code did not successfully produce accurate quantitative results for the lowest porosities studied here, the key elements of the five-part scenario were modeled predicting a steady state detonation and, in some instances, the occurrence of a retonation. The model was validated by a comparison with an experimentally produced run-up length versus peak shock variation, the so-called "Pop plot". This comparative study showed the analysis to be somewhat conservative, predicting shorter run-up distances for a given peak pressure.

However, the slope, λ_{SDT} vs P^* was matched. A parametric study, which varied the input conditions for a specific porosity, showed that longer characteristic rise-time resulted in a longer detonation run-up distance. A second parametric study, which compared run-up distances for different porosity explosives, for various pressure inputs with the same characteristic rise time, illustrated that porosity, in the interval $1.15 < \alpha_0 < 1.5$, was not a dominant factor in the effective run-up distance.

The granulated bed/cast explosive configuration is representative of a rocket motor which has partially fragmented. Even though the length of the fragmented propellant is not long enough to detonate from an accelerated convective burn, the intact propellant may shock initiate from the rapid pressure rise rate. It is evident that "ramp" wave initiation of detonation is truly a serious hazard to contend with, demonstrated by the short run-up distances corresponding to rapid rise rates for several porous cases. However, by the extrapolation of data from the first parametric study, a substantially long run-up length, outside the dimensions of the propellant bed, would result for relatively long rise-time conditions.

If the distance needed to shock initiate the cast material is greater than any dimension of the rocket motor, DSDT is obviously impossible. If the solid rocket propellant is unavoidably frangible, then future formulations should be devised so that, when damaged, the propellant breaks into larger fragments (on the order of $\frac{1}{2}$ millimeter). Flame spreading and convective burning in such effectively large fragments (but smaller surface-to-volume) would result in a local dP/dt that would produce larger t^* .

As a final conclusion, one can clearly state that an alternative methodology for transition to detonation other than the direct acceleration of the convective burn front, is a Ramp Initiated Shock to Detonation Transition in an impermeable but porous propellant.

APPENDIX A

HMX PROPERTIES [9,22,23,26,29]

Explosive: OCTAHYDRO-1,3,5,7-TETRANITRO-1,3,5,7-TETRAZOCINE

Formula: $C_4H_8N_8O_8$ Initial Homogeneous Specific Volume $v_{SO} = 0.5263 \text{ cc/g}$ Ambient Homogeneous Sound Velocity $c_{SO} = 0.2642 \text{ cm}/\mu\text{sec}$ Initial Yield Stress $Y_0 = 51.7 \text{ MPa}$ Initial Shear Modulus $G_0 = 3.516 \text{ GPa}$ Gruneisen Coefficient $\Gamma = 1.1$ Activation Temperature $\frac{E^*}{R} = 14400 \text{ K}$ Frequency Factor $z = 6.9 \times 10^{10}$ Product Gas Constant $\hat{R} = 2870740 \frac{\text{ery}}{\text{gK}}$

Specific Heat (constant volume)

of the solid

$$C_{VS} = 1.5 \text{ J/gK}$$

*Specific Heat (constant volume)

of the product gas

$$C_{VG} = [2.4 - 0.28(\frac{1}{v_{T0}} - 1.3)] \frac{\text{J}}{\text{gK}}$$

*Heat of Detonation

$$H_{DET} = [7.91 - 4.33(\frac{1}{v_{T0}} - 1.3)^2 - 0.934(\frac{1}{v_{T0}} - 1.3)] \frac{\text{kJ}}{\text{g}}$$

*Detonation Velocity

$$D = 3.64(\frac{1}{v_{T0}} - 1.3) + 6.98 \text{ mm}/\mu\text{sec}$$

Covolume Correction Term

 β is listed in Table [2.3]

Nonlinear volume-dependent function obtained

from shock Hugoniot experiments [22]

$$\begin{aligned} J(x) = & 7.57x^2 + 13.33x^3 + 18.04x^4 \\ & + 2.828x^5 + 24.01x^6 + 278.3x^7 \\ & + 383.6x^8 \end{aligned}$$

$$\text{where } x = \frac{v_{so}}{v_s} - 1$$

*Data fits of CJ data predicted by TIGER [23].

APPENDIX B

RECIPROCITY RELATIONS

Since very few mechanical engineers utilize the concept of Helmholtz free energy, a step by step derivation for pressure and specific internal energy from the free energy definition will be presented. Helmholtz free energy is defined to be

$$\psi \equiv e - Ts \quad (B.1)$$

where ψ represents Helmholtz free energy, e , specific internal energy, T , temperature, and s , specific entropy. By taking the derivative of Equation (B.1) the following expression is obtained

$$d\psi = de - Tds - sdT \quad (B.2)$$

Making use of an important thermodynamic relation

$$de = Tds - Pdv \quad (B.3)$$

where P represents pressure and v specific volume, a substitution can be made in Equation (B.1) yielding

$$d\psi = -Pdv - sdT \quad (B.4)$$

Evaluating Equation (B.4) at constant temperature an expression for pressure in terms of free energy is arrived at, i.e.

$$P = - \left(\frac{\partial \psi}{\partial v} \right)_T \quad (B.5)$$

In a similar manner, an expression for specific internal energy can be derived by first evaluating Equation (B.4) at constant specific volume, bringing forth

$$\left(\frac{\partial \psi}{\partial T} \right)_v = - S \quad (B.6)$$

Following a rearrangement of the definition of free energy and then using Equation (B.6), specific internal energy can be expressed as

$$e = \psi - T \left(\frac{\partial \psi}{\partial T} \right)_v \quad (B.7)$$

Although the derivations may seem somewhat trivial, including the fundamentals here may assist in the interpretation of the model and the results for any given explosive. See Reference [30] for additional information.

REFERENCES

1. Krier, H. and Gokhale, S. S., "Modeling of Convective Mode Combustion Through Granulated Propellant to Predict Detonation Transition," AIAA Journal 16 (2), (1978), 177.
2. Krier, H. and Kezerle, J. A., "A Separated Two-Phase Flow Analysis to Study Deflagration-to-Detonation Transition (DDT) in Granulated Propellant," Seventeenth Symposium (International) on Combustion, The Combustion Institute, Pittsburgh, PA, (1979).
3. Hoffman, S. J., and Krier, H., "Fluid Mechanics of Deflagration to Detonation Transition in Porous Explosives and Propellants," AIAA Journal 19, (1981), 1571-1579.
4. Butler, P. B., Lembeck, M. L., and Krier, H., "Modeling of Shock Development and Transition to Detonation Initiated by Burning in Porous Propellant Beds," Combustion and Flame 46, (1982), 75-94.
5. Campbell, A. W., "Deflagration-To-Detonation Transition in Granular HMX," Seventh Symposium (International) on Detonation, Annapolis, MD, (1981).
6. Macek, A., "Transition from Deflagration to Detonation," J. Chem. Phys. 31, (1959), 162-167.
7. Tarver, C. M., Goodale, T. C., Shaw, R., and Cowperthwaite, M., "Deflagration-to-Detonation Transition Studies for Two Potential Isomeric Cast Primary Explosives," Sixth Symposium (International) on Detonation, Coronado, CA, August 24-27, (1976).
8. Jacobs, S. J., Comments to paper by Tarver, et al., Sixth Symposium (International) on Detonation, (1976), 249.
9. Kooker, D. E., and Anderson, R. D., "A Mechanism for the Burning Rate of High Density, Porous, Energetic Materials," Seventh Symposium (International) on Detonation, Annapolis, MD, June 16-19, (1981).
10. Coyne, D. W., Butler, P. B., and Krier, H., "Shock Development from Compression Waves Due to Confined Burning in Porous Solid Propellants and Explosives," AIAA Paper No. 83-0480, Reno, Nevada, (1983).
11. Dick, J. J., "Measurement of the Shock Initiation Sensitivity of Low Density HMX," Combustion and Flame 54, (1983), 121-129.
12. Setchell, R. E., "Ramp-Wave Initiation of Granular Explosives," Combustion and Flame 43, (1981), 255-264.
13. Weekerle, J., Johnson, J. O., and Halleck, P. M., "Shock Initiation of High-Density PETN," Sixth Symposium (International) on Detonation, Office of Naval Research, ACR-221, Arlington, VA, (1976), 20.

14. Campbell, A. W., Davis, W. C., Ramsey, J. B., and Travis J. R., "Shock Initiation of Solid Explosives," Physics of Fluids 4, (1961), 511.
15. Mader, C. L., "Initiation of Detonation by the Interaction of Shocks with Density Discontinuities" Physics of Fluids 8, (1965), 1811.
16. Howe, P., Frey, R., Taylor, B., and Boyle, V., "Shock Initiation and the Critical Energy Concept," Sixth Symposium (International) on Detonation, Coronado, CA, August 24-27, (1976).
17. Hayes, D. B., "Shock Induced Hot-Spot Formation and Subsequent Decomposition in Granular, Porous, Hexanitrostiblene Explosive," Detonation Physics Symposium, Minsk, Russia, (1981).
18. Bernecker, R. R., "The DDT Process for High Energy Propellants," AGARD Conference Preprint No. 367, Paper No. 14, Lisse, The Netherlands, (1984).
19. Butler, P. B., and Krier, H., "Analysis of Deflagration to Shock to Detonation Transition (DSDT) in Porous Energetic Solid Propellants," AGARD Conference Preprint No. 367, Paper No. 5, Lisse, The Netherlands, (1984).
20. Carroll, M. M., and Holt, A. C., "Static and Dynamic Pore-Collapse Relations for Ductile Porous Materials," Journal of Applied Physics 43, (1972), 1623-1635.
21. Coyne, D. W., "An Analysis of the Stress Wave Propagation and Shock Formation in Porous and Nonporous High Energy Propellants," Masters Thesis, Department of Mechanical and Industrial Engineering, University of Illinois, Urbana-Champaign (1983).
22. Baer, M. R., and Nunziato, J. W., "A Theory for Deflagration-to-Detonation Transition (DDT) in Granular Explosives," SAND Report, SAND82-0293, (1983).
23. Cowperthwaite, M., and Zwisler, W. H., "TIGER' Computer Code Documentation," Report PYV-1281, Stanford Research Institute, (1974).
24. Zel'dovich, Ya. B., and Raizer, Yu. P., Physics of Shock Waves and High Temperature Hydrodynamic Phenomena, Academic Press, New York and London (1966).
25. Mader, C. L., Numerical Modeling of Detonations, University of California Press, Berkeley, CA, (1979).
26. Nunziato, J. W., Kennedy, J. E., and Hardesty, D. R., "Modes of Shock Wave Growth in the Initiation of Explosives," Sixth Symposium (International) on Detonation, (1976), 47-59.
27. Kipp, M. E., and Lawrence, R. J., "WONDY V, A One-Dimensional Finite Difference Wave Propagation Code," Sandia Report, SAND 81-0930, (1982).

28. VonNeumann, J., and Richtmyer, R. D., "A Method for the Numerical Calculation of Hydrodynamic Shocks," Journal of Applied Physics 21, (1950), 232-237.
29. Engineering Design Handbook, Principles of Explosive Behavior, United States Army Material Command Pamphlet, No. 706-180, (1972).
30. Craig, B. G. in LASL Explosive Property Data (T. R. Gibbs and A. Popolato, Eds.), University of California Press, Berkeley, CA, 50.

END

FILMED

2-85

DTIC